Suspended Microchannel Resonators for Biomolecular Detection

by

Thomas P. Burg

Dipl.-Phys., Physics
ETH Zurich, 2001

Submitted to the Department of Electrical Engineering and Computer Science
in partial fulfillment of the requirements for the degree of

Doctor of Philosophy
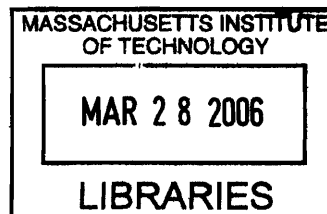
at the

MASSACHUSETTS INSTITUTE OF TECHNOLOGY

September 2005

Author . . . .
Department of Electrical Engineering and Computer Science
August 31, 2005

Certified by. . . . .
Scott R. Manalis
Associate Professor of Biological Engineering
Thesis Supervisor

Accepted by . . . .
Arthur C. Smith
Chairman, Department Committee on Graduate Students

Suspended Microchannel Resonators for Biomolecular Detection

by

Thomas P. Burg

Submitted to the Department of Electrical Engineering and Computer Science
on August 31, 2005, in partial fulfillment of the
requirements for the degree of
Doctor of Philosophy

Abstract

Microfabricated transducers enable the label-free detection of biological molecules in nano-liter sized samples. Integrating microfluidic detection and sample-preparation can greatly leverage experimental efforts in systems biology and pharmaceutical research by increasing analysis throughput while dramatically reducing reagent cost.

Microfabricated resonant mass sensors are among the most sensitive devices for chemical detection, but degradation of the sensitivity in liquid has so far hindered their successful application in biology. This thesis introduces a type of resonant transducer that overcomes this limitation by a new device design: Adsorption of molecules to the inside walls of a suspended microfluidic channel is detected by measuring the change in mechanical resonance frequency of the channel. In contrast to resonant mass sensors submersed in water, the sensitivity and frequency resolution of the suspended microchannel resonator is not degraded by the presence of the fluid. Our device differs from a vibrating tube densitometer in that the channel is very thin, and only molecules that bind to the walls can build up enough mass to be detected; this provides a path to specificity via molecular recognition by immobilized receptors.

Suspended silicon nitride channels have been fabricated through a sacrificial polysilicon process and bulk micromachining, and the packaging and microfluidic interfacing of the resonant sensors has been addressed. Device characterization at 30 mTorr ambient pressure reveals a quality factor of more than 10,000 for water filled resonators; this is two orders of magnitude higher than previously demonstrated Q-values of resonant mass sensors for biological measurements.

Calculation of the noise and the sensitivity of suspended microchannel resonators indicate a physical limit for mass resolution of approximately 0.01 ng/cm^2 (1 Hz bandwidth). A resolution of $\sim$0.1 ng/cm^2 has been experimentally demonstrated in this work. This resolution constitutes a tenfold improvement over commercial quartz crystal microbalance based instruments. The ability to detect adsorbing biomolecules by resonance frequency has been validated through binding experiments with avidin and various biotinylated proteins.

Thesis Supervisor: Scott R. Manalis
Title: Associate Professor of Biological Engineering

3

Acknowledgments

First and foremost, I want to thank Professor Scott Manalis for the opportunity to do my thesis research in his laboratory. Scott made this work possible by providing the best resources and scientific advice a student could ask for, and his contagious optimism and enthusiasm were a constant source of motivation for me. Over the past years, Scott has helped me grow both professionally and personally. It has been a privilege for me to work under his supervision, and I do not know where I could have found a more dedicated, knowledgeable, and supportive advisor.

I also want to thank my thesis committee, Professor Denny Freeman and Professor Marty Schmidt for their guidance over the course of the past year. Discussions in committee meetings and their constructive review of this manuscript were a great help in the completion of this thesis.

Furthermore, I wish to express my gratitude to all group members and collaborators who contributed to this work: Leo Alexopoulos in collaboration with the Sorger Lab was a great help with fluorescence experiments. Nebojsa Milovic was an indispensable resource for everything that involved chemistry and HPLC equipment. Christine Tsau contributed her vast experience in microfabrication to the process development and device testing. My undergraduate students George Alex Popescu and Stanley Wang deserve credit for their great work to test the resonant sensors under vacuum, and for their help with PDMS packaging. A steady source of fun and enjoyment was the company of all members of the Nano group, and, in particular, of those who helped me get started in the early years: Emily Cooper, (Doktor) Jürgen Fritz, Cagri Savran and Andrew Sparks.

I am also deeply indebted to Vicky Diadiuk and the entire staff of the MIT Microsystems Technology Lab who taught me the intricacies of fab processes and often did the impossible to let me convert drawings and process diagrams into working devices. Special thanks also go to Amir Mirza and John Foster of Innovative Micro Technology for enabling the fabrication of glass frit packaged resonators at their foundry despite all technological challenges.

The detailed analytical and numerical analysis of transport processes conducted by Thomas Gervais of Prof. Klavs Jensen's group gave me insight into the importance of mass transport limitations in thin microfluidic channels. The results of his work will guide the design of future devices and experiments.

Finally, I want to thank my family, especially my parents Doris and Günter and my brother Andy for their love and support over the years. They gave me the ability and the confidence to follow my own path, and I know I would have never made it this far without them.

Contents

List of Figures

10

List of Tables

Chapter 1

Introduction

1.1 Background

Microfabricated transducers enable the detection of biomolecules in microfluidic systems with nanoliter size sample volumes. Their integration with microfluidic sample preparation into lab-on-a-chip devices can greatly leverage experimental efforts in systems biology and pharmaceutical research by increasing analysis throughput while dramatically reducing reagent cost. Microdevices can also lead to robust and miniaturized detection systems with real-time monitoring capabilities for point-of-use applications. Sensors that convert biochemical information into electronic signals typically measure changes in a physical property of a solid-liquid interface, such as surface charge, refractive index, surface stress, or mass. To provide specificity, immobilized receptors preferentially bind the target molecules of interest, altering the properties of the surface and generating a signal. Unlike conventional protein microarrays, this scheme does not require a secondary antibody or fluorescent labeling of the target molecules. Despite reducing the cost and labor associated with biomolecular interaction analysis, label-free detection technologies enable experiments in which labeling would interfere with the binding reaction, or in which real-time measurements of the binding kinetics are of interest. Surface plasmon resonance (SPR) [3, 22, 65] and quartz crystal microbalance (QCM) [45, 58, 72, 49] based instruments are currently the two most widely employed methods for label-free protein interaction exper-

iments, with applications ranging from fundamental research in systems biology to drug discovery and quality control. Laboratory instruments based on SPR and QCM are commercially available, however these two principles are not easily amenable to miniaturization and batch fabrication. The three main types of microfabricated sensors for biochemistry can be classified as electronic, optical and mechanical transducers, all of which have specific advantages and limitations. Electronic field effect devices can be highly sensitive to binding of charged molecules regardless of molecular weight. However due to charge screening these sensors require low ionic strength solutions and tight binding of ligands to the surface to operate effectively. [9, 18, 11] Integrated optical sensors rely on the measurement of refractive index in the evanescent field of planar waveguides, which generally limits the thickness of the sensitive layer to less than 100nm and requires intricate alignment of external optical components. [71, 41] Micromechanical surface stress sensors have recently been the subject of many research efforts, in part because of their simplicity and high sensitivity in certain assays. [37, 55, 81, 77, 54] However, the relationship between surface stress and the density of bound targets depends on a combination of physical properties, such as steric hindrance, electronic charge, and hydrophobicity of the molecules, so that the quantitative power of the method is limited. In addition, the need for different surface functionality on the top and bottom side of the device complicates assay development. Another class of micromechanical transducers is formed by micromechanical resonators whose natural frequency provides a direct quantitative measure of mass adsorbed to their surface. Resonant mass sensors have been highly successful for chemical sensing in gaseous environments. [25, 28, 20, 36, 21, 42, 67] In liquids, however, the mass sensitivity and frequency resolution of resonant sensors is degraded by the low quality factor and large effective mass that is induced by viscous drag. While certain designs have the potential to greatly alleviate these limitations, [75, 19, 39] their sensitivity is still inferior to air or vacuum based resonators [73]. To overcome this problem, various groups have employed the 'dip and dry' method, by which the resonance frequency is measured in air before and after the device has been exposed to the sample. [27, 45, 34, 26] To ensure reliability, great care must be taken to avoid

contamination of the resonating element. Furthermore, the technique does not allow real-time measurements for studying binding kinetics. For some assays, mass enhancing labels can be used to increase the signal to noise ratio in liquid [72] at the expense of additional sample preparation and experimental complexity.

1.2 Device concept

Signal transduction in resonant mass sensors relies on the dependence of the mechanical resonance frequency f_0 on the effective device mass m^*:

$$f_0 = \frac{1}{2\pi} \sqrt{\frac{k}{m^*}} \tag{1.1}$$

When a resonant transducer is submersed in fluid, the effective mass is increased and the quality factor is reduced, thereby leading to a degradation of mass sensitivity. Vibrating tube designs avoid this problem by confining the fluid to the inside of the resonator. To date, there are several examples of commercially available laboratory instruments that employ this concept for the measurement of fluid density. Enoksson et al. first recognized the potential of suspended microchannels configured as micromechanical resonators for measuring fluid density and flow in a microfluidic format. [13, 14, 15, 16] Since then, various implementations of micromachined vibrating tube densitometers and flow sensors have been reported. [74, 63, 62, 61].

The primary feature that sets our work apart from research in the area of vibrating tube densitometers is that molecules that bind to the channel walls are detected, thereby providing a path to specificity via molecular recognition by immobilized receptors such as antibodies. We have therefore optimized the design for sensitivity to surface mass; this requires the fluid channel and the walls of the hollow resonator to be very thin.

To detect specific biomolecules, the channel walls are first functionalized with a layer of capture molecules, as illustrated in Figure 1-1. Subsequent accumulation of target molecules on the functionalized walls decreases the resonance frequency.
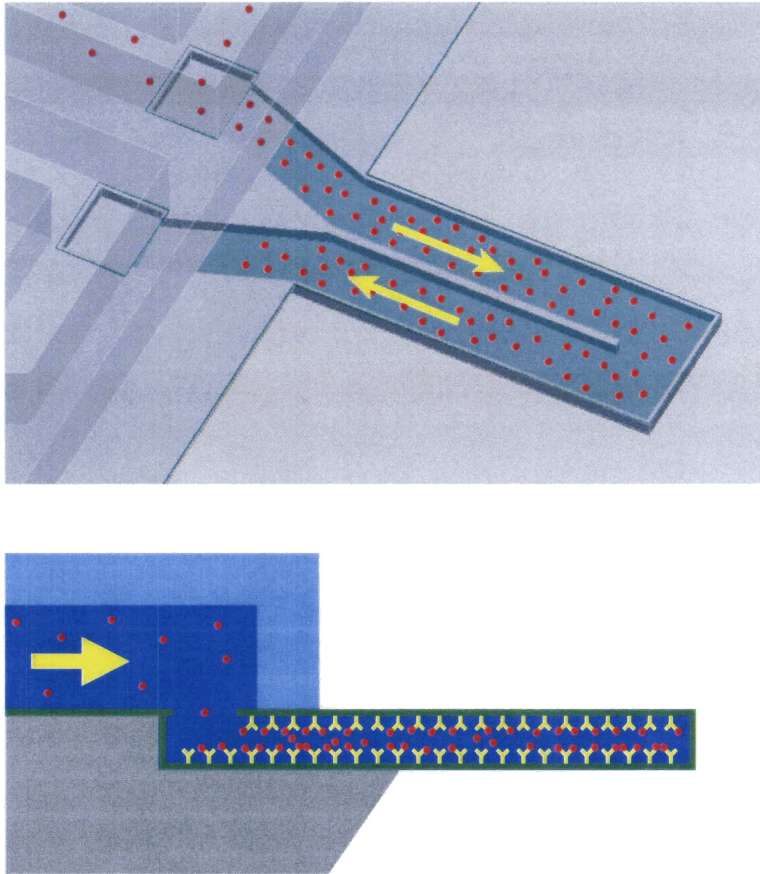
Figure 1-1: Sample molecules (red) flow through a hollow cantilever and are captured by immobilized receptors (yellow). The mass increase is detected by the change in resonance frequency.

Molecules that adsorb onto the walls of the fluid filled resonator are perpetually replenished by the flow of fresh sample through the device and, if the ratio of surface area to volume is very large, the adsorbing molecules eventually build up enough mass to cause a detectable frequency shift.

Since the mass density of biological molecules is greater than the mass density of water (e.g. proteins typically range from 1.3–1.4 g/cm^3) [17, 70, 23, 57], the resonance frequency of a suspended microchannel is decreased by the adsorption of molecules to the channel walls.

Chapter 2

Sensitivity and Noise

2.1 Mass sensitivity of hollow resonators

Assuming uniform surface coverage, the mass sensitivity of a long and thin suspended microchannel resonator with constant cross section is to first order independent of the exact geometry and vibrational mode of the channel. To illustrate the nomenclature for the following calculations we will refer to a double clamped beam, as illustrated in Fig. 2-1, however the results are independent of this particular geometry. L is the total length of the suspended section of the fluid path, the wall thickness is denoted by t, and H is the inner channel height. The resonance frequency ω_0 of a mode of vibration is found by the principle of Rayleigh-Ritz. Equating the maximum kinetic and potential energy (U) of the displacement field $u(z)$ gives

$$\omega_0^2 = \frac{U}{\int_0^L \frac{m_A(z)}{2} u(z)^2 \mathrm{d}z} \quad . \tag{2.1}$$

We define $m_A(z)$ as the mass per unit length

$$m_A(z) = \int_{\mathrm{X-section}} \rho(x, y, z) \mathrm{d}x \mathrm{d}y \tag{2.2}$$

where $\rho(x, y, z)$ denotes the local density of mass. If molecules with a greater density than water accumulate on the channel walls, this results in an additional term

$\Delta\rho(x, y, z)$, which is greater than zero only in the thin layer of adsorbed molecules. m_A then increases like

$$m_A \to m_A(z)\left(1 + \frac{\Delta m_A(z)}{m_A(z)}\right) \qquad (2.3)$$

and the resulting change in eigenfrequency, $\Delta\omega_0$, is given to the first order by

$$\frac{\Delta\omega_0}{\omega_0} = -\frac{1}{2}\frac{\int_0^L u(z)^2 \Delta m_A(z)\mathrm{d}z}{\int_0^L u(z)^2 m_A(z)\mathrm{d}z} \qquad . \qquad (2.4)$$

If the relative mass increase of each cross section is independent of position, i.e.

$$\frac{\Delta m_A(z)}{m_A(z)} = \mathrm{const.} \qquad (2.5)$$

equation 2.1 can be written as

$$\omega^2 = \frac{1}{1 + \frac{\Delta m_A}{m_A}} \frac{U}{\int_0^L \frac{m_A}{2}u(z)^2\mathrm{d}z} \qquad (2.6)$$

or, since Δm_A is usually small relative to m_A

$$\frac{\Delta\omega_0}{\omega_0} \approx -\frac{1}{2}\frac{\Delta m_A}{m_A} \qquad . \qquad (2.7)$$

Equation 2.6 shows that the ratio $\frac{\omega}{\omega_0}$ is only a function of $\frac{\Delta m_A}{m_A}$ and does not depend on the mode shape $u(z)$ or the exact cross-section geometry. Mass sensitivity can therefore be optimized by minimizing the mass and by maximizing the number of available binding sites for each cross section. The shape and the mode of vibration can be chosen to optimize fluid delivery, resonator quality factor, and readout signal-to-noise ratio. A useful figure of merit to assess the utility of the sensor for biochemical detection is mass sensitivity per surface area. Rewriting Equation 2.7 as

$$\frac{\Delta\omega_0}{\omega_0} \approx -\frac{1}{2}\frac{\Delta m_A}{s}\left(\frac{m_A}{s}\right)^{-1} \qquad (2.8)$$

where s is the length of the solid-liquid boundary shows that s/m_A is the device parameter that most critically influences the sensitivity.

For example, m_A of a rectangular cross section of wall thickness t and fluid layer thickness d changes by

$$\frac{\Delta m_A}{m_A} \approx \frac{\sigma}{\rho_{SiN}t + \frac{1}{2}\rho_{H_2O}\,d} \qquad (2.9)$$

when molecules adsorb to the surface at a density of σ ng/cm^2. The approximation assumes that the channel width is significantly greater than the depth of the fluid layer as well as the thickness of the channel walls. The thermomechanical limit for frequency resolution using a high quality resonator is $\sim$0.01 ppm in a 1 Hz bandwidth. Assuming 1 μm wall and fluid layer thickness with silicon nitride as the structural material, Equations 2.7 and 2.9 predict a minimum detectable mass $\Delta\sigma$=7 pg/cm^2, or $\sim$1 protein of 100 kDa per square micron.

Equation 2.4 only takes into account the frequency shift due to added mass, i.e. the change in maximum kinetic energy. The assumption that molecular adsorption does not change the maximum potential energy is valid if the channel cross-section is symmetric about the neutral axis. Changes in surface tension at the top and bottom of the channel will then cancel, resulting in no net modulation of the spring constant. This is the case for all cantilever resonators that were designed and tested in this work. The resonance frequency depends on surface stress if the strain at the top and bottom channel surface during vibration is not equal and of opposite sign.

2.2   Effective mass of biomolecules in solution

Detecting the adsorption of biological molecules in solution by mass relies on the difference in specific gravity between the adsorbed layer and the water molecules it displaces. Kautzmann et al. [57] and, more recently, Voros [70] have determined the mass density of proteins in aqueous solution to be on the order of 1.3-1.4 g/cm^3. Furthermore, the work by Voros has shown that this value not only applies when the proteins are free in solution, but also when they are adsorbed to a solid, hydrated surface. The value of 1.3-1.4 g/cm^3 represents an effective density whose meaning is most easily understood by comparing the mass of a fixed volume of solution before
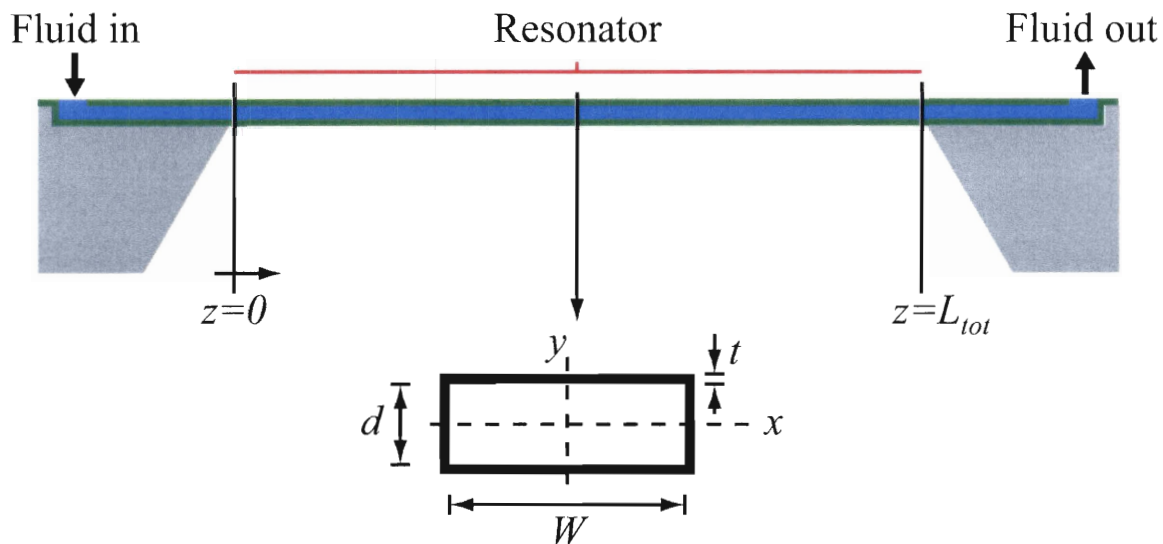
Figure 2-1: A double clamped beam is used to illustrate that the mass sensitivity of a suspended microchannel resonator depends only on the cross section mass.
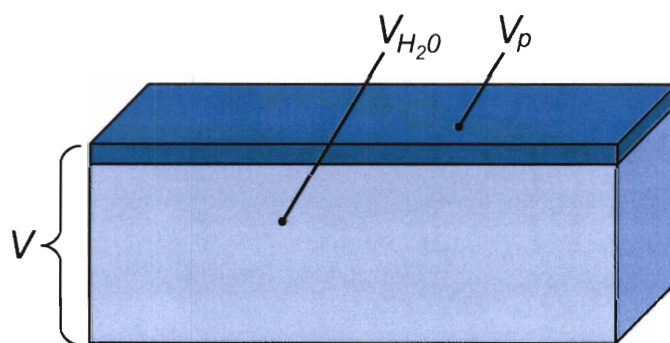
Figure 2-2: Most proteins have an effective density of 1.3–1.4 g/cm³ in aqueous solution. When dry proteins are added to a fixed volume V that is initially filled with water, the mass of the volume increases by ~25% of the dry protein mass.

and after adding m_p grams of dry protein. The total volume V can be divided into the pure water volume V_{H_2O} and the volume contributed by the concentrated and solvated biomolecules, V_p, as illustrated in Fig. 2-2. The total mass in the volume V is then

$$m = \rho_{H_2O}(V_{H_2O} - V_p) + \rho_p V_p \qquad (2.10)$$

or, rearranging terms and replacing V_p by m_p/ρ_p

$$\frac{m}{V} = \rho_{H_2O} + \frac{m_p}{V}\frac{\rho_p - \rho_{H_2O}}{\rho_p} \qquad (2.11)$$

so that the increase in solution density resulting from a protein concentration c_p is given by

$$\Delta\rho = c_p\frac{\rho_p - \rho_{H_2O}}{\rho_p} \qquad . \qquad (2.12)$$

Equation 2.12 shows that when solvated proteins are added to a closed water reservoir, displacing the necessary volume of pure water, the net mass of the reservoir will increase by only approximately one quarter of the mass of dry protein added. This is analogous to a hollow resonator, which comprises a constant fluid volume and contains varying amounts of protein. When molecules bind to the surfaces surrounding the volume rather than being freely dispersed in solution, the above picture still gives a good estimate of the net mass; although water is known to be more densely packed at solid-liquid interfaces, its physical properties closely match those of the bulk only a few monolayers from the surface. [48] Since proteins are generally several nanometer in size, surface induced ordering of water molecules will be considered negligible.

2.3 Frequency resolution and sources of error

The ability to detect the adsorption of minute amounts of mass with micromechanical resonators is determined by the ratio of sensitivity to frequency resolution. Sensitivity, measured as the relative frequency shift per added mass, is solely a function of the cross section mass of the microchannel resonator. Frequency resolution depends

on factors that can be broadly classified as statistical measurement errors and as systematic errors. Statistical errors result from random noise in the resonator and in the deflection readout, and they can always be reduced by narrowing the measurement bandwidth. [12] Systematic errors, on the other hand, are fluctuations in resonance frequency that are often unrelated to the adsorbed mass and instead arise from cross-sensitivity to, for example, temperature, pressure, or flow. Systematic errors can often be reduced to acceptable levels by environmental control and by minimizing the transducers sensitivity to the operating conditions. However, technological refinements are not always sufficient when the duration of an experiment exceeds several tens of minutes, which is common for biochemical binding reactions. In this case, satisfactory resolution may be achieved through differential sensing, whereby the signal of a mechanically identical, yet distinctly functionalized sensor is used as a control. [54, 56]

2.3.1 Phase and frequency noise

The resonance frequency of a mechanical structure, unlike position or velocity, is not itself subject to intrinsic noise at non-zero temperatures. The precision of any estimate of resonance frequency, however, is limited by the thermal fluctuations in the observable degrees of freedom of the system. [69] Although the signal-to-noise ratio can, in theory, be improved by increasing the magnitude of the drive, the vibration amplitude is limited by the mechanical properties of the resonator and by the maximum actuator force. The dynamics of the micromechanical resonators considered in this work can be modeled by a one-dimensional harmonic oscillator

$$\ddot{x} + \frac{\omega_0}{Q}\dot{x} + \omega_0^2 x = \frac{\omega_0^2}{k}F(t), \quad X(\omega) = \frac{\omega_0^2}{k}\underbrace{\frac{1}{\omega_0^2 - \omega^2 + j\frac{\omega_0\omega}{Q}}}_{H(\omega)} \cdot F(\omega) \quad (2.13)$$

with the natural frequency ω_0, spring constant k, and quality factor Q. When the resonator is in thermal equilibrium with the environment and no external drive signal is applied, the force $F(t)$ has zero mean and a non-zero white noise power that is

responsible for the Brownian motion of the resonator. According to the equipartition theorem, the fluctuations of x due to Brownian motion are given by

$$\langle x^2 \rangle = \frac{k_B T}{k} \quad . \tag{2.14}$$

The power spectral density S_{ff} of F is

$$\langle x^2 \rangle = \frac{1}{2\pi} \int_0^\infty |H(\omega)|^2 S_{ff} d\omega \tag{2.15}$$

which yields

$$S_{ff} = \frac{4 k_B T k}{Q \omega_0} \quad . \tag{2.16}$$

In order to understand the uncertainty in ω_0 introduced by a certain noise level, $\langle x^2 \rangle$, we consider the case where the system is driven at a fixed frequency ω so that ω_0 can be obtained from the phase lag between the drive signal and the response. With $F_\omega(t) = F_0 e^{j\omega t}$ the measured response is

$$x(t) = F_0 |H(\omega)| e^{j(\omega t + \angle H(\omega))} + \left(\delta x_1(t) + j \delta x_2(t) \right) \quad . \tag{2.17}$$

The phase of $\delta x_1(t) + j \delta x_2(t)$ is uniformly distributed on the interval $[0, 2\pi)$, and the mean amplitude $\langle \delta x_1^2 + \delta x_2^2 \rangle$ is equal to the mean square noise level in the measurement bandwidth. The uniform distribution of the phase implies that $\langle \delta x_1^2 \rangle = \langle \delta x_2^2 \rangle$. When $x(t)$ is measured by lock-in detection with a time-constant τ, only the narrow band of frequencies $\omega \pm \frac{2\pi}{\tau}$ contributes to the noise, and δx_1 restricted to this frequency band appears as amplitude noise, while $\delta x_2 / |F_0 H(\omega)|$ appears as phase noise. In the given bandwidth the phase can therefore be measured only to within

$$\Delta \phi = \sqrt{\frac{\frac{1}{2\pi} \int_{\omega - \frac{2\pi}{\tau}}^{\omega + \frac{2\pi}{\tau}} \frac{S_{ff} |H(\omega')|^2 d\omega'}{2}}{F_0^2 |H(\omega)|^2}} \approx \frac{1}{F_0} \sqrt{\frac{S_{ff}}{\tau}} \tag{2.18}$$

where the last approximation is reached by neglecting the frequency dependence of $H(\omega')$ in the narrow band $\omega \pm \frac{2\pi}{\tau}$. Equation 2.18 shows that when thermal fluctuations

are the limiting factor, phase noise is independent of frequency. The measurement of $\angle H(\omega)$ enables estimation of ω_0 via the relationship

$$\angle H(\omega) = -\arctan\left(\frac{\omega_0 \omega}{Q(\omega_0^2 - \omega^2)}\right) \quad . \tag{2.19}$$

If the phase measured at ω_0 is used to estimate small deviations of the natural frequency from ω_0, the error $\Delta\phi$ translates into an estimation uncertainty

$$\sqrt{\langle(\widehat{\omega_0} - \omega_0)^2\rangle} = \frac{\Delta\phi}{\frac{\partial}{\partial\omega}\angle H(\omega)|_{\omega_0}} = \frac{\omega_0}{2Q}\Delta\phi \quad . \tag{2.20}$$

Combining equations 2.16, 2.18 and 2.20 then yields

$$\frac{\sqrt{\langle(\widehat{\omega_0} - \omega_0)^2\rangle}}{\omega_0} = \sqrt{\frac{k_B T k}{\tau\omega_0}} \frac{1}{Q^{3/2} F_0} \quad . \tag{2.21}$$

Equation 2.21 shows the importance of a high quality factor and large drive amplitude for obtaining high accuracy in resonant sensors. Ultimately, the amplitude is limited by the maximum force of the actuator, as well as the mechanical and geometrical characteristics of the resonator. The inverse relationship between resolution and the first derivative of the phase in equation 2.20 illustrates that it is advantageous to conduct the measurement at or close to the actual resonance frequency, because this is where the measurement is least susceptible to phase noise. The phase measurement and conversion to frequency may be implemented in different ways, which will be discussed in more detail in chapter 5, yet the fundamental limit for frequency resolution given by equation 2.21 is independent of the method.

2.3.2 Pressure sensitivity

Cross-sensitivity to hydrodstatic pressure is an important aspect for the operation of resonant mass sensors in fluids. When the device is used in continuous flow, the pressure can fluctuate due to flow instabilities, changes in flow resistance or variations in backpressure. Controlling all these parameters to high precision incurs high equipment expenses and is generally not an option in portable instruments. Pres-
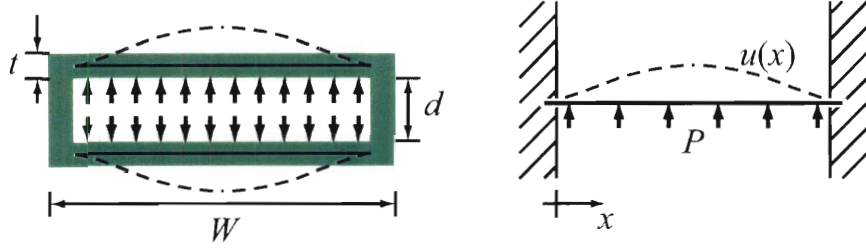
Figure 2-3: The walls of a suspended microchannel deflect under hydrostatic pressure. For thin channels, the deflection is similar to that of a doubly-clamped beam.

sure fluctuations are commonly the result of events like sample injection, deliberate changes in pump rate, or the formation of bubbles in the fluidic system, and as such they cause systematic errors that may not be reduced by statistical means.

The pressure effect on resonance frequency of a long and thin hollow beam in transverse vibration can be calculated from the equation of motion

$$\frac{\partial^4 u}{\partial z^4} + \frac{m_A}{EI}\frac{\partial^2 u}{\partial t^2} = \frac{f(z,t)}{EI} \tag{2.22}$$

where E is Young's modulus, I is the area moment of inertia with respect to the neutral plane, and m_A is the cross-section mass defined by equation 2.2. $f(z,t)$ on the right hand side represents the driving force per unit length. The frequency of the n-th eigenmode has the general form

$$\omega_n^2 = \frac{\lambda_n^4}{L^4}\frac{EI}{m_A} \tag{2.23}$$

where λ_n is a numeric constant that depends on the boundary conditions and L is a characteristic length, e.g. the beam length for a cantilever device. The influence of small deformations of the cross-section may be written as

$$\frac{\Delta\omega_n}{\omega_n} \approx \frac{1}{2}\left(\frac{\Delta I}{I} - \frac{\Delta m_A}{m_A}\right) \quad . \tag{2.24}$$

For the rectangular channel geometry shown in Figure 2-3 it is possible to derive simple expressions for ΔI and Δm_A as a function of pressure. If the width of the

27

channel is much greater than its height, the sidewalls are very stiff and experience negligible deformation, while the top and bottom diaphragms deflect under internal pressure as indicated by the dashed line in Figure 2-3. The top and bottom may be approximated as fully clamped beams subject to a uniform pressure load P. The deflection as a function of position and pressure is

$$u(x) = \frac{1}{2} \frac{P(W - 2t)^2 x^2}{Et^3} \left(1 - \frac{x}{W - 2t} \right)^2 \tag{2.25}$$

and the area moment of inertia at $P = 0$ is

$$I_0 = \frac{t(d + 2t)^3}{6} + \frac{W - 2t}{12} \left[(d + 2t)^3 - d^3 \right] \tag{2.26}$$

where the first term accounts for the contribution of the sidewalls, and the second term represents the central region of the channel. When the top and bottom walls deflect by $u(x)$, the new moment of inertia is to first order in u

$$I_u = I_0 + \underbrace{2 \int_0^{W - 2t} u(x)(d + t)t\mathrm{d}x}_{\Delta I} \tag{2.27}$$

and evaluation of the integral after inserting equation 2.25 yields

$$\Delta I = \frac{1}{30} \frac{P}{Et^2} (d + t)(W - 2t)^5 \quad . \tag{2.28}$$

Similarly, we find for the increase in mass for a channel that is filled with water:

$$\Delta m_A = \rho_{H_2O} \frac{1}{30} \frac{P}{Et^3} (W - 2t)^5 \tag{2.29}$$

Real devices will have larger I_0 and m_A than those of the plain rectangular channel in Figure 2-3, but provided that the fluid conduit can be approximated as shown, the expressions for the increments ΔI and Δm_A are valid.

2.3.3 Bias voltage dependence

The resonators that are the basis of this work are actuated by electrostatics. The bias voltage that is applied between the resonator and the actuation electrode can have a significant effect on the resonance frequency. Although the electrostatic force is small and the static deflection of the resonators is on the order of a few nanometers, the presence of a force gradient lowers the effective spring constant, which, in turn, is observed as a change in frequency. Sensitivity to electrostatics is an important consideration in resonant transducers even if the actuator bias itself is stable, because insufficient shielding may allow external fields to influence the measurement.

The dependence of the effective spring constant k^* on bias voltage is obtained from the definition

$$
\begin{aligned}
k^* &= -\frac{\partial^2}{\partial x^2}\left(\frac{1}{2}C(x)V^2 - \frac{1}{2}kx^2\right) \\
&= k - \frac{1}{2}\frac{\partial^2 C}{\partial x^2}V^2 \quad .
\end{aligned}
\tag{2.30}
$$

$C(x)$ is the capacitance of the electrostatic actuator, V is the bias voltage, and k denotes the mechanical spring constant. The associated change in resonance frequency is

$$
\frac{\Delta\omega_0}{\omega_0} = -\frac{1}{4}\frac{\frac{\partial^2 C}{\partial x^2}V^2}{k} \quad .
\tag{2.31}
$$

In most cases the actuator capacitance may be approximated by a parallel plate capacitor with a gap d_0 and capacitance $C(x = 0) = C_0$, which inserted into 2.31 gives

$$
\frac{\Delta\omega_0}{\omega_0} = -\frac{1}{2}\frac{C_0 V^2}{d^2 k} \quad .
\tag{2.32}
$$

For small fluctuations ΔV superimposed on a constant voltage V_0, i.e. $V = V_0 + \Delta V$, the last equation reads

$$
\frac{\Delta\omega_0}{\omega_0} = -\frac{1}{2}\frac{C_0 V_0^2}{d^2 k} - \frac{C_0 V_0}{d^2 k}\Delta V \quad .
\tag{2.33}
$$

2.3.4 Temperature coefficient

Temperature affects the sensor signal by altering the stiffness and stress of the resonator structure and, in the case of fluid filled resonators, through changes in bulk density of the liquid. The density of water has a temperature coefficient of -0.256 $(mg/cm^3)/°C$ at room temperature, [40] and, as will be shown later, this means that for our devices temperature needs to be stable to within $\sim$0.01°C to avoid density related measurement errors. Radenovic et al. measured the temperature dependence of the spring constant of commercial silicon nitride cantilevers for atomic force microscopy. [47] They found that the resonance frequency decreased with an increase in temperature, consistent with a decrease in Young's modulus. The temperature effect on resonators that are clamped on more than one side is further determined by stress induced upon heating or cooling. Examples of such devices include bridges, membranes, or torsional resonators. The silicon nitride film used in the resonators discussed here has a coefficient of thermal expansion that is slightly lower than that of the silicon substrate, [30, 31, 68] so that heating induces a tensile stress in the film, which in turn yields an increase in resonance frequency for double-clamped structures.

A reliable way to reduce temperature related errors is to conduct a differential measurement of two mechanically identical resonators. Only one of the devices is exposed to the sample while the other device provides a reference measurement. If both transducers are closely spaced on the same chip, the mechanical characteristics and their respective temperature are generally matched well enough to enable cancellation of thermal drift.

Chapter 3

Device Design

3.1 Resonator design and modeling

The design of resonators for this work was motivated primarily by the capabilities of the fabrication process and the requirements for optical readout and electrostatic actuation. The widest channels that could be fabricated with high yield at 1 μm depth were 20 μm wide. Figure 3-1 summarizes the four design variations that were fabricated and characterized, and important characteristics of the cantilever and torsional resonators will be discussed in the following sections. The first design shown in Figure 3-1 was used in conjunction with PDMS microfluidics to conduct the initial proof-of-principle experiments [5], while the remaining three device types were built in collaboration with Innovative Micro Technology[1] and packaged using glass frit bonding. Given the great similarity between all three cantilever resonators, detailed analysis is provided here only for design III, and it will be pointed out when there are significant differences to the multi-channel designs with smaller cross-section per channel. Most of the calculations in chapter 2 are specific to thin structures whose modes of vibration can be modeled well by pure bending. The results are not directly applicable to the case of torsional resonators, however certain qualitative predictions can still be made. The mechanical characteristics of torsional resonators with non-trivial flexure cross-section are difficult to model analytically; finite-element modeling

---

[1]Innovative Micro Technology, Santa Barbara (CA)
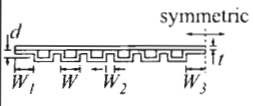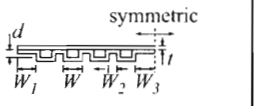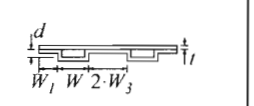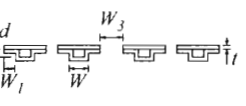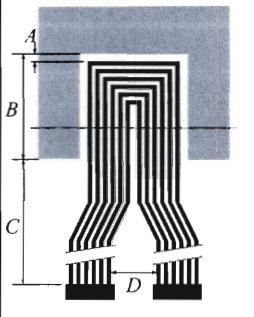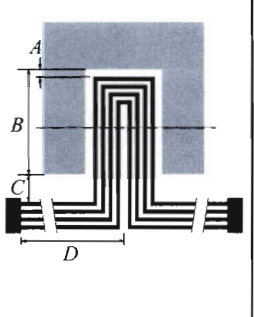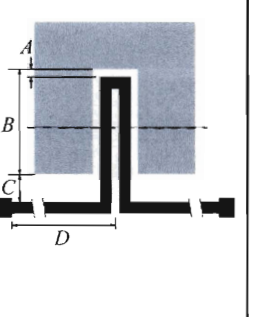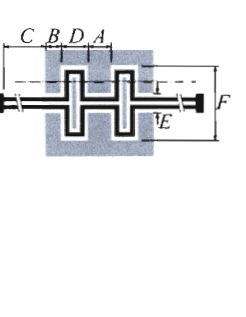
	Cantilever I	Cantilever II	Cantilever III	Torsional resonator
Package	PDMS	Glass frit, vacuum		
Section				
Layout	 $t = 0.8$ $A = 9.0$ $d = 1.2$ $W = 8.0$ $B = \begin{bmatrix}154\\304\end{bmatrix}$ $W_1 = 9.0$ $C = 566$ $W_2 = 4.0$ $D = 132$ $W_3 = 3.0$	 $t = 0.8$ $A = 10$ $d = 1.0$ $B = 320$ $W = 10$ $C = 45$ $W_1 = 10$ $D = 700$ $W_2 = 3.0$ $W_3 = 1.5$	 $t = 0.8$ $A = 10$ $d = 1.0$ $B = 320$ $W = 20$ $C = 45$ $W_1 = 10$ $D = 700$ $W_3 = 1.5$	 $t = 0.8$ $A = 30$ $d = 1.0$ $B = 15$ $W = 10$ $C = 550$ $W_1 = 10$ $D = 70$ $W_3 = 30$ $E = 43$ $F = 130$
$2 \cdot m_A/s$	1.08 mg/cm^2	0.96 mg/cm^2	0.96 mg/cm^2	1.78 mg/cm^2
f_0 (exp.)	42 kHz	36 kHz	33 kHz	615 kHz

Figure 3-1: Cantilever beams and torsional resonators with different fluid channel layouts were fabricated and tested. The microfluidic channels in all devices were $1\mu m$ tall.

has therefore been used to calculate the resonance frequencies, and mode shapes of these devices.

3.1.1   Cantilever resonators

The main advantages of the cantilever design are the simplicity of the readout by means of the optical lever method, and the well understood theory thanks to a wealth of studies in the field of atomic force microscopy. In addition, the geometry of cantilevers and bridges is uniquely suited to being filled with one continuous fluidic channel. We found that filling is not reliable in geometries containing channel junctions, since the high surface area-to-volume ratio of these channels facilitates trapping of air in places where channels split or converge.

The design of the lead channels that connect the resonator to the fluid inlets was dictated by the design rules of the package. Soft lithography in PDMS enables the fabrication of narrow microfluidic channels with near vertical sidewalls which can be aligned to a substrate with a narrow tolerance. The channel length and inlet separation (dimensions C & D in Figure 3-1) can therefore be made short; in particular the length C could, in principle, be reduced to approximately 100 μm, which would enable not only higher flow rates but also reduce the concern about sample depletion in kinetic measurements. The inherent width of the glass frit used to package the devices with glass microfluidics required long inlet and outlet channels for cantilever designs II and III and for the torsional resonators. After compression, the frit is between 300 and 400 μm wide, and additional alignment tolerances need to be taken into account because of the limited accuracy of the silk-screening process and the potential of misalignment during the glass frit bonding (c.f. chapter 4).

The expected sensitivity for all types of resonators may be estimated using equation 2.8, and the result $S = 2 \cdot m_A/s$ in units of mg/cm^2 is listed in Figure 3-1. S has the convenient interpretation that adsorption of S ng/cm^2 yields a frequency shift of one part per million (1 ppm). The quoted figures are based on a simplified geometry that neglects deviations from the constant cross-section at the corners near the cantilever tip, which, in addition to fabrication tolerances, may cause the real device
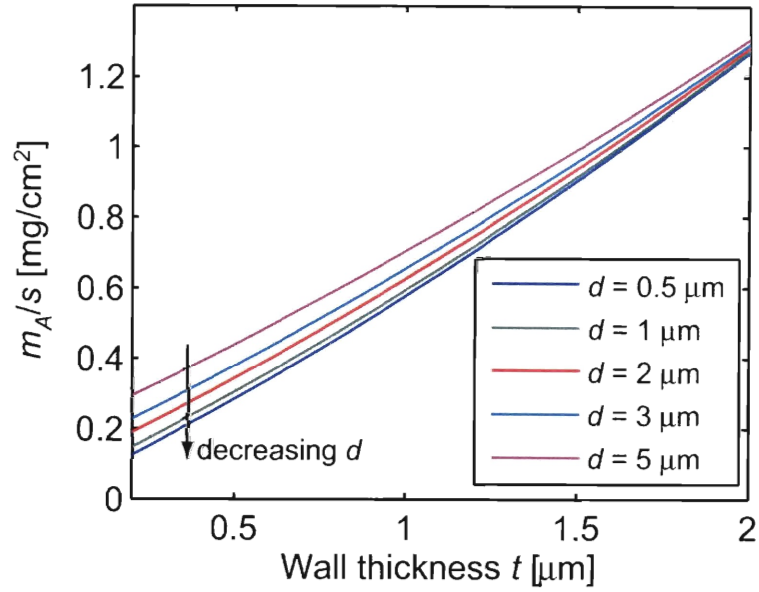
Figure 3-2: The sensitivity of cantilever design III is most critically influenced by the wall thickness t. The channel depth d has less impact on sensitivity due to the lower density of the fluid compared to the wall material (1 g/cm³ vs. 3.2 g/cm³) and the smaller cross-section area occupied by the fluid.

sensitivity to differ from the estimate. Nonetheless, the ratio m_A/s indicates general trends that are helpful for the design. An important observation is that varying the planar resonator geometry generally has little impact on the sensitivity for a given set of design rules. The width of the border around the cantilever, W_1, is limited by the lithographic alignment accuracy, and the space between individual channels, W_2, is determined by the minimum line width allowed between etched features. Because of the low height of the channels, adding additional vertical features can not substantially increase the surface area. As far as the planar sensor geometry is concerned, sensitivity can be judged best by the fill-factor of the channel area divided by the area of non-wetted parts. Figure 3-2 illustrates the dependence of sensitivity on the channel depth, d, and the wall thickness, t. All other dimensions are based on the cantilever III design in Figure 3-1. The calculation assumes a density of 1 g/cm³ for the liquid and 3.2 g/cm³ for the walls, which corresponds to the values of our fabricated devices when filled with aqueous solution. Due to the higher density and larger cross-section area of the wall material, the sensitivity is dominated by t while

34

an increase in d from 0.5 μm to 5 μm only reduces sensitivity by ~50%.

The spring constant of the hollow cantilevers is of similar magnitude as that of a solid beam of the same total thickness. Finite element simulation yields k ~1 N/m for a force applied to the tip of the 300 μm long type III cantilever. Devices with subdivided channels are approximately twice as stiff, with k ~2 N/m for the type I and type II designs.[2] E=180 GPa and ν=0.24 were used for the Young's modulus and Poisson's ratio of silicon nitride [35]. Figure 3.1.1 shows the design of a hollow cantilever with an L-shaped gold trace on the glass lid 70 μm above the resonator for electrostatic excitation. The white areas are coated with chrome and connected to a common ground. To minimize bending due to the stressed chrome layer, the metal has been removed near the base of the cantilever and only covers the tip; a thin trace along the center of the beam connects the chrome pad on the tip to the rest of the chip.

The force developed by the electrostatic actuator depends on the gradient of the capacitance and on the applied voltage:

$$F = -\frac{1}{2}\frac{\partial C}{\partial x}V^2 \quad . \tag{3.1}$$

The capacitance between two crossed lines of width w_1 and w_2 separated by a gap x may be calculated using a semi-empirical model developed by Wong et al. [76]:

$$C(x_0) = 3.285 \cdot \epsilon_0 \frac{w_1 \cdot w_2}{x_0} \quad . \tag{3.2}$$

This equation is valid if the two conductors are much thinner than wide, as in this case the effect of the fringe field can be described by a numeric gauge factor. The overlap area between the cantilever and the electrode is 30×63 μm and $x_0 = 70$ μm, so that $C(x_0) = 0.79$ fF. The driving voltage V has the form $V(t) = V_B + v_{ac}\sin(\omega t)$, which yields

$$F_\omega(t) = \frac{C(x_0)}{x_0} V_B v_{ac}\sin(\omega t) \tag{3.3}$$

---

[2]Finite element calculations were performed with the ANSYS 5.7 software package. The geometry was meshed with 20 node 3D structural elements (solid186).
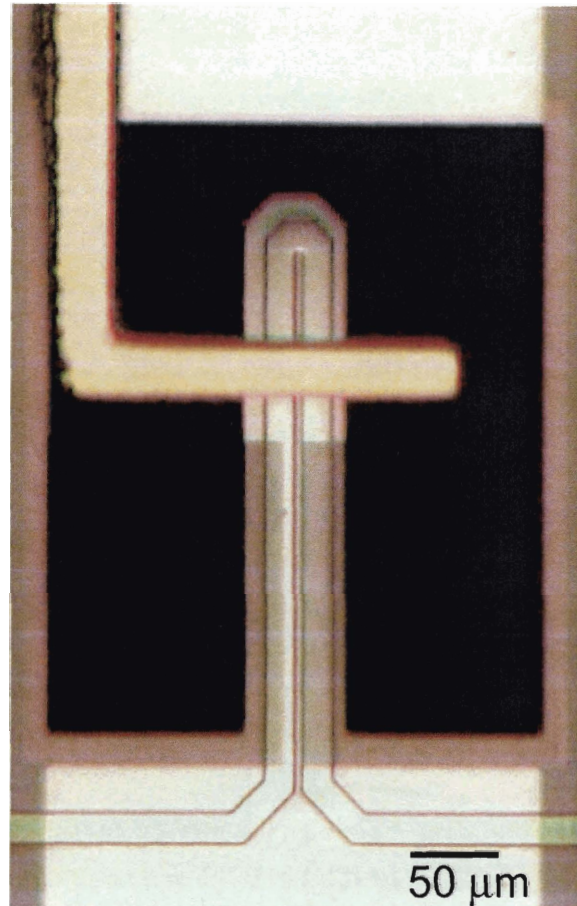
Figure 3-3: A 300 μm long and 63 μm wide cantilever containing a 20 × 1 μm fluid channel. The L-shaped electrode for electrostatic excitation is located on the glass lid ∼70 μm above the resonator surface. All white areas are coated with a 50 nm thin layer of Chromium.

for the force component at frequency ω acting on the cantilever. V_B is a static bias voltage that is applied in addition to the AC drive signal in order to increase the efficiency of the drive. Given the capacitance $C(x_0)$ and assuming a bias of 100 V, a force of ∼1 nN can be obtained. Since in reality the force is not concentrated at the cantilever tip the real amplitude is smaller than what would be predicted by F divided by the spring constant and multiplied by Q.

Flow inside a vibrating fluidic channel gives rise to a Coriolis force as indicated in Figure 3-4. If the mass flow is sufficiently large and if the resonator is appropriately designed, the Coriolis force can be exploited to excite a torsional mode whose amplitude may then be used to measure the flow rate. [16] The 300 μm long cantilevers
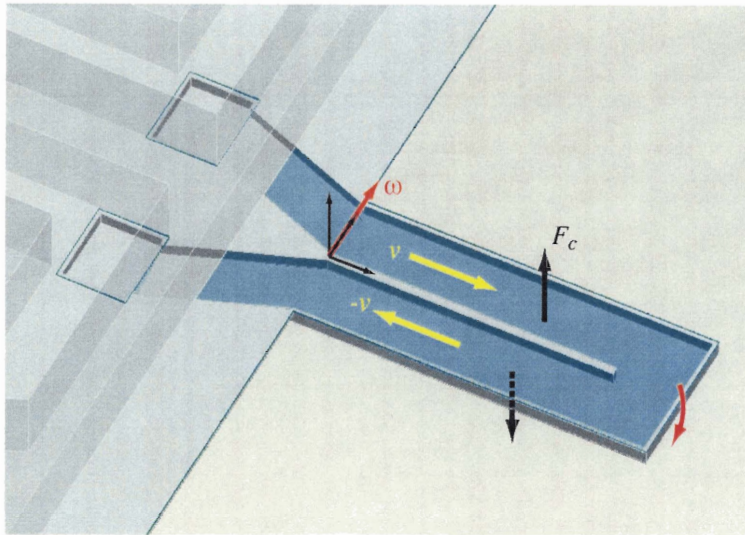
Figure 3-4: Flow inside a vibrating cantilever beam causes twisting due to the Coriolis force.
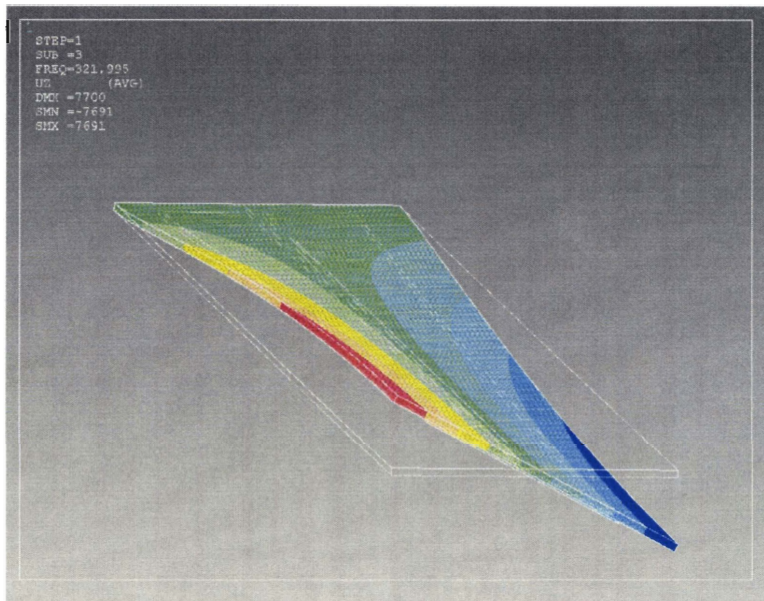
Figure 3-5: First torsional mode of a hollow cantilever beam (design III), f=322 kHz.

with a single 20 μm wide fluid channel whose first mode is at ~30 kHz possess the torsional mode shown in Figure 3-5 at 322 kHz.[3] Due to the large difference in frequencies no resonant amplification occurs. This is also true for the wider devices with four parallel channels, whose first torsional mode is at ~175 kHz. Since the fluid layer is very thin, the Coriolis force is weak even at high flow rates: The magnitude of the force per unit area, P, may be calculated from

$$P(x, z) = 2\rho \frac{q}{w} \omega_0 \frac{u(z)}{z} \tag{3.4}$$

where $w = W - 2t$ is the channel width, ρ the density of the fluid, and q is the volumetric flow rate given by

$$q = w \frac{d^3}{12\eta} \frac{P_{in} - P_{out}}{L_{channel}} \quad . \tag{3.5}$$

d denotes the channel height, η is the dynamic fluid viscosity, and $L_{channel}$ is the total channel length; P_{in} and P_{out} is the pressure at the inlet and outlet. Equation 3.5 is based on the simplifying assumption that the channel can be modeled by parallel plates, which is justified since $w/d \approx$ 10–20 for all of our devices. The Coriolis force acting on a device oscillating at 30 kHz with a maximum tip deflection of 1 μm and a flow rate of 1 nL/s is approximately $0.8 \cdot 10^{-6}$ N/m.[4] Integrated over a length of 300 μm this gives a total distributed force of 250 pN which, without resonant amplification, yields a maximum corner deflection of less than 1 pm. In conclusion, it can be said that the effect of the Coriolis force may safely be neglected in our resonator design.

3.1.2 Torsional resonators

The torsional resonators shown in the last column of figure 3-1 are significantly stiffer and have a higher resonance frequency than the cantilever resonators. They consist

---

[3]Calculated by finite element method

[4]1 nL/s is considered a high flow rate under typical experimental conditions, since it requires a pressure drop of ~100 psi between inlet and outlet of the resonator.
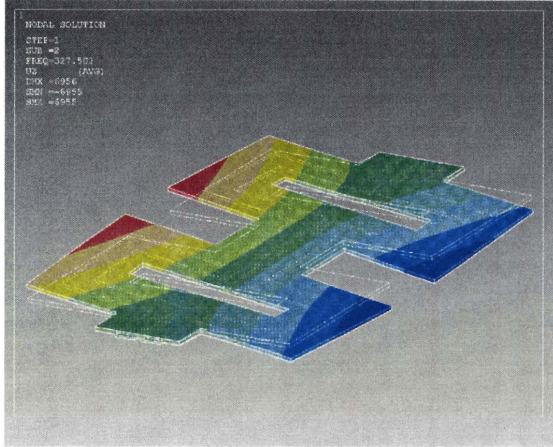
(a) First torsional mode, f=347 kHz. The two paddles vibrate in phase.
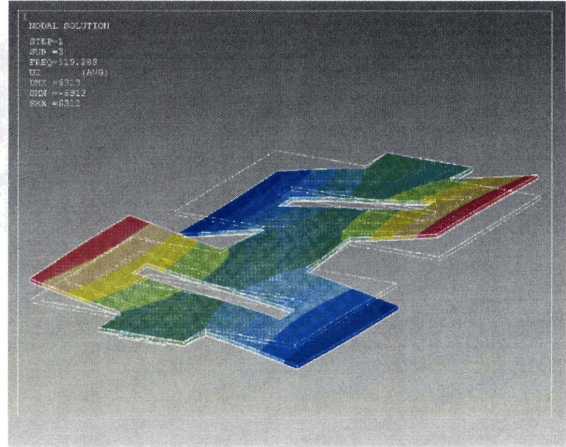
(b) Second torsional mode, f=519 kHz. The two paddles vibrate with opposite phase.
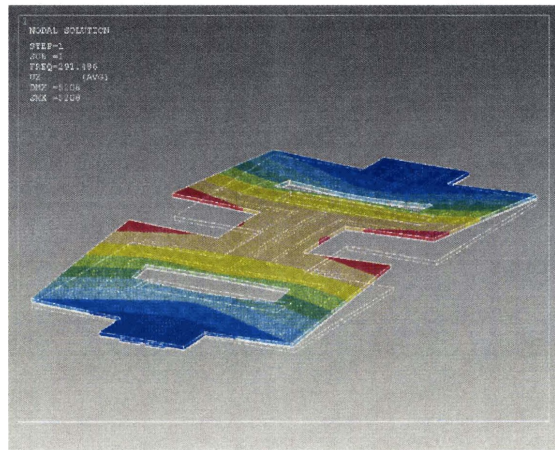
(c) First transverse vibration mode, f=291 kHz.

Figure 3-6: The first three modes of the two-paddle resonator are two torsional modes and one transverse vibration mode. The frequencies of all modes are sensitive to pre-stress, which has been assumed zero for the shown simulations. At 100 MPa tensile stress the simulated frequencies increase to 414 kHz for the transverse vibration (c), and 364 kHz and 558 kHz for the torsional resonances (a) and (b), respectively.
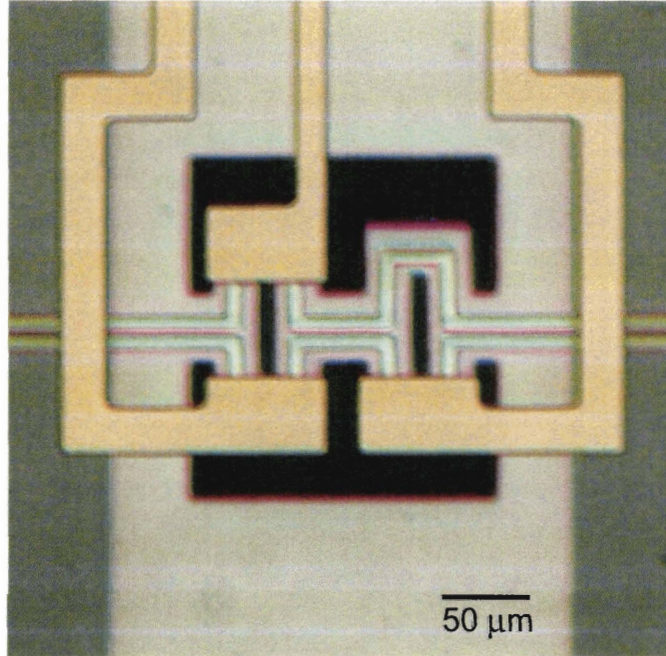
Figure 3-7: Torsional resonator with three pads for electrostatic actuation. The device contains two 10 μm wide and 1 μm deep microfluidic channels.

of two paddles that can resonate in phase, as shown in Figure 3-6(a), or out of phase, as shown in Figure 3-6(b). When operated in the out-of-phase mode, the resonator is balanced, meaning that little energy is lost through radiation into the substrate. When other damping mechanisms, most notably air damping, are small, optimizing the geometry can help to increase the quality factor and improve frequency resolution. In the presence of air damping, the quality factor generally improves with increasing resonance frequency [24]. Due to the small dimensions and the high stiffness, the torsional resonators have much higher resonance frequencies than the 300 μm long cantilever beams. Typically, the mode in which the paddles oscillate out of phase has a natural frequency of $\sim$600 kHz.

Figure 3-7 shows an optical micrograph of the torsional resonator. Three electrodes suspended 20 μm above the chrome coated device surface enable electrostatic excitation of the different modes. The first torsion mode is favored if the two adjacent electrodes at the bottom of the image are driven in phase, and the second mode is excited most effectively by driving two diagonally opposing pads with the same signal.

40

Besides the torsional vibration, the resonator can, in principle, also be operated as a doubly-clamped beam in transverse vibration. Driving the top and bottom pads on the left side while leaving the one on the bottom right unconnected would generate the vibration illustrated in Figure 3-6(c) at ~291 kHz. This mode is less preferred for practical purposes, since the detection with the optical lever method is more challenging. For small torsional resonators, the simplified theory derived in section 2.1 can only provide an estimate of the order of magnitude of the mass sensitivity.

3.2 Mass transport

A prerequisite for achieving high surface sensitivity with the suspended microchannel resonator is that the fluid layer is thin; this entails a small inner volume and a large aspect ratio of channel length to height. Consequently, sample molecules that have a high binding affinity to receptors on the channel wall can get rapidly depleted. Analyte depletion is a general concern for the detection of biomolecules in small volumes. Especially for the accurate determination of kinetic rate constants under non-equilibrium conditions it is crucial to ensure that reaction rates are not dominated by mass transport limitations. Although a detailed analysis of the transport phenomena in thin fluid channels is not the main subject of this thesis, enough insight is given to understand limitations of the current design and to identify important design criteria for future iterations.

The influence of flow rate, diffusivity, and sensor geometry on kinetic measurements has been studied extensively for commercial surface plasmon resonance based instruments whose flow chamber is a microfluidic channel of $50 \times 500 \times 2400$ μm $(h \times w \times l)$ cross section.[43] Although fluid flow and binding in microchannels is always governed by the same equations and boundary conditions, the mass transport in one micrometer tall channels is limited by a different mechanism than the transport in the SPR flow cell. The difference arises from the dramatically shorter diffusion time for biomolecules from the channel center to the wall: While transport of target molecules to a point on the surface of a 50 μm tall SPR channel is diffusion limited,

(a)   (b)
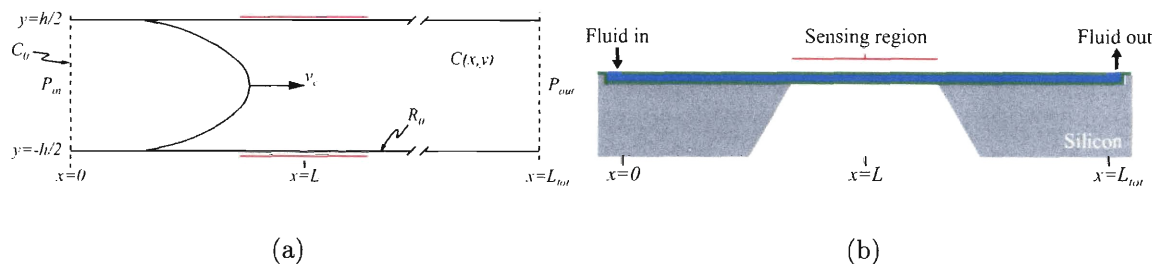
Figure 3-8: (a) The pressure drop $P_{in} - P_{out}$ drives the parabolic flow profile. The channel is approximated as two parallel plates. (b) Illustration of a possible implementation with the corresponding inlet/outlet and sensing regions.

the limitation in a 1 μm channel is due to convection. These regimes are characterized quantitatively by the Peclet number, $\text{Pe} = (v_c \cdot \frac{h}{2})/D$, and the aspect ratio, $l/(\frac{h}{2})$, where v_c is the flow velocity at the center of the channel, D is the diffusion coefficient, and h and l is the channel height and length.[5] In SPR, $\text{Pe} \gg l/(\frac{h}{2})$ for all large proteins, while for our device $\text{Pe} \approx l/(\frac{h}{2})$.

Fast diffusion compared to convection in the thin channel does not by itself imply that binding will be flow rate limited. Analyte depletion is also a function of the binding rate constant and the density of receptors on the walls. Figure 3-8(a) introduces the notation for the following analysis. A possible implementation with the corresponding sections along the x-coordinate is shown in Figure 3-8(b). The pressure difference $P_{in} - P_{out}$ generates a parabolic flow profile with the maximum velocity

$$v_c = \frac{h^2}{8\eta} \frac{P_{in} - P_{out}}{L_{tot}} \quad . \tag{3.6}$$

In Equation 3.6, η denotes the dynamic viscosity of the fluid. An analyte of interest, A, is present in the flow stream at concentration $C(x, y, t)$, which decreases continuously along the channel due to loss of analyte to the immobilized receptors. The reaction is modeled as

$$A + R \rightleftharpoons AR \tag{3.7}$$

---

[5]Typical numerical values are: $D=10^{-6}$ cm^2/s, $v_c=5$ cm/s (both, SPR and our sensor). SPR: $h=5 \cdot 10^{-3}$ cm, $l=0.24$ cm, our sensor: $h=1 \cdot 10^{-4}$ cm, $l=0.03$ cm

42

with forward and reverse rate constants k_a and k_d. R is the free receptor concentration on the walls, which decreases over time from its initial value R_0 while satisfying the rate equation

$$\frac{\partial R}{\partial t}(x,t) = k_a C(x,t)|_{wall} \cdot R(x,t) - k_d \Big(R_0 - R(x,t) \Big) \quad . \tag{3.8}$$

The concentration profile evolves according to the diffusion/convection equation

$$\frac{\partial C}{\partial t} = D \frac{\partial^2 C}{\partial y^2} - v_c \left(1 - \left(\frac{y}{h/2} \right)^2 \right) \frac{\partial C}{\partial x} \tag{3.9}$$

where D is the diffusion coefficient, and axial diffusion is considered negligible compared to the convective transport. The boundary conditions to Equation 3.9 are:

$$C(0,y,t) = C_0, \qquad D\frac{\partial C}{\partial y}\Big|_{y=\pm\frac{h}{2}} = \mp\frac{\partial R}{\partial t}, \qquad \lim_{x\to\infty} C(x,y,t) = 0 \tag{3.10}$$

The equilibration time for most biochemical reactions is significantly longer than the convection time v_c/L_{tot}. Therefore, a quasi-stationary solution $C(x,y)$ can be found for any given time. Although the equation is non-linear due to the coupling of C and R at the channel walls, a worst case estimate of the sample depletion at $t{=}0$ can be obtained analytically. Through appropriate scaling the result becomes independent of the particular sensor geometry:

$$\tilde{x} = \frac{x}{\left(\frac{v_c \cdot (h/2)^2}{D} \right)}, \qquad \tilde{y} = \frac{y}{h/2}, \qquad c(\tilde{x},\tilde{y}) = \frac{C(x,y,0)}{C_0} \tag{3.11}$$

$$\kappa = k_a R_0 \frac{(h/2)}{D} \tag{3.12}$$

Equation 3.9 with the assumption of stationarity becomes

$$\frac{\partial^2 c}{\partial \tilde{y}^2} = \left(1 - \tilde{y}^2 \right) \frac{\partial c}{\partial \tilde{x}} \tag{3.13}$$

43
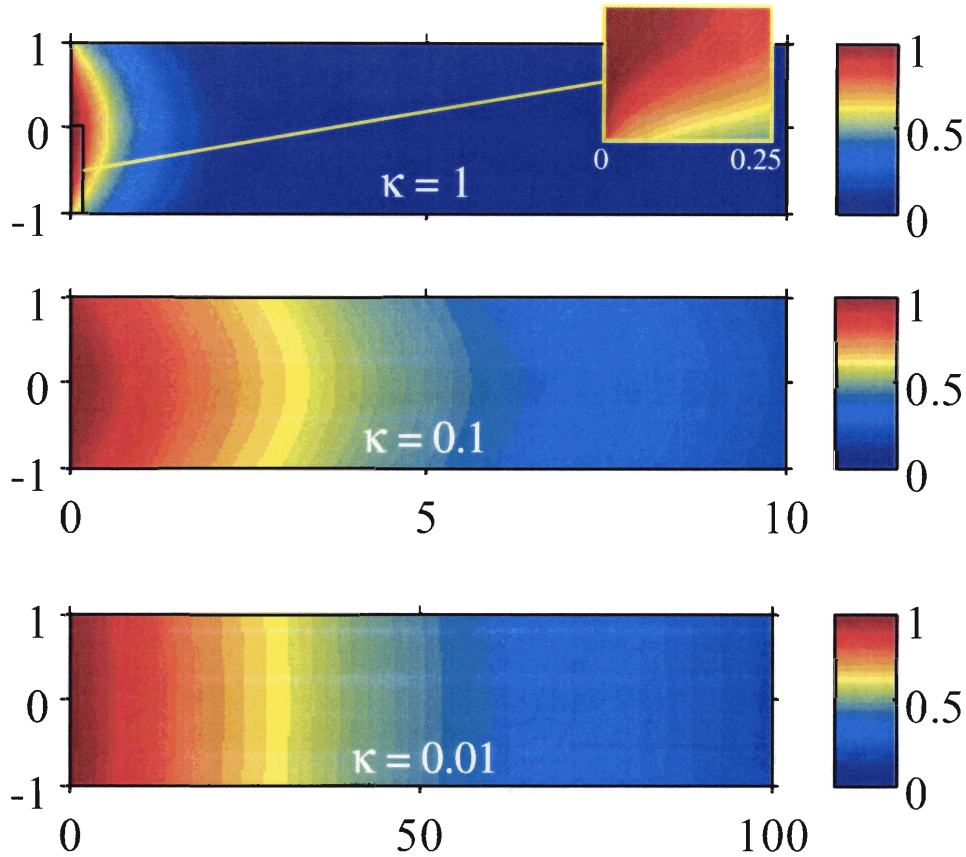
Figure 3-9: Relative sample concentration in a channel cross section shortly after injection for three different reaction rates κ. κ=1 represents a fast interaction. The axial position is measured by the number of times a target molecule entering at $\tilde{x}$=0 could diffuse from the channel center to the wall, with $100 \,\hat{=}\, 1$ mm for a typical geometry and diffusivity.

with boundary conditions

$$c(0, \tilde{y}) = 1, \qquad \left.\frac{\partial c}{\partial \tilde{y}}\right|_{\tilde{y}=\pm 1} = \mp \kappa \cdot c(\tilde{x}, \pm 1), \qquad \lim_{\tilde{x} \to \infty} c(\tilde{x}, \tilde{y}) = 0 \qquad (3.14)$$

The dimensionless coordinate $\tilde{x}$ corresponds to the number of times a probe molecule injected at the channel center could diffuse to the channel wall before reaching the axial position x.

Equation 3.13 with the boundary conditions 3.14 has been solved analogous to Brown's method, [4] and the solution for three different values of the normalized reaction rate constant κ is plotted in Figure 3-9. The illustrated length scales are

typical for devices with a channel height of $\sim 1\ \mu$m and realistic values for flow rate, diffusivity and detector length (assuming 10-100 kDa proteins and 1-10 atmospheres pressure drop). The values of κ shown cover most biological systems of interest, with $\kappa=1$ representing a fast reaction, and $\kappa=0.01$ representing a slow reaction. The main difference between the three scenarios is their respective suitability for measurements of kinetic rate constants. Pure detection is always possible, since, even in the case of strong depletion, the walls will eventually saturate. In the case where $\kappa \geq 1$, the sample is almost fully depleted after less than one characteristic length, which makes determining kinetic parameters difficult. If the channel height is increased to $h \geq 3\ \mu$m, the quadratic dependence of flow rate and diffusion time on h rapidly lead into a fully reaction limited regime in which the concentration distribution between inlet and outlet resembles that depicted in the inset in Figure 3-9. For slow reactions ($\kappa=0.01$), the mass transport limitation is much less significant even at $h=1\ \mu$m: After ten characteristic lengths, the sample concentration is still $\sim 90\%$ of the injection concentration.

3.3   Chip layout

The sensor chips for the cantilever devices II and III as well as the torsional resonators described in Figure 3-1 were fabricated on the same wafer and packaged with the glass frit process described in section 4. Each chip contains two resonant sensors that share a common ground connection and are individually addressable through separate excitation electrodes. The fluidic connections for the two devices are also separate, with one large volume (~ 20 nL) microfluidic bypass connecting to the inlet, and another similar bypass connecting to the outlet of each of the two thin silicon nitride channels. One chip therefore requires a total of eight fluid inlets, which are made via through-holes that connect to tubes on the backside of the chip.

Figure 3-10 illustrates the global layout of the sensor chip. The through holes are spaced on a 4×3 mm grid that enables sealing by standard size (-001) O-rings. Microfluidic channels in the glass lid are etched 50 μm deep and connect the inlets to

45

the resonator; these channels are sealed by lines of glass frit. The frit has the ability to bond over metal traces as well as to seal over the thin silicon nitride channel whose surface is depressed by approximately 150 nm as a result of dishing of the CMP (see section 4). All electrical contacts except for the ground connection to the resonator surface are located on the glass lid where they are routed to bond pads on the edge of the chip without crossing the fluid channels. Since the glass frit that joins the silicon chip and the glass lid is a line pattern that covers a relatively small area, there is a narrow gap separating the two surfaces. This gap is filled on one side of the chip with colloidal silver particles. The particles aggregate after evaporation of the solvent and make an electrical connection between the chrome on the silicon chip (not shown) and a large gold pad on the glass lid. The resonator surface can now be tied to ground via a wirebond to the glass. The layout of the area to which the conductive silver paint is applied is indicated in Figure 3-10.
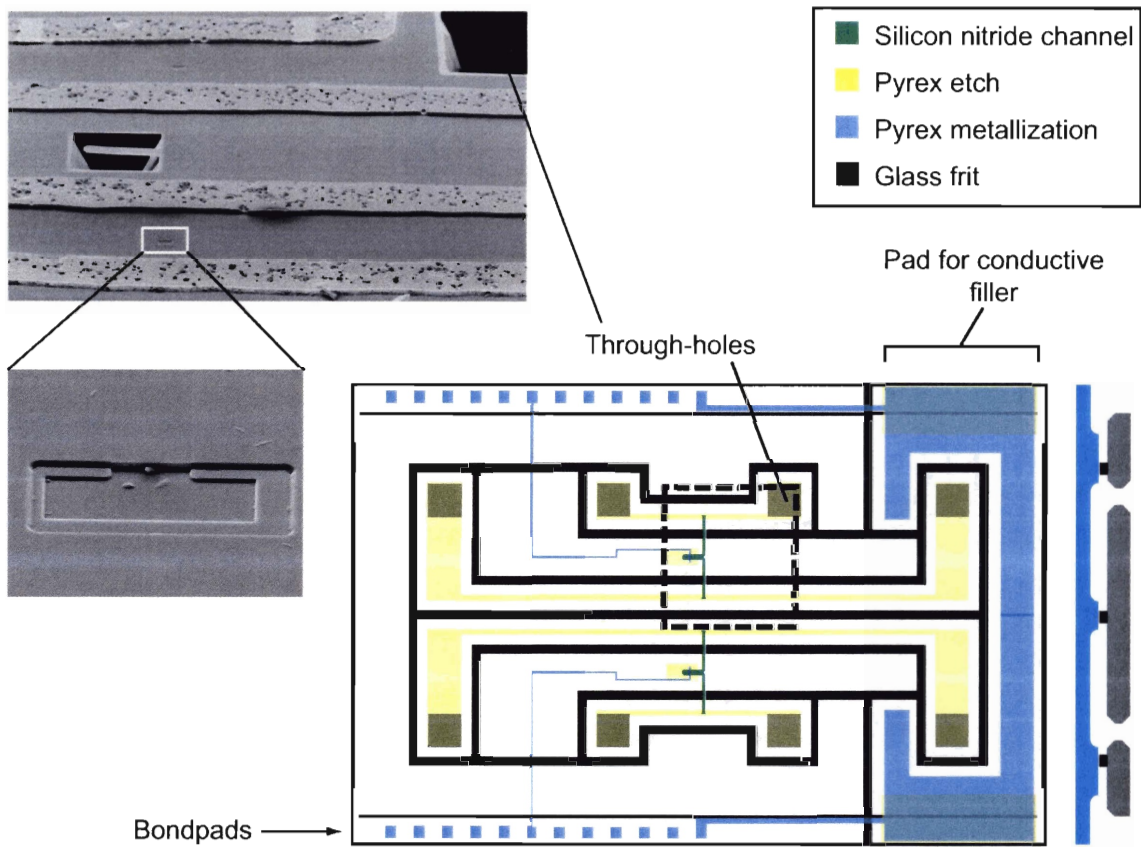
Figure 3-10: Chip layout: Each die contains two independently addressable suspended microchannel resonators. Fluids are injected via through-holes in the silicon and flow to the resonator inlet (electron micrograph) through microfluidic channels that are sealed by glass frit.

Chapter 4

Fabrication and Packaging

High sensitivity to surface bound mass in vibrating tube resonant mass sensors requires a large ratio of surface area to channel volume and wall thickness. The fabrication of the suspended microchannel resonators in this thesis is based on a sacrificial polysilicon process with low-stress low-pressure chemical vapor deposited (LPCVD) silicon nitride as the structural material. Channels with a total length up to 2 mm and a height of ~ 1 μm were fabricated without noticeable slowing of the etch rate due to mass transport effects, which is often limiting in sacrificial silicon dioxide processes. The ability to complete the sacrificial release without the need for access holes along the channel not only simplified the process, but also avoids degradation of the sensitivity by the mass of an additional layer that would otherwise be required to re-seal the release holes. While the fabrication of micron- and sub-micron channels with sacrificial etching of polysilicon has been reported before, [2, 66] we are not aware of any prior demonstration of a process that can yield hollow resonators with the thin walls, long channels, and an interface to conventional microfluidics required for our work.

Microfluidic packaging, in particular the use of micromolded poly(dimethylsiloxane) (PDMS) microfluidics, is facilitated by the use of a Damascene process which yields thin silicon nitride channels buried under a planarized wafer surface. In a conventional process, the silicon nitride channels would protrude out of the wafer surface by ~ 2 μm. The channels would then be impossible to seal with packaging technolo-

gies that can not conform to this topography, and released devices would be more susceptible to damage during contact lithography and backside processing.

Suspended microchannel resonators were fabricated on standard six inch ⟨100⟩ silicon wafers and then packaged on the chip level with PDMS microfluidics or on the wafer scale by bonding the device wafer to a pyrex capping wafer. The fabrication of suspended silicon nitride channels is described in the following section, and modifications to this process that pertain to a particular packaging method are pointed out in sections 4.2.1 and 4.2.2. [6, 7]

The two main functions of the first-level package are to enable efficient fluid delivery and to provide contacts for electrostatic actuation of the resonators. Since the suspended microchannels are bulk micromachined, the electrodes can not be fabricated underneath the channels. Furthermore, the package has to be transparent in order to enable optical readout of the cantilever vibration; optics is the preferred method for this application since its low noise allows for the most precise measurement of resonance frequency without sophisticated on-chip electronics.

4.1 Silicon process

The process flow for the fabrication of suspended silicon nitride channels is illustrated in Figure 4-1. First, the channels were etched to a depth of 1 μm using reactive ion etching (RIE) in sulfur hexafluoride (Figure 4-1(a)). This etch was done in a South Bay Technologies RIE 2000 system at 35 mTorr, 50 W forward power, and 60 V DC bias. The wafers were then coated with 800 nm low-stress LPCVD silicon nitride (Figure 4-1(b)) followed by 1.5 μm LPCVD polysilicon. Low-stress silicon nitride was deposited from a 10:1 ratio of dichlorosilane and ammonia in an SVG/Thermco 7000 vertical thermal reactor at 775°C and 250 mTorr. A refractive index n=2.278 was measured by multiple-angle ellipsometry[1] at 632.8 nm; $n \sim 2.2$ is a characteristic value for low-stress silicon rich Si_xN_y. Although the residual stress was not characterized in this process, literature values for films obtained under similar conditions

---

[1]Sentech SE400 ellipsometer
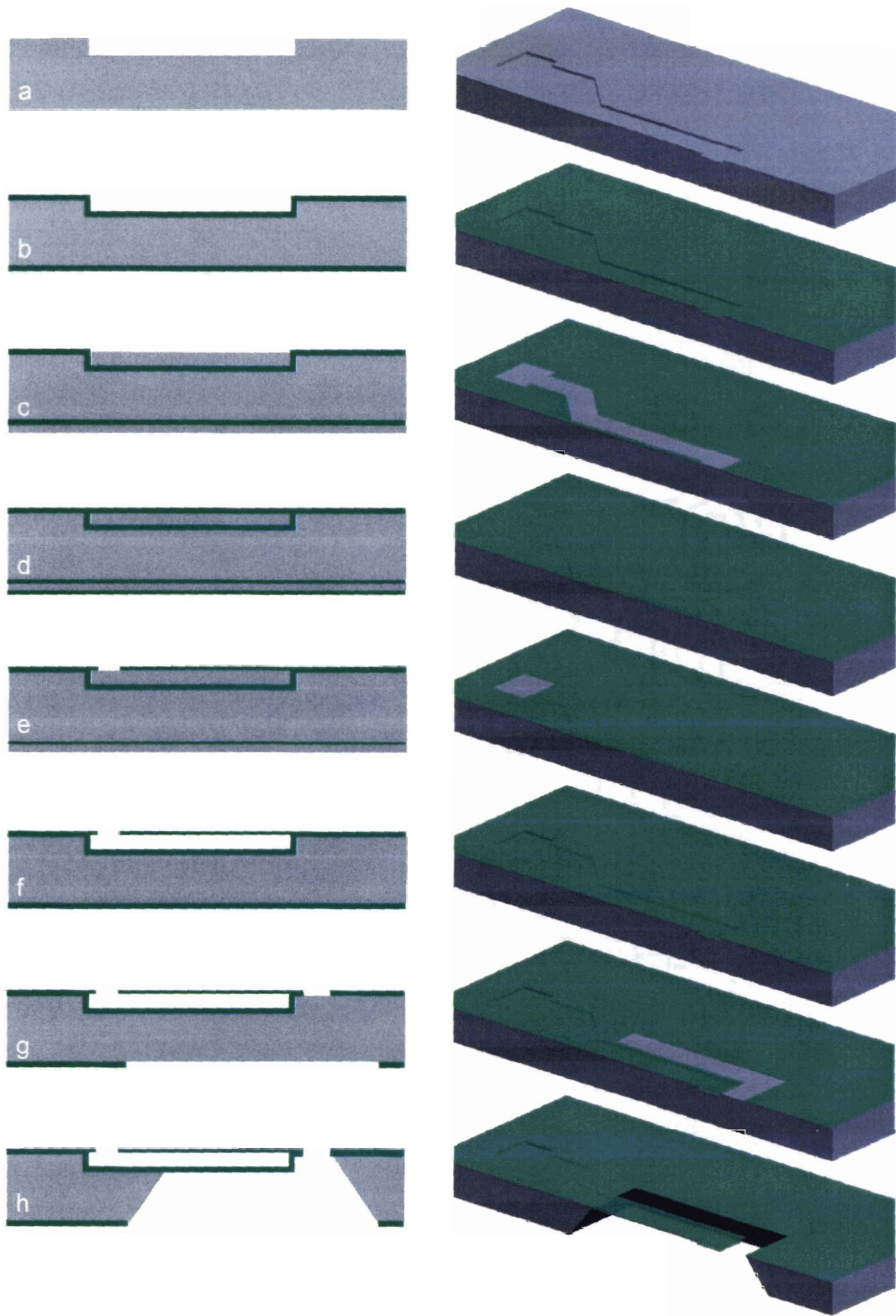
Figure 4-1: Basic process for the fabrication of low-stress silicon nitride suspended microchannel resonators.
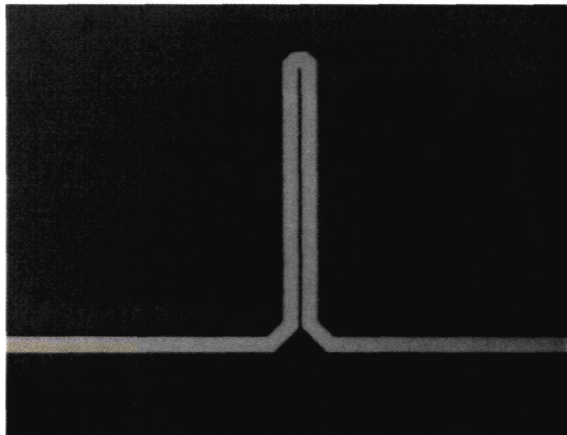
(a) After the CMP only the 1 μm deep channels are filled with polysilicon, and the first silicon nitride layer is exposed on the wafer surface.
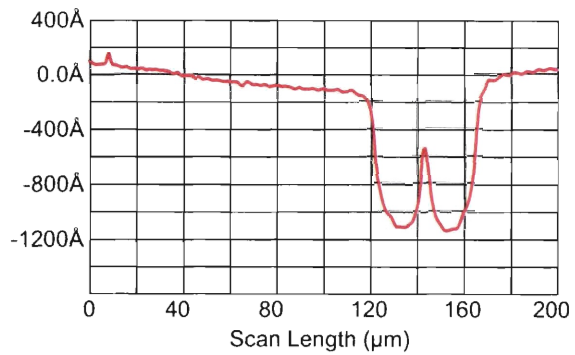
(b) Surface topography after CMP.

Figure 4-2: Channel pattern and surface topography after polysilicon CMP.

Table 4.1: CMP parameters

Machine	Strasbaugh 6EC
Slurry	Cabot Semi-Sperse 25 : H2O (1:1)
Table speed	25 rpm
Chuck speed	40 rpm
Down force	3.0 psi
Rate	60 nm/min

and with similar refractive index suggest a low tensile stress on the order of 50–100 MPa.[30, 68] The LPCVD polysilicon was deposited thicker than the depth of the etched trenches, so that subsequent removal of the layer by chemical-mechanical polishing (CMP) left the channels filled, as shown in Figures 4-1(c) and 4-2(a). The depression of the channel area relative to the wafer surface, which is seen in the profilometer scan in Figure 4-2(b), is the result of a slight difference in polishing rates between silicon nitride and polysilicon as well as the compliance of the polishing pad. This phenomenon is usually termed "dishing" in the CMP literature, and various techniques have been developed to minimize its effect in Damascene processes. [8, 33]
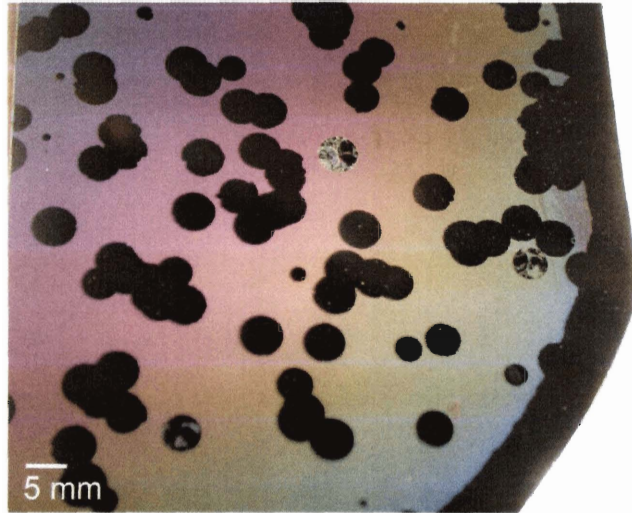
Figure 4-3: Defects in the second silicon nitride layer on the wafer backside lead to etching of the polysilicon underneath. The circularly undercut areas later delaminate and cause high particle counts. This problem does not occur if the nitride is stripped from the backside before the sacrificial etch.

The degree of dishing observed in our channel structures did not cause any complications with subsequent processing steps or with the operation of the device.

Table 4.1 summarizes the parameters used for the polysilicon CMP. Since the pads and slurry were not optimized for selectivity to silicon nitride, the process needed to be timed to stop as soon as the polysilicon was completely removed. Excessive thinning of the silicon nitride due to over-polishing was not a concern since the polishing rate as well as the initial layer thickness was uniform to within 10% across a six inch wafer. The timing was optimized once at the beginning of each lot by polishing a monitor wafer with frequent visual inspection until no patches of polysilicon remained; even nanometer thin residues were easily discerned from silicon nitride due to the metallic appearance of the poly and the contrast in hydrophobicity, which caused water to peel off from the silicon and collect in areas where the hydrophilic silicon nitride had been exposed. After the CMP, a second layer of low-stress LPCVD silicon nitride was deposited to close the microchannels (Figure 4-1(d)), and holes were etched into this layer to provide access to the polysilicon underneath (Figure 4-1(e)). The polysilicon was then dissolved in a six molar aqueous solution of potassium hydroxide (KOH) at
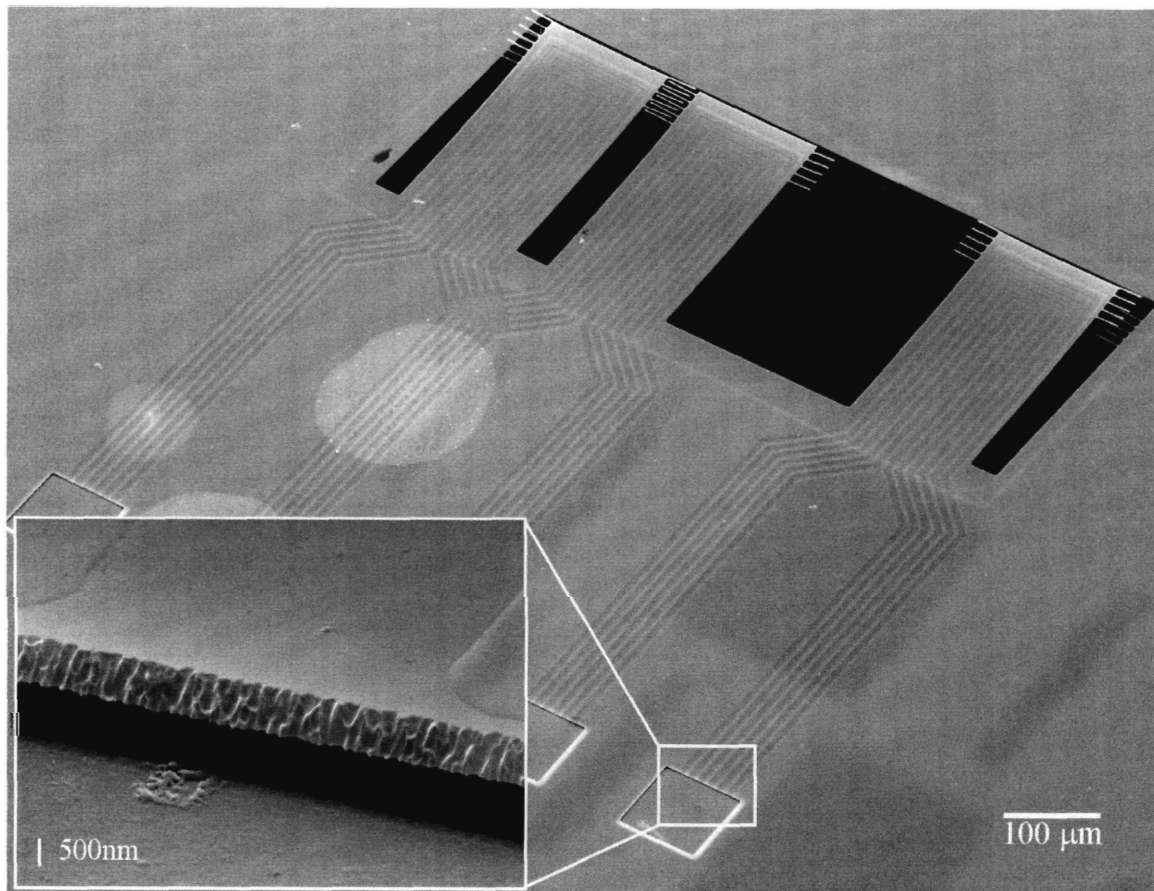
Figure 4-4: Electron micrograph showing three 300 μm long cantilevers, each containing six parallel 8 μm wide and 1.2 μm deep fluid channels. The total volume inside each resonator is ~30 pL. The inset reveals the narrow gap between the top and bottom silicon nitride diaphragms that form the cantilever.

80°C, as illustrated in Figure 4-1(f); this etch took approximately 20 h to complete, which is consistent with the etch rate we observed for the $\langle 100 \rangle$ plane of bulk silicon in KOH under similar conditions. The top nitride layer had been removed from the wafer backside by RIE prior to the sacrificial release, so that the polysilicon was stripped and the lower layer of silicon nitride was revealed. Omitting this step often gave rise to circularly undercut spots as shown in Figure 4-3 due to small defects in the top nitride that enabled the KOH to attack the polysilicon layer sandwiched between the first and second nitride film. Delamination of these areas later caused unacceptably high particle counts.

The long polysilicon etch was followed by another patterning step on the silicon

nitride to create the outline of the resonators and to define the locations of through-wafer holes for fluid injection ports. RIE was used to etch through both nitride layers on the front side of the wafers, and through the one remaining layer on the backside, as illustrated in Figure 4-1(g). Depending on the backside mask, the resonators were released either from the front side, or, as shown in Figure 4-1(h), from both sides of the wafer. Photoresist was usually drawn into the hollow channels by capillary action, but the resist could easily be removed using a mixture of sulfuric acid and hydrogen peroxide (Piranha solution, 3:1 H_2SO_4:H_2O_2). The 800 nm thin channel lids rarely cracked or collapsed despite the use of contact alignment and backside processing, during which the wafers were placed upside-down on vacuum chucks. The average yield after the RIE was typically better than 90%.

Finally, the suspended channels were released by anisotropic etching of silicon in KOH (6 M) or in tetramethyl ammonium hydroxide (TMAH) solution (10% in water),[2] both at 80°C. An electron micrograph of an array of three hollow cantilevers is shown in Figure 4-4. The sacrificial layer etch and the final release of the suspended structures was carried out in two separate steps in order to avoid excessive undercut due to the finite selectivity between $\langle 100 \rangle$ and $\langle 111 \rangle$ planes of single crystal silicon in alkali etchants: the total etch time in a combined release process is determined by the time required to dissolve the sacrificial layer, which, given our channel design, was approximately four times longer than that for a through-wafer etch. For channel designs with a total length up to $\sim$1 mm, a single release at the end of the process would be sufficient.

4.2 Packaging

4.2.1 PDMS packaging

The packaging method described in this section is based on soft lithography in poly(dimethylsiloxane) (PDMS) as described by Xia and Whitesides [78]. Thin gas-

---

[2]TMAH was used in conjunction with chromium metallization for the glass frit bonding process described in section 4.2.2

55
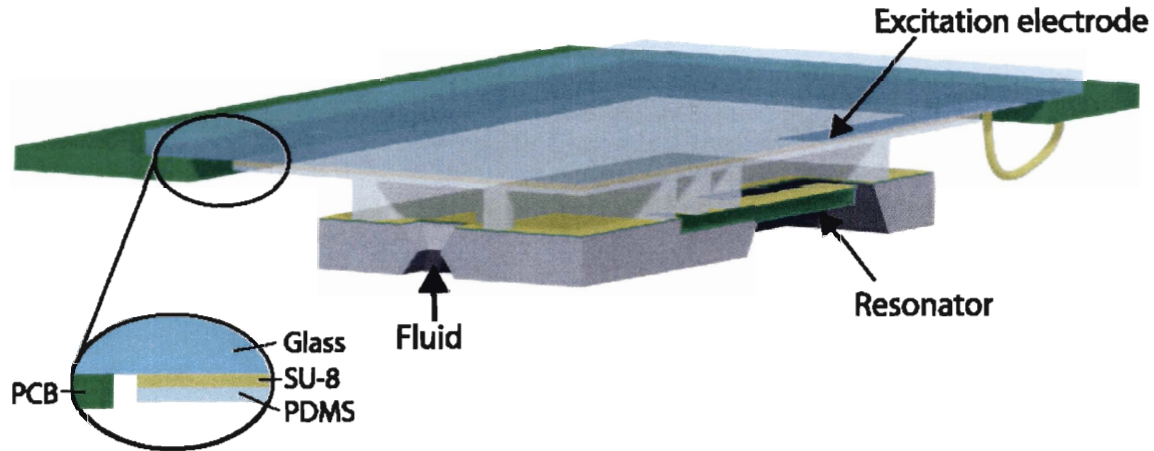
Figure 4-5: Fluid is delivered to the resonator through a ~50μm thin PDMS microfluidic layer. The small gap between the glass carrier and the chip enables efficient electrostatic excitation of the resonator. The PDMS is bonded to the glass in selected areas via an intermediate layer of SU-8.

kets of PDMS are micromolded and then bonded in selected areas to a metallized and patterned carrier substrate; the substrate is glass, which enables the use of optics for the resonance frequency readout. The new method combines many of the advantages of conventional soft lithography and thin elastomer gaskets on rigid supports [32, 50, 51] with the robustness and substrate independence of intermediate layer bonding. While the process flow was specifically developed for the resonant sensor that is the basis of this work, the result is a general technique which can be used to package other microfluidic devices. The silicon device fabrication prior to packaging is carried out as described in section 4.1, with the additional deposition of 25 nm gold on a 5 nm thick chromium adhesion layer onto the finished device surface. The metal was deposited by electron beam evaporation after the final release etch. Bending of the cantilevers as a result of residual stress in the metal was minimized by evaporating layers of matched thickness on both sides of the device. Figure 4-5 illustrates the components of the fully packaged device. Fluid enters the sensor chip from the backside via a through hole in the silicon substrate. On the front side, the sample is distributed through 50 μm tall microfluidic channels which are formed by a thin
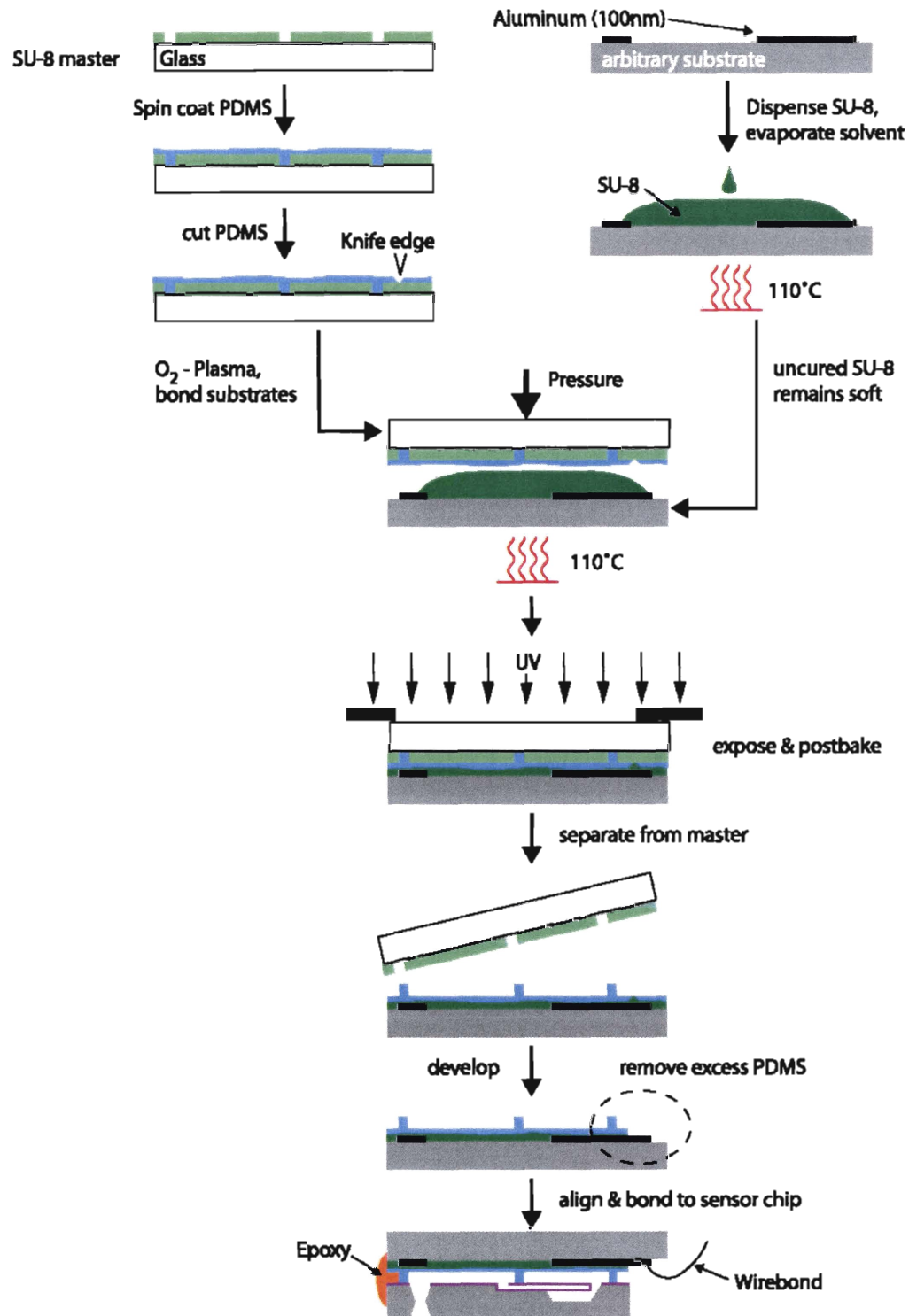
Figure 4-6: Thin PDMS gaskets are fabricated by micromolding against an SU-8 master and then transferred to a metallized and patterned carrier substrate. The PDMS is transferred via a thin layer of SU-8. A permanent bond is formed in lithographically defined areas so that excess PDMS can be easily removed in areas required for wire bonding. The final package is encapsulated with a 100% solids gap filling epoxy.
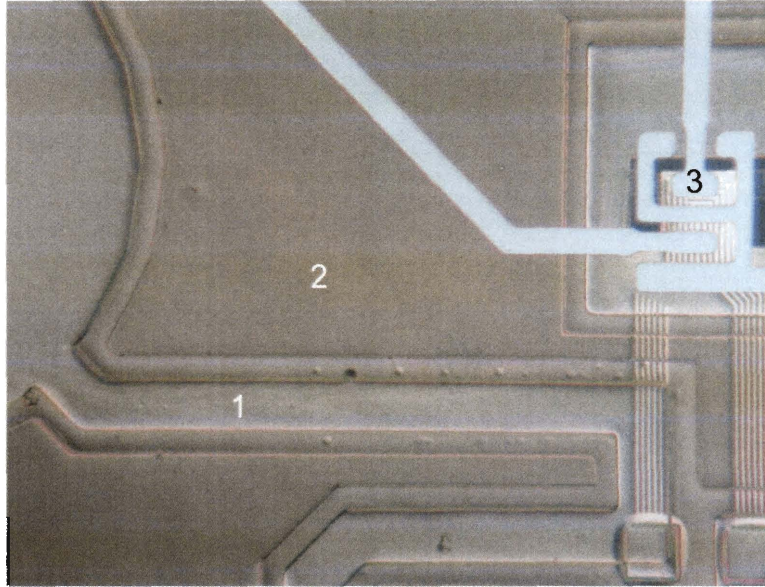
Figure 4-7: A thin gasket of PDMS separates the microfluidic channels (1) from areas filled with a solvent-free epoxy (2). The epoxy bonds the gold coated device chip to a glass substrate containing electrodes (3) for electrostatic actuation of the resonator.

PDMS gasket. The gasket is bonded to a glass substrate on which the excitation electrode has been patterned. The PDMS is attached to the glass via a thin intermediate layer of SU-8 photoresist. Since the wirebond pads need to stay clear, the bonding is carried out locally. Fabrication of the thin gasket starts by spin coating PDMS onto an SU-8 master and curing as illustrated in Figure 4-6. After curing, the elastomer is cut with a razor blade, generating square islands which are to be transferred to a new carrier. The receiving carrier in this work has been glass with patterned aluminum traces, and any other material to which SU-8 adheres may be used if optical clarity is not required. Bonding is carried out in two steps: First, a drop of SU-8 is dispensed onto the receiving substrate, soft-baked, and squeezed to a thin film with the PDMS coated master. Second, the stack is cooled to room temperature and the islands to be transferred are exposed to UV light. When the substrates are separated, the PDMS adheres strongly to the new carrier and peels of from the master. Developing in PM Acetate finally lifts off the PDMS in areas where the SU-8 was not cross-linked. On the chip side, the PDMS also can not be bonded directly since the surface is coated with gold. Bonding of the two substrates is achieved by bringing them into

contact and then dispensing a small drop of solvent-free epoxy[3] onto the gap. The PDMS gasket seals against the chip surface and prevents the epoxy from entering the microfluidic channels. In order to ensure good wetting and adhesion the PDMS is plasma activated before performing this step. Finally, the device is mounted onto a printed circuit board (PCB) and wirebonded. The electrical connection to the gold surface of the silicon chip is made through application of a conductive filler that is dispensed in an area not filled by the epoxy.

Figure 4-7 illustrates the layout of the different package components: The PDMS gasket surrounds the microfluidic channels and a rectangular cavity for the resonator in a 50 μm wide racetrack pattern. The areas outside the channels are filled with epoxy, which has good adhesion to the substrate carrying the PDMS gasket as well as the gold surface of the resonator chip. The white traces in the upper right of Figure 4-7 are 100 nm aluminum lines located on the glass lid $\sim$50 μm above the surface of the silicon chip; these are used for electrostatic excitation of the resonator. The racetrack design has the advantage of minimizing the area occupied by PDMS and maximizing the area available for bonding. In addition, the package is highly tolerant to minor particulate contamination; particles only prevent bonding if they interfere with one of the PDMS features, which is rare because of the small area of the gasket. The epoxy easily flows around and encapsulates small particles. The quality factor of a resonator packaged by the above method is limited by squeeze film damping due to the narrow gap and the air at atmospheric pressure that surrounds the vibrating beam. Figure 4-8 shows the frequency response of a 300 μm long cantilever. The quality factor of this device was limited to 25, although other identical resonators that had not been packaged exhibited a Q of $\sim$90 when driven with an electrode consisting of a sharp tip that was positioned close to the cantilever using a micrometer stage. The gap size can be adjusted to yield the best trade-off between squeeze film damping and electrostatic drive efficiency, yet air damping will always limit the quality factor when a polymer package is used.

---

[3]Epotek 377 from Epoxy Technology, Billerica (MA)
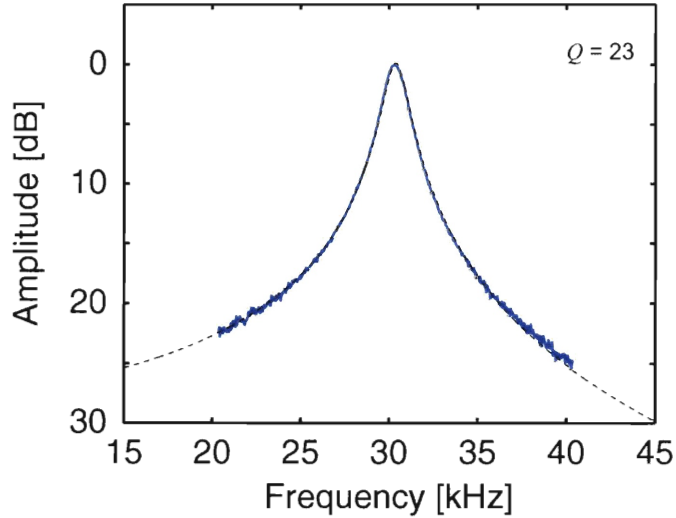
Figure 4-8: Squeeze film damping of a PDMS packaged cantilever resonator with a gap of <50 μm limits the quality factor to ~25. As the gap size is increased, Q eventually rises to ~90 and is then limited by viscous drag.

4.2.2 Glass packaging

A hermetic package based on inorganic materials provides a wider range of chemical compatibility and enables better frequency resolution than a polymer package; systematic errors and noise due to air currents, humidity or particles are completely eliminated, and a significantly higher quality factor may be achieved through vacuum encapsulation. The process flow described in section 4.1 has been combined with a wafer-scale approach to fabricate vacuum encapsulated suspended microchannel resonators with microfluidic interconnects etched into a glass cap.[4] The extended process flow chart including the fabrication of the pyrex capping wafer is depicted in Figure 4-9. The silicon process follows the same sequence as described above up to step (c) in Figure 4-9. After dissolving the sacrificial polysilicon layer in hot potassium hydroxide the wafers were rinsed and dried, and a 50 nm layer of chromium was deposited by ion beam deposition. The purpose of the chromium layer is to provide high reflectivity for the optical readout and, at the same time, to serve as an electrode for electrostatic actuation (Figure 4-9(d)). The chromium was then patterned

---

[4]Process development was done in collaboration with Innovative Micro Technology (Santa Barbara, CA)
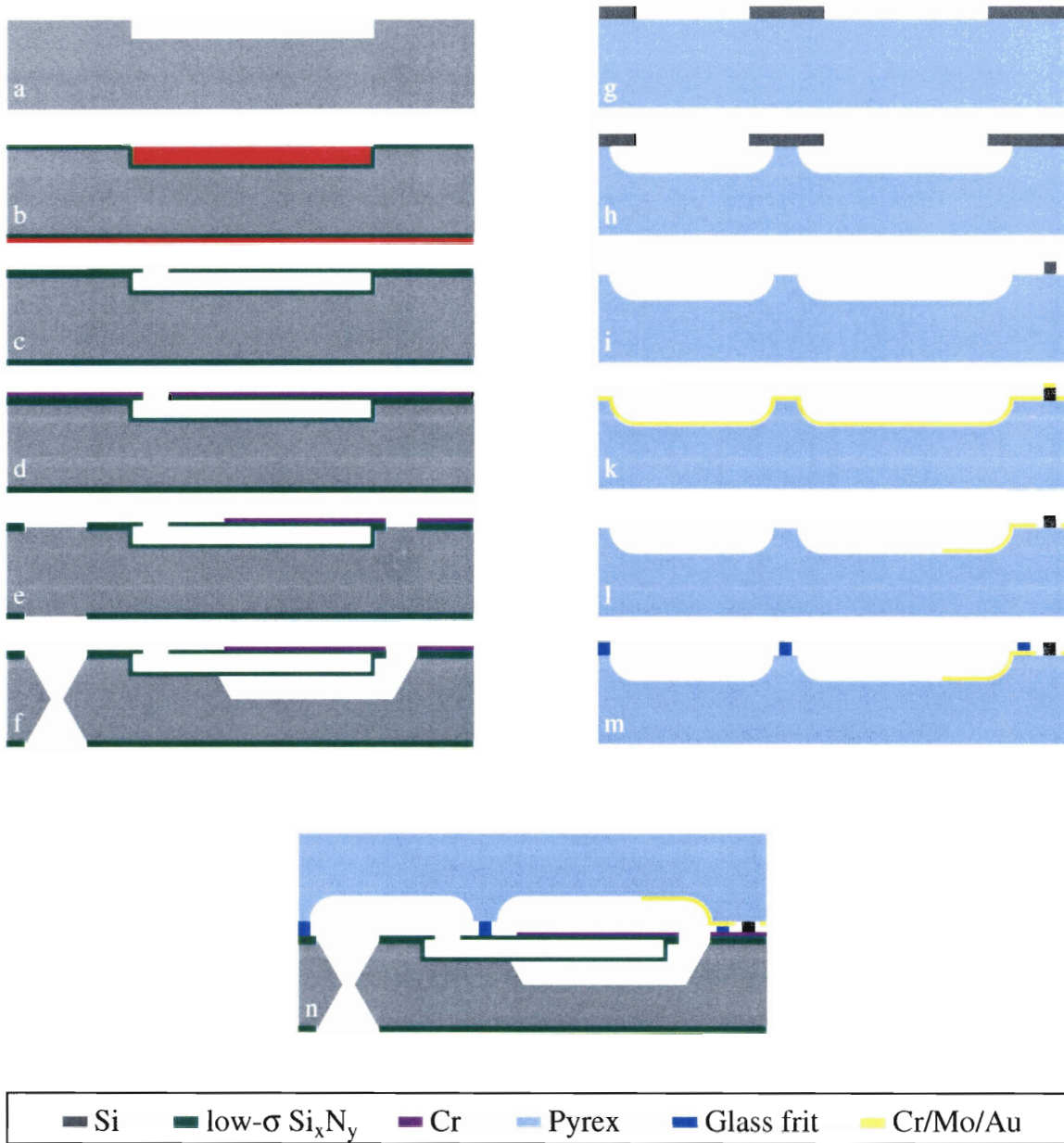
Figure 4-9: Process flow for fabrication and wafer-level vacuum packaging of suspended microchannel resonators.

in order to minimize stress on the resonator and to remove the metal from all areas that would later be in contact with the sample fluid. We subsequently dry etched through both silicon nitride layers to create the resonator outline and open areas for through-wafer holes for sample delivery. The backside of the wafers was also patterned and etched in the same step, thus enabling etching of the fluid vias from two sides (Figure 4-9(e)). Finally, the resonators were released by bulk micromachining in tetramethylammonium hydroxide (TMAH), which is compatible with chromium metallization (Figure 4-9(f)).

The first level packaging for the suspended microchannel resonators was done on the wafer scale: A glass wafer providing microfluidic channels as well as electrical interconnects for electrostatic actuation was attached to the device wafer by glass frit bonding. Glass frit has the ability to bond over metal traces and, at the same time, maintain a good vacuum seal for extended periods of time. [60] Fabrication of the glass capping wafer required etching deep ($\sim$50 μm) recesses to form microfluidic channels and cavities for the resonators. Furthermore, electrodes for electrostatic actuation needed to be integrated, and hard spacers of $\sim$20 μm height had to be formed to limit the compression of the glass frit during bonding. The mask for the deep channel etch in hydrofluoric acid (HF) was formed by a silicon wafer which was first anodically bonded to the glass, then etched back to 20 μm in potassium hydroxide and patterned using deep reactive ion etching (DRIE) (Figure 4-9(g)). The glass wafers were then immersed in 49% hydrofluoric acid for seven minutes, thereby etching the exposed pyrex isotropically to a depth of 50 μm. A similar method has been employed by Corman et al. [10] for deep wet etching of Borosilicate glass; however, their work used a masking wafer of full thickness that had been etched anisotropically, resulting in less precise pattern definition. We preferred the silicon bonding and etch-back approach over the use of other alternatives for its good adhesion, low undercut, and low processing temperature. The use of metal masks using evaporated or sputtered chromium/gold has also been reported in the literature; however, the edge adhesion of a Cr/Au mask in HF depends on the exact pre-deposition cleaning protocol, residual stress in the metal film, and pin-hole density. LPCVD polysilicon on the other hand
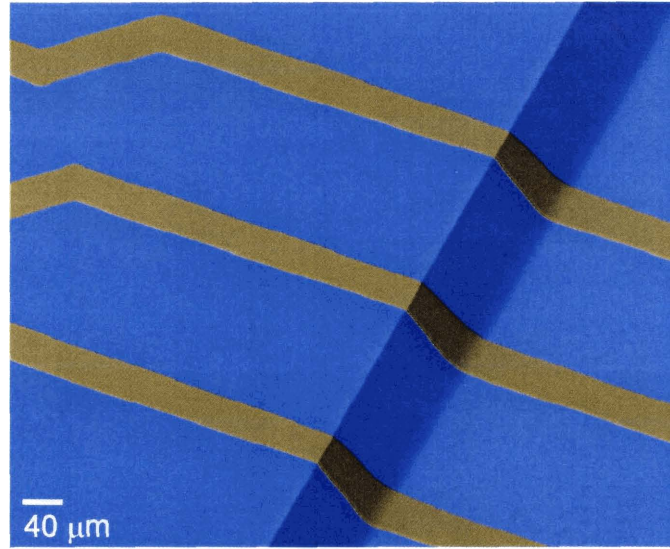
Figure 4-10: Metal traces were patterned inside of 50 μm deep isotropically etched recesses in the glass capping wafer. Good patterning fidelity was obtained for traces that were 50 μm wide and separated by at least 200 μm. The traces constitute electrodes for electrostatic actuation of the resonators.

generally adheres well to pyrex substrates, but the high process temperature often leaves the wafers warped which would have complicated many of the subsequent steps.[5]

After the deep glass etch (Figure 4-9(h)), the masking layer was further reduced by DRIE to leave only a sparse distribution of silicon islands; these formed the hard spacers required by the glass frit bonding process (Figure 4-9(i)) to limit the compression of the frit. Last, a tri-layer stack of chromium, molybdenum and gold was deposited (Figure 4-9(k)) by ion beam deposition. The chromium served as an adhesion layer, and the purpose of the molybdenum was to prevent diffusion of chromium into the gold during the glass frit bonding. The metal film was patterned (Figure 4-9(l)) and exhibited good step coverage over the etched features in the glass, as shown in Figure 4-10.

After the glass frit layer had been deposited by silk-screen printing (Figure 4-9(m)), the device and the capping wafer were bonded under vacuum at 425°C (Fig-

---

[5]We conducted test depositions of LPCVD polysilicon on six inch pyrex wafers and observed deformation by several millimeters even at a deposition temperature as low as 560°C.

63
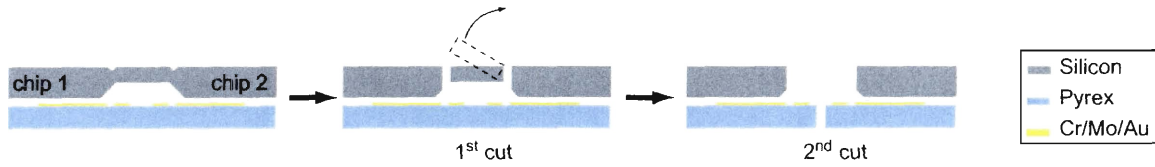
Figure 4-11: The released and bonded device wafer can be die sawed without damaging the resonators. Two cuts into the silicon are made to reveal the bond pads prior to separating the individual chips. The silicon above the bond pads has been recessed by ~300 μm as part of the release etch.

ure 4-9(n)). Once bonded, the wafers could be die sawed without damaging the resonators. The dicing was done in two steps: First, two cuts were made along the streets between columns of dies; these cuts were only deep enough to go through the silicon wafer in order to reveal the bond pads on the glass, as shown in Figure 4-11. The loose silicon between dies was then removed and the full wafer stack was cut to separate the individual chips. At the end of the process, a colloidal silver paste was applied to the narrow gap between the pyrex and the silicon chip, as shown in Figure 4-12. The particles aggregate after evaporation of the solvent and make an electrical connection between the chrome on the silicon chip surface and a large gold pad on the glass lid. This connection makes it possible to contact the resonator surface via a wirebond pad on the glass.

The finished devices had vacuum encapsulated resonators with quality factors up to 700 in the case of 30 kHz cantilever beams (Figure 4-13(a)), and $Q \sim 1400$ for the 600 kHz anti-symmetric mode of the two-paddle torsional resonators (Figure 4-13(b)). Comparing the quality factor of vacuum packaged devices to that of unpackaged devices in a vacuum test chamber reveals that the pressure inside the on-chip cavity is ~1 Torr. Therefore, damping is still limited by viscous drag due to residual gas. Although the wafer bonding was carried out under high vacuum ($P < 1$ mTorr), the large surface area-to-volume ratio of the on-chip cavity causes significant pressure build-up as a result of outgassing. Sub-millitorr vacuum encapsulation in micromachined devices has been achieved by various groups through the use of integrated getters to trap residual gas [59, 64].
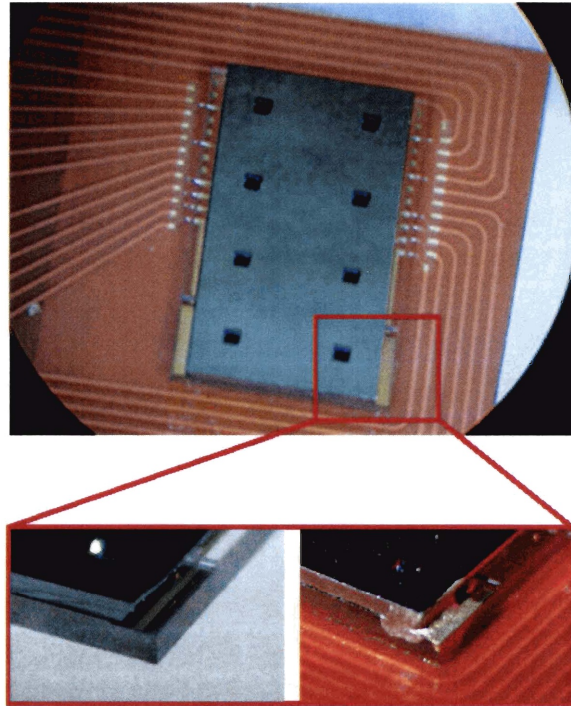
Figure 4-12: At the end of the process, a colloidal silver paste is applied to the narrow gap between the pyrex and the silicon chip. The silver particles make an electrical connection between the chrome on the silicon chip surface and a large gold pad on the glass lid.
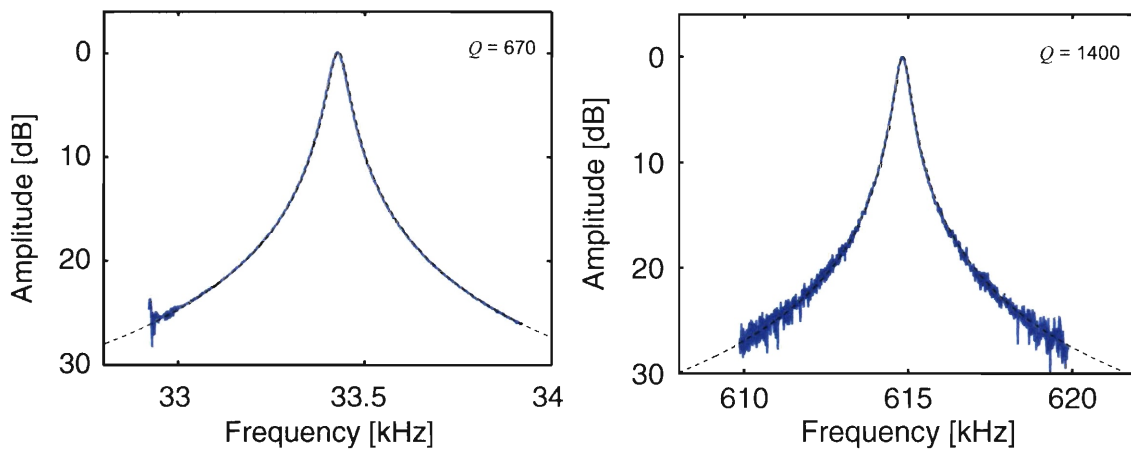
(a) Frequency response of a vacuum packaged cantilever.

(b) Frequency response of a vacuum packaged torsional resonator.

Figure 4-13: Cantilevers packaged by glass frit bonding under vacuum show a quality factor up to ~700 (a), and torsional resonators with higher resonance frequency have a Q of ~1400 (b).

Chapter 5

Measurement instrumentation

5.1 Frequency measurement

5.1.1 Comparison of measurement techniques

The natural frequency of micromechanical resonators may be obtained from observation of the amplitude or phase of the resonator response to an external driving force. When high accuracy or speed are not a concern, it is often convenient to drive the system over a range of frequencies and to determine the centroid of the resulting amplitude spectrum from a non-linear fit. This measurement can be easily performed with an off-the-shelf network analyzer, however the frequency resolution of such instruments is typically limited to a few Hertz at scan times of several seconds, which is not sufficient for most resonant sensor applications. A more precise technique is to measure the phase lag between drive and response at a fixed frequency, as illustrated in Figure 5-1a. The driving frequency may be tuned to be close to the resonance in order to obtain the best sensitivity. Only one frequency reference with high stability is required, and measurement errors are entirely due to phase noise at the output of the resonator. Any function generator with a temperature controlled crystal oscillator as time base is usually sufficient to not introduce additional errors. The main drawback of the fixed-frequency method is its limited dynamic range, which is on the order of the bandwidth of the resonator.
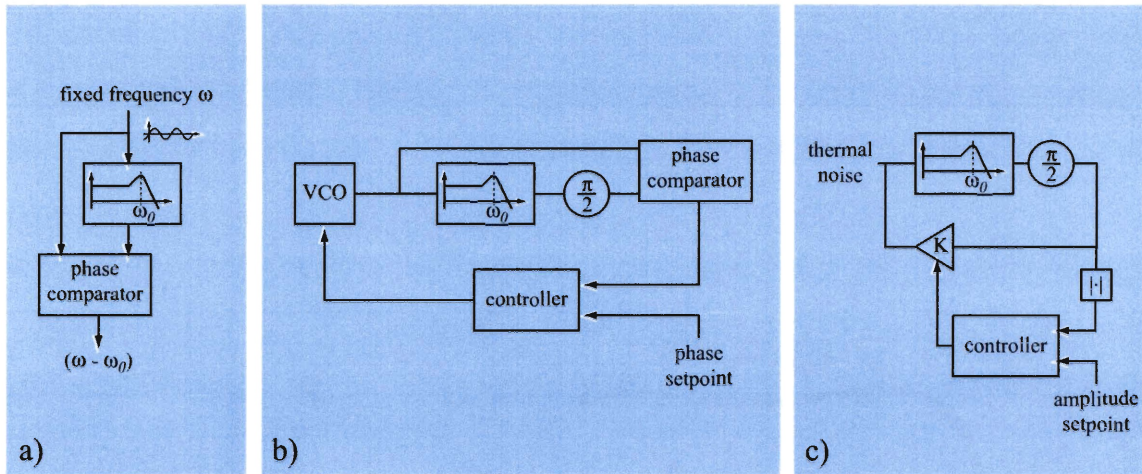
Figure 5-1: Three phase-based methods for measuring the natural frequency (ω_0) of a micromechanical resonator: (I) uses an open-loop measurement of the phase shift between a fixed drive signal and the response to determine ω_0. (II) and (III) are closed-loop tracking circuits. In (II), a voltage controlled oscillator (VCO) maintains a set phase relationship between input and output of the resonator. (III) uses positive feedback to create a free-running oscillator whose frequency matches ω_0.

The dynamic frequency range may be extended by using feedback, as shown in Figure 5-1b. A controller compares the measured phase to a setpoint and adjusts a voltage controlled oscillator (VCO) to maintain a fixed phase difference between input and output of the resonator. If the setpoint is zero and the output signal is phase shifted by ninety degree, as shown in Figure 5-1, the VCO will always track the natural frequency of the resonator. The frequency noise is governed by phase noise due to thermal fluctuations as well as the performance of the voltage controlled oscillator. Analog implementations of the phase-locked-loop approach are often limited by the need for a tunable and highly stable frequency source.

An alternative method to obtain wide dynamic range without the need for a high-stability function generator is depicted in Figure 5-1c. Here the resonator is the frequency determining element of an oscillator circuit that is formed by connecting the phase-shifted and amplified output signal back to the actuator, so that the overall loop gain is greater than one and has zero phase at ω_0. After start-up the loop gain is reduced and a stable oscillation amplitude is maintained by an automatic gain control circuit. The physical limit on resolution with the free-running oscillator is

68

the same as for the other two measurement techniques, since frequency jitter at the output is caused by phase noise blurring the frequency at which the criterion for self-oscillation is met. The next section will give a more detailed explanation of the noise characteristics as well as the influence of the loop parameters on the stability of the feedback oscillator.

5.1.2 Phase and frequency noise in harmonic oscillators

All oscillator systems generally contain a non-linear element to limit the amplitude of oscillation; nonetheless, an analysis based on linear systems theory can provide some important insights. If the amplitude is limited by active control of the feedback gain, as shown in Figure 5-1c, the influence of the gain controller may be neglected for short times, so that the system is effectively linear and is represented by the diagram in Figure 5-2. [69] The resonator has the complex frequency response

$$H(j\omega) = \frac{1}{k}\left[\frac{\omega_0^2}{-\omega^2 + j\omega\frac{\omega_0}{Q} + \omega_0^2}\right] \tag{5.1}$$

and the closed loop system is described by

$$\begin{aligned} T(j\omega) &= \frac{H(j\omega)}{1 - Ke^{j\phi}H(j\omega)} \\ &= \frac{1}{k}\left[\frac{\omega_0^2}{-\omega^2 + j\omega\omega_0\left(\frac{1}{Q} - \frac{K}{k}\frac{\omega_0}{\omega}\sin\phi\right) + \omega_0^2\left(1 - \frac{K}{k}\cos\phi\right)}\right] \end{aligned} \tag{5.2}$$

where the gain parameter K has units of N/m. The feedback phase ϕ is tuned manually to make the total loop phase $\sim 0°$, and K is adjusted by the gain controller to minimize the term $\sim j\omega$, which represents the damping. When $\phi \approx \pi/2$ and with K well adjusted, the closed-loop system behaves like a very high quality resonator whose resonance frequency is equal to ω_0. For $\phi \neq \pi/2$, the term $\sim \cos\phi$ in Equation 5.2 gives rise to a dependence of the center frequency on the gain K. The term $\sim j\omega$ in Equation 5.2 represents the damping, and the effective quality factor can be identified

by

$$Q' = \left(\frac{1}{Q} - \frac{K}{k} \right)^{-1} \tag{5.3}$$

which holds for frequencies $\omega \approx \omega_0$ and $\phi = \pi/2$. The only external input to the system is a random force that causes Brownian motion of the mechanical resonator. Due to the high effective quality factor – Q' is typically on the order of 10^6 to 10^8 – the output is a very pure sine wave of angular frequency ω_0. The output referred noise may be expressed in terms of amplitude and phase modulation:

$$x(t) = \left[A + \delta A(t) \right] e^{j\phi(t)}, \qquad \phi(t) = \omega_0 t + \delta\phi(t) \tag{5.4}$$

where δA and $\delta\phi$ represent amplitude and phase noise, respectively. The instantaneous oscillation frequency is defined as

$$\widehat{\omega_0} = \frac{\partial}{\partial t} \phi(t) \tag{5.5}$$

and its power spectral density (PSD), $S_{\widehat{\omega_0}\widehat{\omega_0}}(\omega)$, is related to the PSD of the phase by

$$S_{\widehat{\omega_0}\widehat{\omega_0}}(\omega) = \omega^2 S_{\phi\phi}(\omega) \quad . \tag{5.6}$$

Analogous to section 2.3.1 it can be shown that amplitude and phase noise contribute equally to the distortion of the signal. The total noise power is equal to the power of x itself, since the 'signal' that is generated by the oscillator is nothing but narrow band noise. The power spectral density of $S_{xx}(\omega)$ is therefore

$$S_{xx}(\omega) = S_{ff} |T(j\omega)|^2 \tag{5.7}$$

where S_{ff} is the white noise force given by Equation 2.16. The phase noise PSD is given by

$$S_{\phi\phi}(\omega) = \frac{\frac{1}{2} S_{xx}(\omega)}{\frac{1}{2\pi} \int_{-\infty}^{\infty} S_{xx}(\omega) d\omega} = \frac{1}{2} \frac{S_{xx}(\omega)}{\langle x_{osc}^2 \rangle} \tag{5.8}$$

70
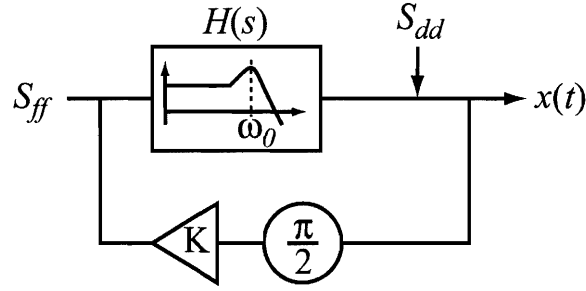
Figure 5-2: Noise in the free-running oscillator is caused by Brownian motion (S_{ff}) and noise in the displacement sensor (S_{dd}).

where $\langle x_{osc}^2 \rangle$ is the mean square amplitude of oscillation. Combining equations 5.8 and 5.6 and integrating over the measurement bandwidth yields

$$\langle (\widehat{\omega_0} - \omega_0)^2 \rangle = \frac{\frac{1}{2\pi} \int_{\omega_0+\omega_1}^{\omega_0+\omega_2} (\omega - \omega_0)^2 S_{ff} |T(j\omega)|^2 d\omega}{\langle x_{osc}^2 \rangle} \quad . \tag{5.9}$$

A simple analytical expression for the noise results if the measurement bandwidth is restricted to an interval $[\omega_1, \omega_2]$ such that $\omega_1 \gg \omega_0/Q'$ and $\omega_2 \ll \omega_0$. The first condition requires that the measurement interval is shorter than the inverse of the oscillator linewidth, which is usually in the range of a few millihertz. To fulfill the second condition frequency measurements need to be taken at a rate much slower than the oscillation frequency itself. The approximation $|T(j\omega)|^2 \approx \frac{\omega_0^2}{4k^2}(\omega_0 - \omega)^{-2}$ then leads to the result

$$\text{Thermal noise:} \quad \left(\frac{\delta\omega}{\omega_0} \right)_{th} = \sqrt{\frac{(\omega_2 - \omega_1) \cdot k_B T}{2\pi\omega_0 k Q \langle x_{osc}^2 \rangle}} \tag{5.10}$$

where $S_{ff} = (4k_B T k)/(Q\omega_0)$ (equation 2.16) has been inserted. Equation 5.10 is an upper bound on the noise level, over-estimating the true value by more the closer the measurement band extends toward low frequencies. Equation 5.10 confirms that the physical noise limit for the oscillator is the same as that in equation 2.21 with $\langle x_{osc}^2 \rangle = Q \cdot F_0/k$ and $(\omega_2 - \omega_1) = 2\pi/\tau$.

Brownian motion accounts only for part of the frequency noise in resonant transducers. Depending on the implementation, the displacement sensor also contributes

significantly to the error. Displacement sensor noise may be described in terms of the corresponding output referred phase noise density, which can then be converted to frequency noise using equation 5.6. To calculate the phase noise at the output we assume that the gain K has been adjusted so that the effective quality factor Q' is very high, and the oscillation amplitude $\langle x_{osc}^2 \rangle$ remains constant over a large number of cycles. The power spectrum of the output signal $x(t)$ is then given by the spectra of the two white noise sources S_{ff} and S_{dd} filtered by their respective closed-loop transfer functions. S_{ff} represents the force noise responsible for Brownian motion, and S_{dd} is the PSD of the displacement sensor noise. The frequency response for S_{dd} is

$$|T(j\omega)|^2 = \left| \frac{1}{1 - jKH(j\omega)} \right|^2 \approx 1 + \frac{\omega_0^2}{4Q^2(\omega_0 - \omega)^2} \quad . \tag{5.11}$$

The frequency noise due to the displacement sensor is now given by

$$\text{Detector noise:} \quad \left(\frac{\delta\omega}{\omega_0} \right)_d = \sqrt{ \frac{S_{dd}}{2\pi \langle x_{osc}^2 \rangle} \left[\frac{1}{3} \frac{\omega_2^3 - \omega_1^3}{\omega_0^2} + \frac{\omega_2 - \omega_1}{4Q^2} \right] } \quad . \tag{5.12}$$

In most cases the first term in the sum will be negligible so that the detector noise is attenuated linearly with Q.

5.1.3 Implementation

The measurement of resonance frequency is based on measuring the resonator vibration in an oscillator circuit. Figure 5-3 illustrates the measurement setup. The frequency is derived from the displacement signal by means of a digital counter. The same signal is also phase shifted, amplified, and connected back to the biased drive electrode; this completes the oscillator configuration described in section 5.1.1. The phase shifter was implemented by a first-order all-pass filter adjusted to provide $\phi = \pi/2$ at the resonance frequency. The amplifier gain was set by the output of a PID-controller operating on the difference between the rms oscillation amplitude and a manually adjusted setpoint signal.

In order to obtain the most accurate measurement of the resonance frequency, it
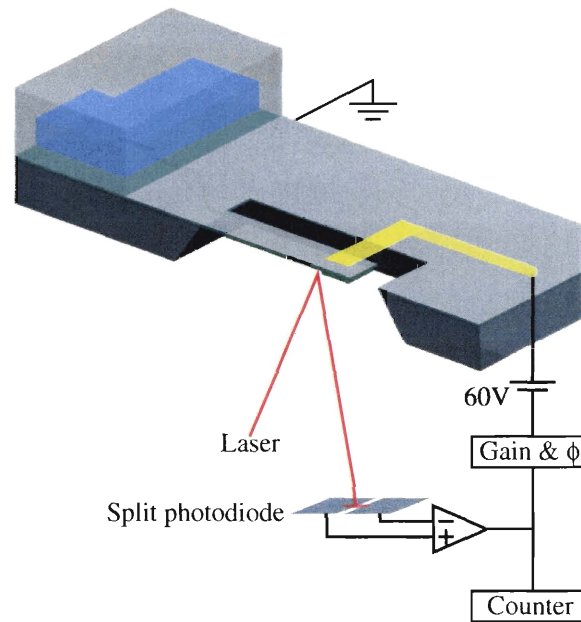
Figure 5-3: The vibration of the resonator is measured by the optical lever method. The optical deflection signal is applied to the drive electrode to form an oscillator circuit, and a digital counter measures the oscillation frequency.

is important for the displacement sensor to have very low noise. One of the simplest techniques to measure the out-of-plane deflection of micromechanical devices with high precision is the optical lever method, which is widely employed in atomic force microscopes. A laser beam is focused onto a spot on the device that experiences a large angular deflection. In the case of a cantilever, for example, this would be near the tip, while a double clamped bridge yields the highest signal to noise ratio when measured between the center and the support. The angle of reflection is measured by a split photodiode, which is used as a position sensitive detector. Note that although Figure 5-3 shows the laser coming from the bottom side of the silicon chip, it can be positioned on either side and the actual measurement configuration was implemented with the optics above the resonator.

The optical lever setup for resonance frequency measurements was laid out as shown in Figure 5-4. The focused beam is perpendicular to surface of the device, and it is narrow enough to not get obstructed by the excitation electrode. Two resonators on a single chip can be measured simultaneously through two independently positioned
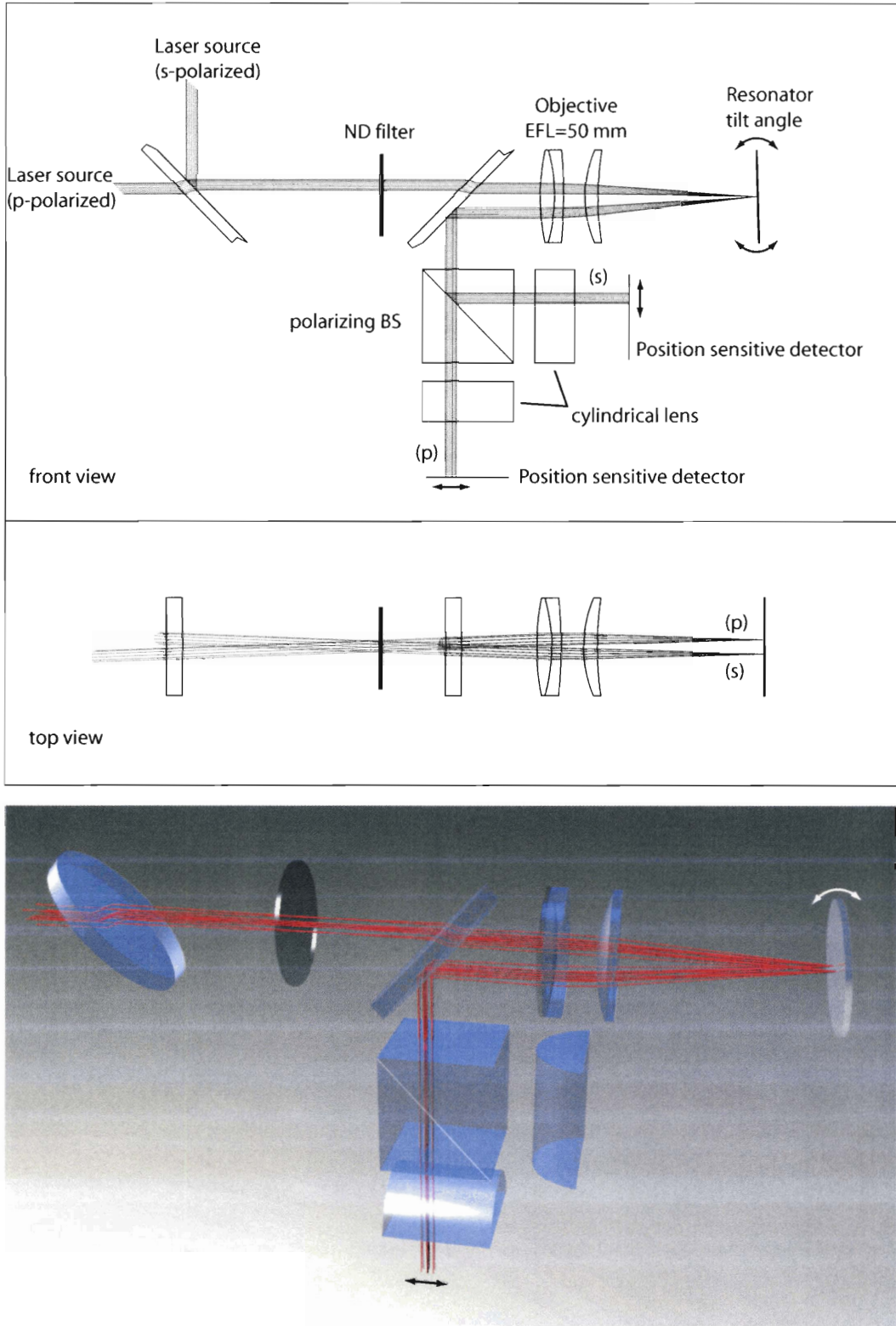
Figure 5-4: Ray diagram of the dual-beam optical lever system. The vibration of two resonators is detected with two independently positioned, orthogonally polarized laser beams.

and orthogonally polarized beams. The light source is a single low-noise laser diode module (Coherent ULN, 635 nm CW, 5 mW) whose output is split by a polarizing cube beamsplitter into the s- and the p-polarized components. Each of the two beams is deflected via an adjustable mirror before the two are re-combined to a common path by a polarization insensitive plate beamsplitter. Next, a neutral density (ND) filter attenuates the light to $\sim$100 μW for each polarization, and the intensity drops by another 50% after the second plate beamsplitter in Figure 5-4. The purpose of attenuating the laser intensity is to prevent excessive heating of the resonator; a 300 μm cantilever with chromium metallization will warm up by $\sim$3°C when a 50 μW laser spot is focused onto its tip.

The objective lens is a combination of an achromatic doublet and a positive meniscus lens with a total effective focal length (EFL) of 50 mm. This lens combination has diffraction limited performance even for oblique rays. After reflecting off the surface of the micromechanical resonator, the beam is re-collimated by the objective at a different position, and the lateral shift is proportional to the effective focal length and the angle of reflection. While the deflection sensitivity of the system increases with increasing focal length, the spot size at the focal plane also increases proportionally.

The beamsplitter now separates the path of the incident and the reflected rays, and the latter are directed towards the split photodetector via a cylindrical lens. Focusing the light in the direction perpendicular to the expected movement eliminates the need for detector alignment along this axis. A polarizing cube beamsplitter transmits the p-polarized beam towards the detector for one resonator, while the s-polarized beam is reflected at 90° towards the detector for the other resonator.

When properly aligned, the channel separation after the detection beamsplitter exceeds 60 dB.[1] In addition, the initial resonance frequencies of the two devices on a chip typically differ by $\sim$3%, which is more than the width of the resonance peaks. Therefore, channel cross-talk when measuring frequency is zero for all practical purposes and the signal of one sensor does not noticeably degrade the resolution of the other.

---

[1] Manufacturer specification for the polarization purity.
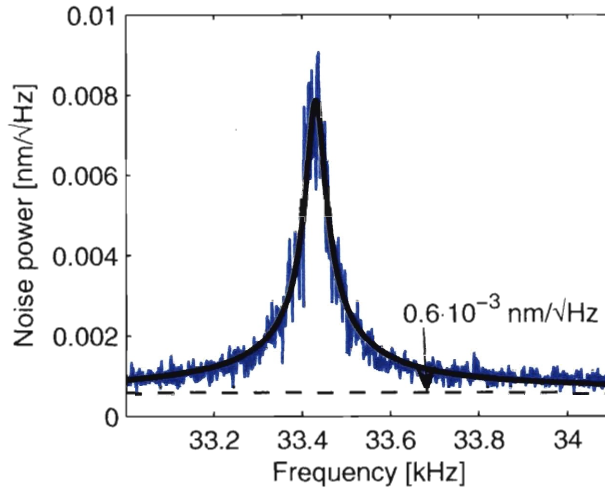
Figure 5-5: Sensitivity and noise floor of the optical lever setup are determined from the noise spectrum of an undriven cantilever. The dashed line represents the equivalent deflection noise of the detector. Q=700.

The deflection sensitivity not only depends on the geometry of the optical lever setup, but also on the intensity of the reflection and the alignment of the detector. If the spring constant of the resonator is small and its value known, the Brownian motion may be exploited to calibrate the detector: the thermal fluctuation $\langle x^2 \rangle$ is given by the equipartition theorem (Eq. 2.14) on one hand, and it may also be calculated from the noise measured at the detector output. Comparing the two calculations yields the scaling (in units of nm/V) that relates the PSD amplifier output to the displacement. Figure 5-5 shows the power spectral density (PSD) of the deflection signal for a cantilever ($Q \sim 700$) with the electrostatic drive turned off. The PSD has been fitted with the transfer function of a second order harmonic oscillator, and the dashed line represents the offset obtained from the fit. The offset represents the noise contribution due to the detector. The y-axis has been calibrated so that the area under the fit without the offset matches the magnitude of the thermal vibration predicted by the equipartition theorem. The noise spectrum in Figure 5-5 and equations 5.10 and 5.12 reveal that Brownian motion is limiting the frequency resolution. When operated at 500 nm rms oscillation amplitude, equation 5.10 predicts a maximum frequency resolution of 0.08 ppm for this resonator (k~1 N/m, bandwidth=10 Hz).

76
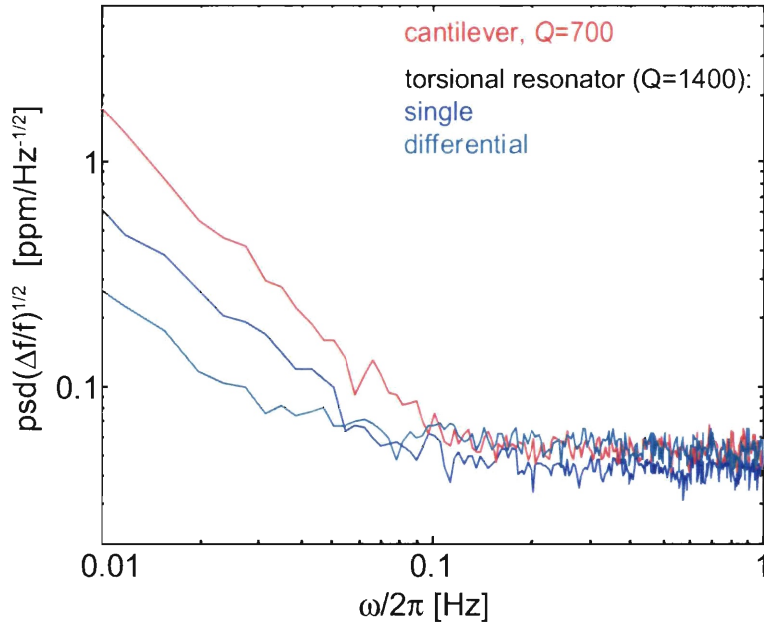
Figure 5-6: The power spectral density of frequency noise is white for measurement time scales shorter than ∼10 s. The measurement error at low frequencies is dominated by drift.

The power spectral density of frequency noise plotted in figure 5-6 reveals that there are two domains with distinct noise characteristics: At frequencies that are 0.1 Hz or more from the carrier, i.e. the measurement time scale is no longer than 10 s, the noise spectrum is white and conforms with equations 5.12 and 5.10, although the absolute magnitude is approximately five times larger than the theory. Error sources that were not taken into account in the estimation are the measurement and triggering error of the frequency counter, noise introduced by the amplifier and phase shifter, and performance degradation due to the limited accuracy of phase adjustment in the feedback network.

At frequencies below 0.1 Hz, the measurement accuracy is limited by drift, which is best characterized in the time domain. The systematic nature of long-term instability prevents its reduction by narrowing the measurement bandwidth. At the same time, drift of non-random origin such as, for example, temperature fluctuations, may be suppressed by conducting a differential measurement, as shown in Figure 5-7. To attain the best common mode rejection, the reference signal $f_{ref}(t)$ is offset and

77

scaled to most closely approximate the sense signal, $f_{sense}(t)$:

$$f_{sense}(t) = a + b \cdot f_{ref}(t) + \eta(t) \tag{5.13}$$

The coefficients a and b are determined by linear least squares regression, and $\eta(t)$ is the residual error. If systematic errors are cancelled completely, the histogram of η has a Gaussian distribution. Figure 5-7 represents a typical differential measurement in which one resonator was filled with liquid. The frequency over time was referenced to and scaled by the first datapoint in each trace. A small offset was artificially added in order to separate overlapping traces on the plot. The difference signal represents the residual noise, $\eta(t)$, in Equation 5.13. The residual noise after subtraction of the reference from the sense signal has a Gaussian distribution, indicating that systematic errors have been significantly reduced. The standard deviation of the residual noise represents the long term frequency stability. Values on the order of 0.1 ppm over one hour have been measured with dry resonators, and $\sim$0.5 ppm was observed in continuous flow. The noise with flow is higher in part because of numerous small frequency jumps which were not observed with the same device when it was dry. Understanding the origin of these jumps requires further investigation.

5.1.4 Cantilever heating

Heating is a potential concern with displacement sensing by the optical lever method. The high aspect ratio of the suspended channel results in good thermal insulation from the substrate, and even low levels of heat generation can give rise to excessive temperatures. The approximate temperature rise due to illumination by the readout laser may be calculated from the laser power and the thermal conductivity of the cantilever. The beam is modeled as a one dimensional slab that is heated on the free end and held at constant temperature where it is attached to the substrate. At steady state, the temperature profile is linear and the temperature rise at the free end is given by

$$\Delta T = P \frac{L}{K} \tag{5.14}$$
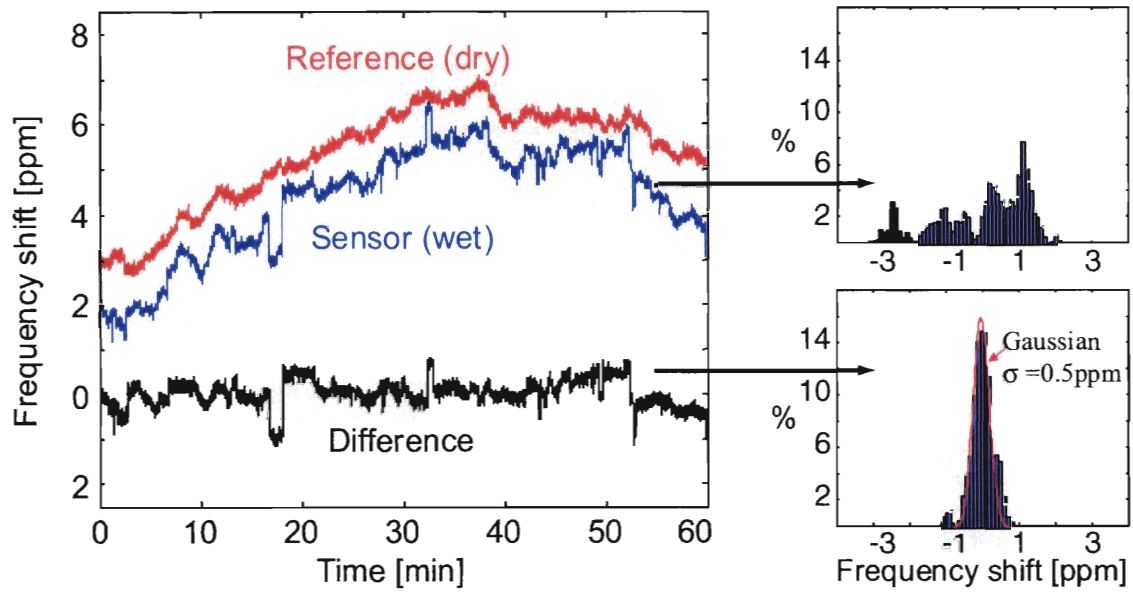
Figure 5-7: Drift may be suppressed by conducting a differential measurement. The residual noise after subtraction of the reference from the sense signal has a Gaussian distribution, indicating that systematic errors are significantly reduced.

where L is the length of the beam and P is the heating power applied to the tip. K^{-1} denotes the thermal resistance per unit length. For the hollow cantilevers considered here, K is dominated by heat conduction through the channel wall, and for the cantilevers of type III in Figure 3-1 with $\kappa_{\text{Nitride}}=15\text{--}30\ \frac{\text{W}}{\text{m}\cdot\text{K}}$ K takes a value of 1.6–3.1 $\frac{\text{W}\cdot\text{m}}{\text{K}}$. Therefore, the temperature rise at $L{=}300\ \mu\text{m}$ is $\sim190{\cdot}10^3$ K/W. This is a worst-case estimate that neglects cooling due to fluid flow inside the cantilever. Convective heat transport alters the temperature profile along the suspended channel, however the temperature distribution throughout the cross-section is approximately uniform even at a high flow rate. Temperature spreads through the thickness of the fluid layer with the time constant

$$\tau_d = d^2\,\frac{\rho C_p}{\kappa} \tag{5.15}$$

where κ, ρ, and C_p are the heat conduction coefficient, the density, and the heat capacity of water. For a channel thickness $d{=}1\ \mu\text{m}$, Equation 5.15 yields $\tau_d \approx 7\ \mu\text{s}$, corresponding to a distance of ~350 nm at a flow of 1 nL/s. Since this distance is

short compared with the extents of the device, the fluid can be regarded as being in thermal equilibrium with the device walls.

The heating power depends on the intensity of the readout laser as well as the optical properties of the reflective layer. Devices that were fabricated using the glass frit process are coated with 50 nm chromium. The film is almost completely opaque as the thickness is much greater than the skin depth, however the reflection coefficient of chromium at λ=635 nm is only ~50% [40]. In order to minimize the effect of laser heating, the beam has been attenuated to 50 μW in all measurements, yielding a worst-case temperature rise of ~3–5°C while still enabling adequate deflection sensitivity. It is interesting to note that if gold or aluminum is used as the reflective material, the absorption coefficient is only ~8% and an approximately six times higher light intensity can be used, thereby increasing the signal-to-noise ratio of the detector.

5.2   Fluid delivery and interconnects

The wafer-level packaged chips already contain a microfluidic network that enables the quick exchange of samples inside the thin resonator channel. Fluids are injected into the chip from the backside via anisotropically etched through holes. The fluidic connections need to satisfy several stringent requirements: they need to be compatible with acids and bases required for cleaning, as well as a range of organic solvents that are used to functionalize the sensor. Furthermore, the connections have to be leak tight up to ~100 psi, and they should be suitable for high density integration. Figure 5-9(a) illustrates our package design. The devices are attached to an adhesive backed, gold plated printed circuit board (PCB) and wirebonded directly to the board, as shown in Figure 5-8. The assembly is clamped onto a Teflon (PTFE) manifold holding an array of standard 1/32" (0.794 mm) outer diameter Teflon FEP tubes. The holes in the manifold were initially drilled at a smaller nominal diameter (0.711 mm), and the manifold was heated for insertion of the tubes. After cooling to room temperature a leak tight seal was obtained between the through holes in the hard
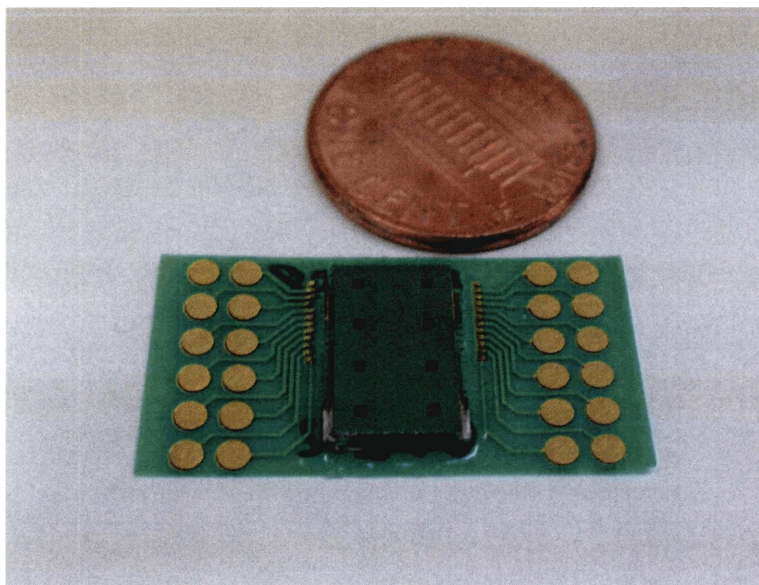
Figure 5-8: Sensor chips are attached to an adhesive backed, gold plated thin core PCB and wirebonded directly to the board. The assembly is seen from the backside, revealing the eight fluid inlets and the wirebonds from the glass lid to the PCB.

PTFE block and the relatively flexible FEP tubing. Finally, the manifold is sealed against the chip surface with commercially available perfluoroelastomer (SIMRIZ™) O-rings, the size of which limits the practical interconnect density to a 3×3 mm grid. Our design enables the reversible connection to multiple fluid inlets on a tight space with chemically inert materials. The fluidic seal is reliable and leakage free for pressures up to 150 psi.[2]

Since the flow resistance of 1 μm tall microfluidic channels is extremely high, a low resistance bypass is required to quickly exchange samples inside the resonator. Without the bypass, any fluid contained in the tubes and connections before the sensor chip would need to be displaced through the resonator at flow rates of less than 1 nL/s every time a new sample is loaded.

The microfluidic network shown in Figure 5-10 illustrates the distribution of fluid on the sensor chip. The inlet and outlet of the resonator connect to channels that are etched 50 μm deep into the cover glass; these channels themselves each possess

---

[2]Leak tests were performed by mounting a test chip with no holes on the chuck and submersing the assembly in a water bath. Leaking connections could be identified by bubble formation upon application of pressure to the tubes.
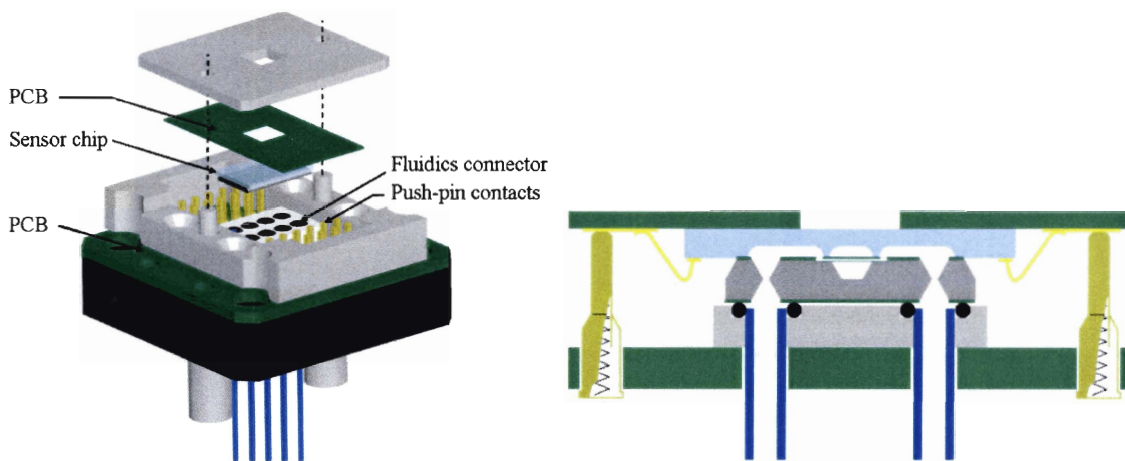
(a) Exploded view of the sensor mount.

(b) Cross-section of the mount showing the electronic and fluidic interface.

Figure 5-9: The sensor chip is clamped onto a Teflon manifold holding an array of standard 1/32" OD Teflon tubes. Perfluoroelastomer O-rings form a seal between the manifold and the chip, and an array of spring loaded contacts provides electrical connections to the PCB.

one inlet and one outlet formed by through-holes in the silicon chip. Therefore each device has four fluid connections per resonator.

An Agilent 1100 HPLC system delivered a continuous flow of buffer at a rate of 5 μL/min.[3] The HPLC pump contains an active flow splitter that maintains the desired flow rate independent of the applied backpressure. Flow inside the resonator was controlled by regulating the pressure difference between the inlet and the outlet bypass. The inlet pressure was elevated either by increasing the flow resistance between the chip and the waste reservoir, or by pressurizing the waste bottle with compressed nitrogen.

---

[3]Typical value. Flow rates in the range of 1–10 μL/min were used in some experiments.
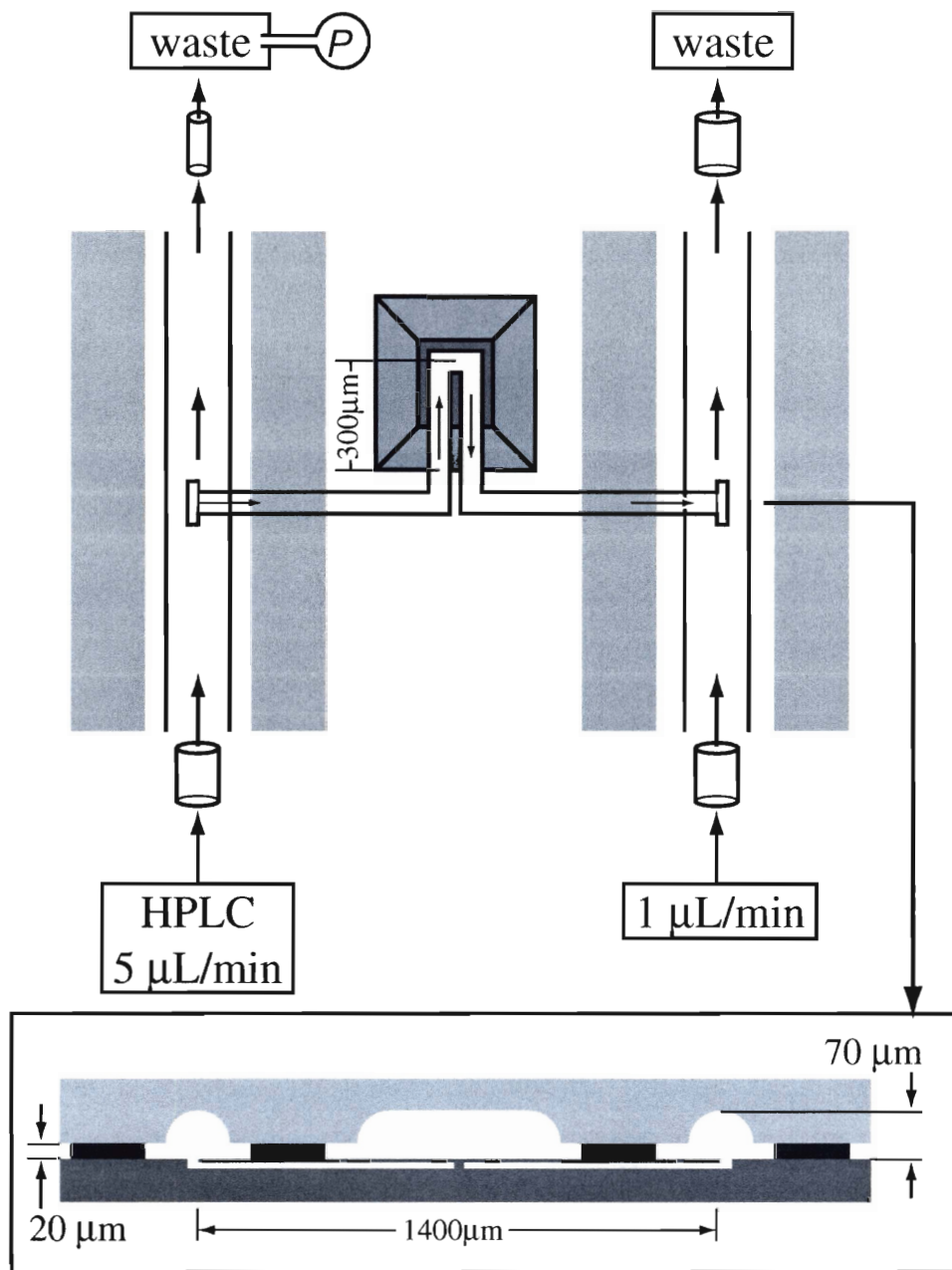
Figure 5-10: Microfluidic bypasses enable the quick exchange of samples inside the suspended microchannel. The flow rate through the resonator is controlled by the pressure difference between the inlet and the outlet bypass.

Chapter 6

Device characterization

6.1 Quality factor

A high quality factor enables high frequency resolution and is therefore a prerequisite for sensing small mass changes with a resonant transducer. In addition to reducing thermal noise ($\propto Q^{-1/2}$), a high Q-value also helps to reject electronic noise ($\propto Q^{-1}$), thereby simplifying the design of the readout circuit.

The quality factor of a second order system is defined via the ratio of stored energy to energy that is dissipated during one cycle at resonance. Most of the following discussion relates directly to the quality factor, however sometimes it will be helpful to consider the relationship between Q and the linear damping coefficient c in the lumped parameter model

$$m^* \ddot{u} + c\dot{u} + ku = F \quad . \tag{6.1}$$

All parameters pertain to a particular mode of vibration and are obtained by modal decomposition of the three-dimensional solution to the vibration equation. $u(t)$ is the amplitude of the mode being considered, m^* is the effective mass, k is the spring constant, and F is the driving force. The quality factor is related to the damping coefficient by

$$Q = \frac{1}{c}\frac{k}{\omega_0} \quad . \tag{6.2}$$

The quality factor of micromechanical resonators is limited by several mechanisms:

Energy loss to the surrounding medium is usually most significant, followed by internal friction and clamping loss at the support [79]. The total damping coefficient and Q-factor may be written as

$$
\begin{aligned}
c &= c_{\text{internal}} + c_{\text{support}} + c_{\text{squeeze film}} + c_{\text{air}} + c_{\text{fluid}} \cdots \\
\frac{1}{Q} &= \frac{1}{Q_{\text{internal}}} + \frac{1}{Q_{\text{support}}} + \frac{1}{Q_{\text{squeeze film}}} + \frac{1}{Q_{\text{air}}} + \frac{1}{Q_{\text{fluid}}} \cdots
\end{aligned}
\tag{6.3}
$$

Hosaka et al. [24] have shown that the quality factor associated with clamping losses of cantilever beams is given by $Q_{\text{support}} \approx 2.17 L^3/W^3$. For all cantilever resonators considered here, this value exceeds $4 \cdot 10^5$, which is much larger than any of the measured Q values. Support losses are therefore insignificant in our silicon nitride devices.

Resonators made out of amorphous materials suffer from large internal friction compared to single-crystal silicon devices, and very thin (sub-micron) beams experience additional damping due to surface loss mechanisms. The predominant internal loss mechanism in thick (several micrometer) cantilevers oscillating at several hundred kilohertz is thermoelastic dissipation caused by irreversible heat flux between the side of the beam that undergoes compression and the side that undergoes tension. [79] Given the geometry and low resonance frequency of our cantilever sensors, bulk friction is likely to place the ultimate limit on the internal quality factor at low ambient pressure. Oscillation of a fluid filled cantilever is subject to additional damping due to the fluid viscosity and irreversible mass transport. Depending on the properties of the fluid, the corresponding quality factor may limit the device performance, and this limitation will be discussed in more detail later in this section.

Operation of the resonator in vacuum is required if internal damping effects are to be measured. Damping due to the medium surrounding an oscillating cantilever depends strongly on the geometry of the device as well as on the arrangement of surfaces around it. When the resonator is in close proximity to a surface, the dominant damping term is due to squeeze film damping. The magnitude of this effect at high ($\sim$1 atm) pressure and for beams that are much longer than wide ($L \gg W$) can be

determined by solving the governing Reynolds equation, leading to the formula [24]:

$$Q_{\text{squeeze film}} = \frac{\omega_0 m_A}{\eta} \left(\frac{g}{W}\right)^3 \qquad (6.4)$$

The parameter m_A is the cross section mass of the beam, g is the gap size, and η is the viscosity of air ($1.86 \cdot 10^{-5}$ Pa s). At atmospheric pressure, the glass packaged cantilevers that were fabricated in this work have values $Q_{\text{squeeze film}}$ of 1500 (design II) and 5300 (design III). In addition to squeeze film damping, airflow induced drag lowers the quality factor of micromechanical resonators. Viscous damping in air and fluids has been modeled analytically by Sader [53], who found that the quality factor of rectangular cantilevers in viscous media can be approximated by

$$Q_{\text{fluid}} = \frac{k}{0.1906 \, \rho \, W^2 \, L \, \Gamma_i(\text{Re}) \, \omega_0^2} \qquad . \qquad (6.5)$$

The cantilever parameters that enter the equation are the spring constant k, the width and length, W and L, and the natural frequency ω_0; the fluid density is ρ, and $\Gamma_i(\text{Re})$ is the imaginary part of the hydrodynamic function, whose explicit form is given in [52]. Γ_i is a function of the Reynolds number $\text{Re} = \rho \omega_0 W^2/(4\eta)$. Equation 6.5 may also be inverted to obtain the spring constant if the quality factor and resonance frequency has been measured, which is a convenient method to calibrate the stiffness of rectangular micro-cantilevers if the thickness and material parameters are unknown [53].[1]

For 63 μm wide hollow cantilever (type III in Figure 3-1) with k=1 N/m obtained by finite element analysis and ω_0=35 kHz (measured), equation 6.5 predicts Q=88.6, which is in excellent agreement with the measured value of 89.

The Sader model is only applicable to viscous media, such as liquids or gases at atmospheric pressure. In vacuum, the mean free path length of gas molecules is generally greater than the dimensions of the device, and treatment of the gas as a continuum is inaccurate. The deviation from the continuum model can be accounted

---

[1]For quick estimations, the hydrodynamic function can be approximated in the range $0.01 < \text{Re} < 100$ by $\Gamma_i(\text{Re}) \approx (\text{Re}/10)^{-2/3}$ with a maximum deviation of 30% from the exact value (15% for $0.1 < \text{Re} < 10$).

for by replacing the absolute viscosity by an effective viscosity which depends on pressure as

$$\eta_p = \frac{1}{1 + \frac{p_{1/2}}{p}} \qquad (6.6)$$

where $p_{1/2}$ is an empirically determined parameter that depends on the geometry. [46, 38] A physical interpretation of $p_{1/2}$ is that this is the pressure at which the mean free path length is comparable to the relevant length scale for air damping of the resonator. Using equation 6.6 and assuming a linear dependence of squeeze film and air flow damping on viscosity, the quality factor at low pressure may be modeled by

$$\frac{1}{Q(p)} = \frac{1}{Q_{\text{internal}}} + \frac{1}{Q_{\text{fluid}}} + \frac{1}{Q_{\text{air}}} \frac{1}{1 + \frac{p_{1/2}}{p}} \qquad . \qquad (6.7)$$

Q_{fluid} characterizes damping due to fluid contained inside the hollow resonator and can be disregarded when the device is empty. Indeed, the effect of low viscosity fluids like water or organic solvents is not detectable at atmospheric pressure, as can be seen from the frequency response curves and measured Q factors shown in Figure 6-1. When the resonator is filled with isopropanol or water, the resonance frequency decreases as expected while the quality factor exhibits a slight increase from 88 to 94. The increase in Q of ~6% is consistent with the reduction in resonance frequency, since the quality factor of a damped harmonic oscillator with fixed spring constant and fixed damping coefficient is inversely proportional to the resonance frequency (c.f. Equation 6.2).

The damping induced by the liquid inside a hollow cantilever beam was investigated experimentally. Measurements at low ambient pressure were conducted using a single-beam version of the optical system described in section 5.1.3 placed inside a vacuum chamber. Figure 6-2 shows the design of the setup. The laser is coupled to a single mode fiber which enters the chamber through one of the vacuum ports. The tubes were inserted through holes that had been drilled with a 0.029" (0.737 mm) drill bit in a 1/4" teflon cylinder, which was subsequently connected to the vacuum chamber with a 1/4" Swagelok adapter. For the optical fiber, a 150 μm drill bit was used to make the hole in the teflon. When the teflon cylinder was compressed by
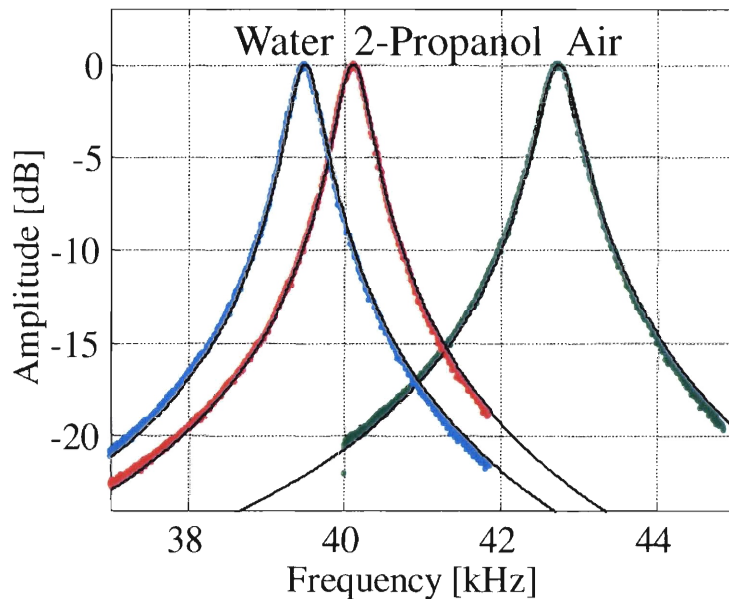
Figure 6-1: When measured in air, the quality factor of a fluid filled cantilever shows no degradation compared to an empty device (green trace). Measurements were taken with a device of type I (c.f. Figure 3-1) driven by an external electrode to avoid excessive squeeze film damping. The quality factors and center frequencies obtained by fitting the frequency response of a harmonic oscillator are (from right to left): Q=88, 94, 94, and f_0=42.7, 40.1, 39.5 kHz.

the Swagelok ferrule, the fluidic and optical feedthroughs formed an air tight seal. The performance of the mechanical pump limited the attainable vacuum level to $\sim$30 mTorr ($\sim$4 Pa). The vacuum level was measured using an HPS 325 Moducell Pirani transducer from MKS Instruments Inc. (Boulder, CO).

The quality factor of a 63 μm wide and 300 μm long cantilever containing a 1 μm thin fluid channel (design III in Figure 3-1) was measured at low pressure while the device was filled with air, water, and silicone fluid viscosity standards of 10 mPa s and 50 mPa s. Viscosity standards were purchased from Brookfield (Middleboro, MA). In all experiments, the cantilever was first rinsed with acetone followed by ethanol in order to remove any residues. The microfluidic channels were then purged with nitrogen (grade 5.0) at 100 psi for at least ten minutes to evaporate the solvent while the channel exterior was pumped to the base pressure of 30 mTorr. Connecting or disconnecting the pressurized gas had no detectable effect on the measured vacuum level, which indicates that all O-ring connections to the chip were well sealed. Each
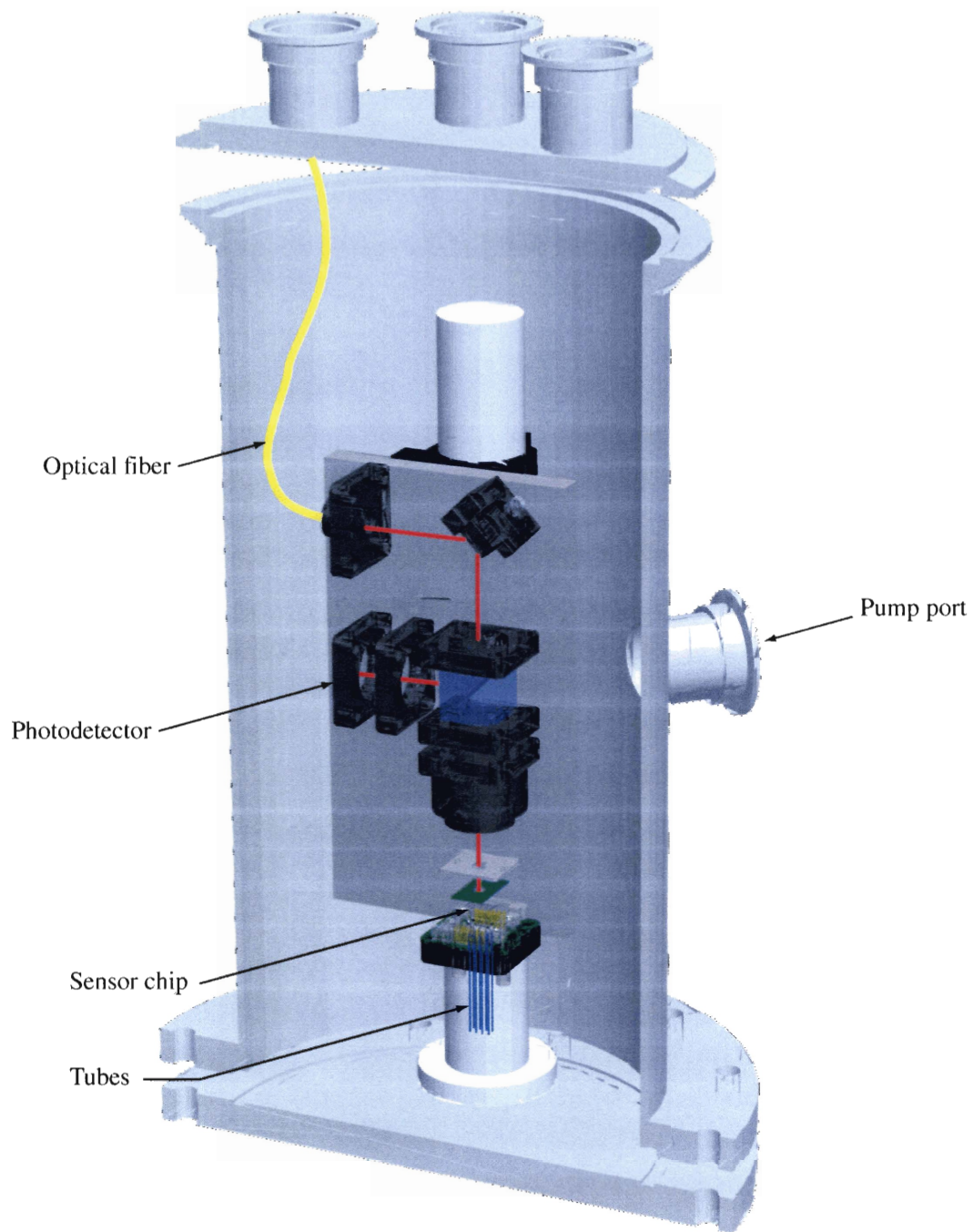
Figure 6-2: A vacuum chamber with fluidic feedthroughs was used to measure the quality factor of fluid filled cantilevers at a pressure of 30 mTorr.
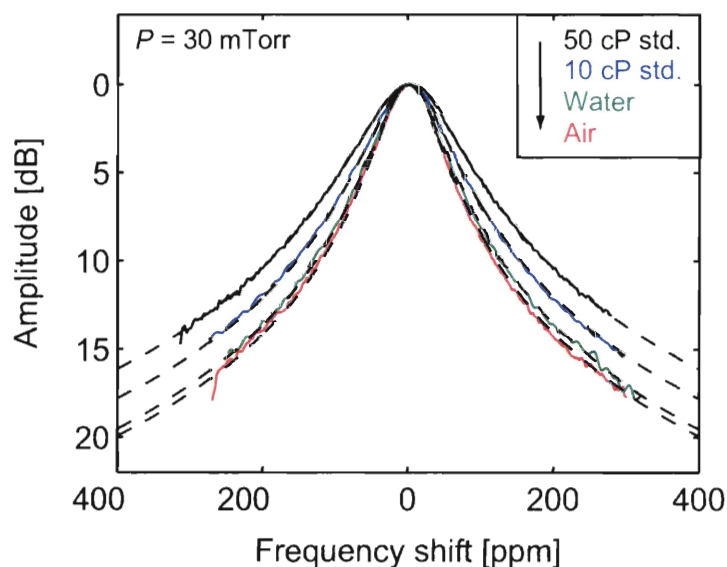
Figure 6-3: The frequency response of a water filled cantilever at 30 mTorr is almost indistinguishable from that of a dry device. For a fluid viscosity of 10 and 50 mPa s, damping visibly lowers the quality factor. Frequency response plots are shown normalized to the center frequency and peak amplitude. The corresponding resonance frequencies and Q-factors are listed in table 6.1

time the device was dried, resonance frequency and quality factor returned to the values for an air filled cantilever surrounded by vacuum. Once dried, the resonator was filled with the sample fluid, and complete wetting of the suspended channel was verified by monitoring the shift in resonance frequency. The frequency response was recorded with an HP4395A network analyzer at a pressure of ~30 mTorr. Finally, the quality factor was monitored continuously while the chamber was slowly vented; Q was calculated as the -3 dB bandwidth divided by the center frequency.

Resonance frequencies and measured Q values obtained by fitting the amplitude response at 30 mTorr are listed in Table 6.1 along with the relevant properties of the different media at room temperature and at atmospheric pressure.[2] Although the quality factor degrades when the channel is filled with water, the value of 11,580 is still close to that of the empty device (Q(dry)=12,520). In all cases, the resonance

---

[2]Data for air and water was taken from the *CRC Handbook of Chemistry and Physics, 85th Ed.* [40], and the specifications for the viscosity standards were provided by the manufacturer. The values are valid at 25°C.

Table 6.1: Measured resonance frequency and quality factor of a cantilever filled with different media and operated at 28±2 mTorr (4 Pa) ambient pressure.

Filling medium	Density [g/cm^3]	Viscosity [mPa·s]	Resonance frequency [kHz]	Q	Q_{fluid}
air	1.18·10^{-3}	0.019	35.179	12,520	∞
water	0.997	0.888	33.666	11,580	100,820
10 cP standard	0.940	9.8	33.752	9,781	39,050
50 cP standard	0.960	46	33.717	7,855	19,700

spectrum could be described well by the frequency response of a harmonic oscillator, as illustrated by the fits in Figure 6.1 that were used to extract ω_0 and Q.

By comparing the quality factors for different media it is possible to isolate the contribution of the fluid to the damping of the beam. Filling the resonator with fluid increases the damping coefficient to

$$c = c_0 + c_{fluid} \tag{6.8}$$

where c_0 includes the effects of internal damping and air damping. Starting from the measured quality factor of a dry device, $Q(\text{dry})$, the quality factor associated with fluid damping for water (and other media) may be deduced:

$$\frac{1}{Q_{\text{fluid}}(\text{water})} = \frac{1}{Q(\text{water})} - \frac{\omega_0(\text{water})}{\omega_0(\text{dry})} \frac{1}{Q(\text{dry})} \tag{6.9}$$

The values of Q_{fluid} for the different media are listed in Table 6.1. In the case of water we find $Q=$11,580 at 30 mTorr, and the calculated fluid limited quality factor Q_{fluid} is greater than 100,000. This is an important result, since it shows that the ultimate frequency resolution is not significantly degraded by the presence of the fluid. Sparks et al. have previously reported that the Q-factor of a fluid filled resonator of $\sim 100 \times 100 \mu$m cross section can exceed 20,000 in high vacuum. [63]. Our measurement proves for the first time that very thin vibrating tube resonators with a large ratio of surface area to mass can have a similar quality factor, thereby uniting high surface mass sensitivity and good frequency resolution in liquid.

Cantilever resonators that were packaged by glass frit bonding had a quality factor of 300–700, and the Q for torsional resonators was $\sim$1400. Our measurements in a vacuum chamber indicate that the intrinsic quality factor exceeds 10,000 even for a fluid filled device. Since frequency stability depends directly on the quality factor, we conclude that an improved vacuum package would enable more than a tenfold gain in mass resolution. The pressure of residual gas in the glass frit package may be estimated by comparing the quality factor of packaged devices to a measurement of Q vs. pressure in the external vacuum; this result is shown in Figure 6-4. For comparison, the plot shows Q of a device filled with a 50 mPa s viscosity standard in addition to the measurement of a dry resonator. In both cases, the pressure dependence agrees with the model for air damping given by Equation 6.7. A quality factor of 700 corresponds to $\sim$1 Torr ambient pressure. Air molecules at this pressure have a mean free path of 49 μm,[3] which is comparable to the width of the cantilever as well as to the gap between the cantilever surface and the cover glass. The quality factor in this regime is inversely proportional to pressure down to a few milli-Torr, at which point intrinsic damping starts to limit the Q. In conclusion, an ideal package would be hermetically sealed with an intra cavity pressure of approximately 1 mTorr. Application of getters inside the cavity can reduce the pressure to this level. [59]

6.2   Sensitivity

The sensitivity of suspended microchannel resonators was calibrated by measuring the shift in resonance frequency while the device was filled with fluids of different density. For small mass changes a linear approximation for the relationship between density and resonance frequency is sufficient, and we define the density sensitivity S_ρ through

$$\frac{\Delta\omega_0}{\omega_0} = -S_\rho \Delta\rho \quad . \tag{6.10}$$

S_ρ has units of $(\text{g·cm}^{-3})^{-1}$ and is related to the slope of $\omega_0^{-2}(\rho)$ that is sometimes used to characterize fluid density sensors by $\partial\omega_0^{-2}/\partial\rho = 2S_\rho/\omega_0^2$. [74] The linear

---

[3]The mean free path in air at 20 °C and at atmospheric pressure is 64 nm [1].
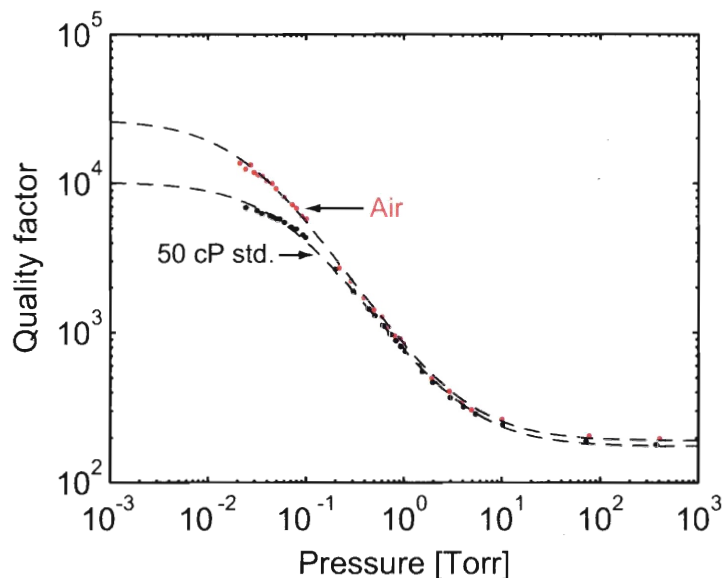
Figure 6-4: The quality factor of a cantilever resonator (type III, Figure 3-1) was measured inside a vacuum chamber. Q for the same type of resonator with on-chip vacuum was 300–700 (dry). Comparison with the plot reveals a value of 1-5 Torr for the sealed devices.

approximation is generally sufficient for the small changes that are typically measured in biomolecular binding experiments.

Samples of well defined density were prepared by dissolving different amounts of sodium chloride in distilled water. Sodium chloride was purchased from Sigma-Aldrich Inc. (St. Louis, MO), and pure water (resistivity 18.2 MΩ·cm) was prepared using a Millipore filtration unit. All measurements were done under continuous flow conditions at a rate of 5 μL/min delivered by an Agilent 1100 HPLC system. The inlet pressure on the resonator was controlled by the length and diameter of the waste line, as described in more detail in section 5.2. The resonance frequency was monitored continuously using the feedback configuration described in chapter 5, and linear drift was subtracted off line.

Figure 6-5 shows the response of a cantilever and a torsional resonator to a sequence of sample injections. Every time a sample plug reached the resonator, the frequency dropped rapidly, equilibrated for a short time, and then returned to the initial value. Although the equilibrium phases in Figure 6-5(a) are too short to be
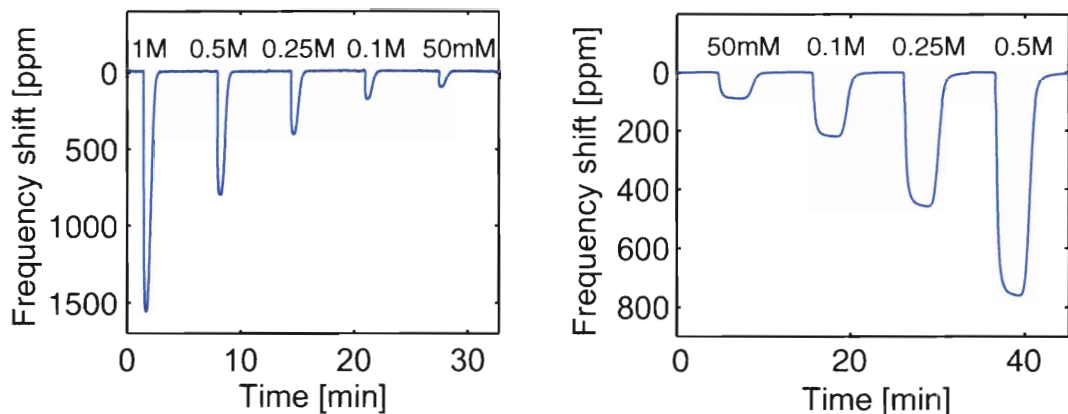
(a) Cantilever (type III, Figure 3-1), 0 ppm $\hat{=}$ 32.269 kHz.

(b) Torsional Resonator, 0 ppm $\hat{=}$ 601.732 kHz.

Figure 6-5: Response of a cantilever (a) and a torsional resonator (b) to various concentrations of sodium chloride in water. Concentrations in mol/L are indicated above each injection peak.

visible on the time scale shown, higher resolution plots of the individual peaks clearly reveal that the peak frequencies represent steady levels and not just transient maxima. The slow tailing at the end of each injection is a common artifact in liquid chromatography caused by mixing in the tubes through which the sample is delivered.

The measured peak frequency shifts were plotted as a function of density using tabulated values of the density of aqueous sodium chloride solutions [40], as shown in Figure 6.2. The slope of the linear fit to the cantilever data (circles & red solid line) represents the density sensitivity S_ρ=39,700 ppm/(g·cm^{-3}), and the same value applies to the sensitivity of the torsional resonator (squares & black dashed line) to within the experimental error. Since both resonators were designed with very similar channel cross-section their sensitivities are expected to match closely. The measured value of S_ρ is ~20% lower than the design value of 49,800 ppm/(g·cm^{-3}) (c.f. Equation 2.7), which is most likely a result of fabrication tolerances, and, in particular, the uncertainty in the height of the fluid channel introduced by dishing of the CMP.
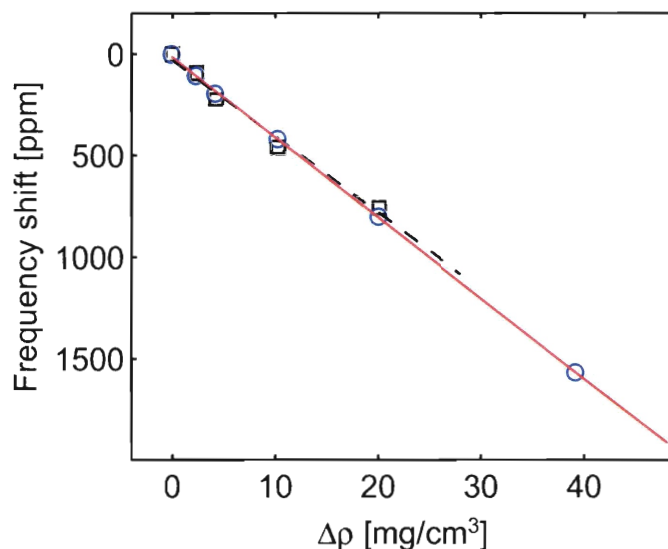
95

Figure 6-6: Measuring the resonance frequency shift as a function of fluid density provides a calibration for mass sensitivity. A linear function has been fitted to the peak frequency shifts of the cantilever (circles & red solid line) and torsional resonator (squares & black dashed line) measurements shown in Figure 6-5. Both devices exhibit an almost identical density sensitivity of $\sim$40,000 ppm/(g/cm^3).

More important than the density sensitivity itself is the derived sensitivity to surface adsorbed mass. Biomolecule concentrations in real samples are generally too low to be detectable by bulk density. Furthermore, molecular specificity relies on the presence of immobilized receptors on the interior channel surface, and the receptor density together with the ligand concentration and binding affinity determine how much mass builds up on the surface. By using the surface mass sensitivity as a performance metric, it is possible to separate the problem of surface preparation and assay development from that of device design. The frequency shift per adsorbed mass is related to the density sensitivity through $S_{\text{surface}} = S_\rho \cdot (A/l)^{-1}$, A/l is the ratio of the channel cross-section area to the cross-sectional length of the solid-liquid interface. For a channel that is much wider than tall the aspect ratio is approximately $(A/l) \approx 2d$, where d denotes the height of the channel. With $d \approx 1$ μm, the measured density sensitivity translates into 0.8 ppm/(ng·cm^{-2}); combined with the frequency resolution of $\sim$0.1 ppm,[4] this yields a mass resolution of 0.13 ng·cm^{-2}.

---

[4]Short term noise in a 1 Hz bandwidth. This noise level has also been maintained over a period of 1 h when the signal from a reference resonator was subtracted.

6.3 Crosstalk

6.3.1 Pressure

Micromechanical structures with thin diaphragms are frequently employed as highly sensitive pressure transducers. Pressure induced strain in a membrane can be measured with high precision by a variety of methods, such as integrated piezoresistors or capacitive or optical displacement sensors. Static deflection and resonance frequency both change under the influence of pressure, and the effect on resonance frequency is of concern when the same signal is to provide information about the adsorption of minute amounts of mass. Controlling pressure to high accuracy in a flow through system requires sophisticated instrumentation and is only an option if the sensor is to be part of a high-end laboratory instrument.

The sensitivity of hollow cantilever and torsional resonators to variations in internal channel pressure was determined experimentally. Depending on the design, the pressure fluctuation equivalent to a frequency noise of 0.1 ppm was found to be $1.3 \cdot 10^{-3}$ psi (9 Pa) or $39 \cdot 10^{-3}$ psi (265 Pa). This means that in order for the resolution not to be degraded, the pressure inside the microfluidic inlet and outlet bypasses must be controlled to approximately 10^{-3} psi.

Measurements were performed on dry channels filled with nitrogen (grade 5.0). To prevent uncontrolled gas flow inside the device, the two microfluidic bypasses were connected together in series and the output of the second bypass was plugged. The pressure applied to the inlet of the first bypass was adjusted using a mechanical regulator while the resonance frequency of the sensor was monitored continuously with the oscillator method.

Figure 6-7 shows that the resonance frequency increases linearly with pressure in the range of 0–80 psi. The positive sign of the slope is consistent with an increasing spring constant as expected for a channel whose cross section is expanded by the deflection of the walls under pressure. Inserting the design values for the cantilever geometry into equation 2.28 and 2.24 yields a value of 115 ppm/psi, which is in reasonable agreement with the experiment considering the simplifying assumptions
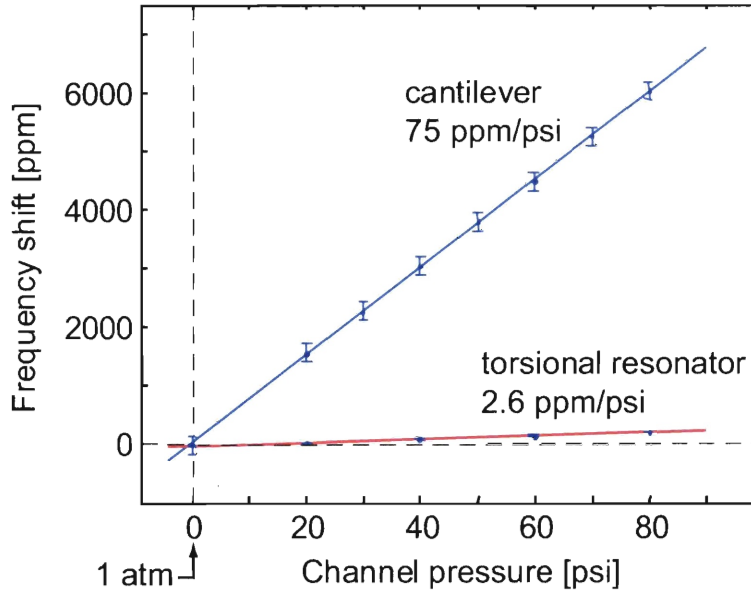
Figure 6-7: The resonance frequency of hollow cantilever (type III, Figure 3-1) and torsional resonators depends on the internal channel pressure. The channel width of the torsional resonator is 10 μm and that of the cantilever is 20 μm. Measurements were performed in the lowest transverse vibrational mode of the cantilever and in the antisymmetric torsional mode of the torsional resonator.

made by the model. Specifically, assuming that the top and bottom diaphragm can both deflect equally at the base of the cantilever may lead to over-estimation of the pressure coefficient.

Although no explicit calculation was performed for the torsional resonator, the almost thirty times lower sensitivity to pressure is generally expected since the channel is only ten instead of twenty micron wide. Therefore, the top and bottom of the channel will bulge sixteen times less and result in less stiffening of the support flexures.

6.3.2 Bias voltage

The resonance frequency of electrostatically driven micromechanical resonators depends on the square of the applied bias voltage as shown in section 2.3.3. Small voltage fluctuations cause frequency shifts that are in direct proportion to the product of bias voltage and voltage noise and inversely proportional to the spring constant (c.f. Equation 2.33). The voltage dependence of resonance frequency for cantilever
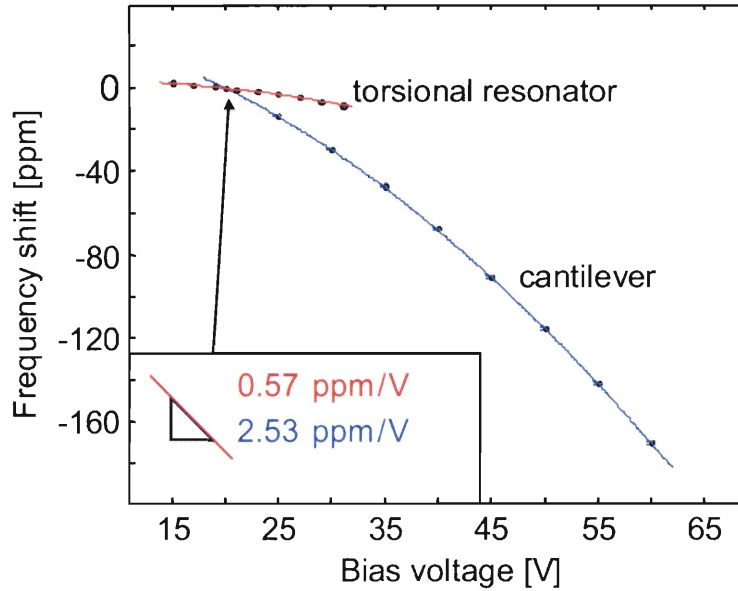
Figure 6-8: The resonance frequency of electrostatically actuated resonators decreases as the square of the bias voltage. The torsional resonators are less sensitive to bias variations than the relatively compliant cantilever devices (type III, Figure 3-1). Measurements were performed in the lowest transverse vibrational mode of the cantilever and in the antisymmetric torsional mode of the torsional resonator.

and torsional resonators was characterized experimentally by operating the resonator in feedback at varying bias voltages and monitoring the resonance frequency. Active control of the feedback gain enabled the change in resonance frequency to be separated from the dependence of the oscillator frequency on bias voltage. Increasing the bias effectively amplifies the force exerted by the electrostatic actuator, thereby increasing the overall feedback gain and altering the oscillation frequency. Although the oscillation frequency is independent of gain when the feedback phase is adjusted to precisely ninety degree, the required phase accuracy can not be achieved in practice because of component tolerances and drift. By actively controlling the gain of the feedback amplifier to maintain a constant vibration amplitude, the increased efficiency of the electrostatic actuator at higher biases was compensated by a concomitant reduction in electronic gain.

Figure 6-8 illustrates how the measured resonance frequencies of the cantilever and the torsional resonator follow the expected dependence on the square of the bias
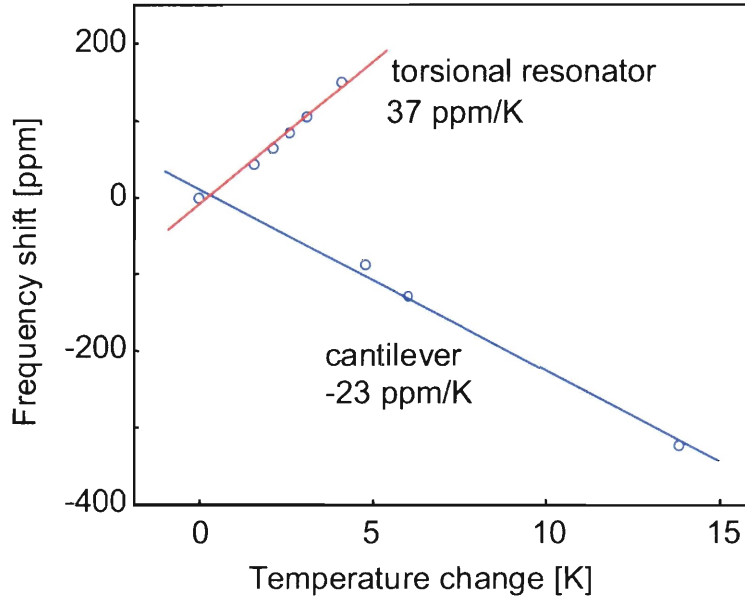
Figure 6-9: The temperature sensitivity of cantilevers and torsional resonators is similar in magnitude but opposite in polarity. Cantilevers become more compliant with increasing temperature due to a decrease in Young's modulus. Torsional resonators also respond to tensile stress induced by heating. Measurements were performed in the lowest transverse vibrational mode of the cantilever and in the antisymmetric torsional mode of the torsional resonator.

voltage. The slope of ~ -2.5 ppm/V at 20 V bias in the case of the cantilever is slightly lower than the value of 3.2 ppm/V predicted by Equation 2.33.[5]

6.3.3 Temperature

All physical transducers are susceptible to temperature induced measurement errors. Resonant mass sensors are influenced by temperature primarily through changes in material properties and thermal stress induced by mismatch between the thermal expansion coefficient of structural components made from different materials. A water filled resonator is further subject to a reduction in total mass when the device is heated, for the density of water has a negative temperature coefficient at room temperature. At 25°C, the density of water changes by -0.256 (mg/cm^3)/°C, which in combination with the device sensitivity of 40,000 ppm/(g·cm^3) yields a temperature

---

[5]The value of 3.2 ppm/V was calculated using the design parameters for spring constant (k=1 N/m), capacitance (C_0=0.79 fF) and gap size (d=70 μm).

coefficient of $\sim$10 ppm/$^\circ$C.

The temperature sensitivity of unfilled cantilevers and torsional resonators has been characterized experimentally. Measurements were done on dry devices in order to be able to separate the intrinsic temperature coefficient (TC) of the device from density changes of the fluid. Frequency was measured continuously by the oscillator method and stable feedback gain was ensured through automatic gain control. The temperature of the device was increased by resistively heating the metallic clamping plate by which the chip was held on the teflon manifold (c.f. Figure 5-9(a)). The temperature was measured with a thermocouple mounted in a recess between the resistive heater and the plate.

Figure 6-9 plots the measured dependence of resonance frequency on temperature. The negative TC of the cantilever device is consistent with a reduction in Young's modulus as reported by Radenovic et al. [47]. While the resonance frequency of cantilevers is not significantly affected by thermal expansion, torsional resonators are sensitive to stress resulting from a mismatch in the coefficient of thermal expansion (CTE) of the silicon substrate and the structural thin film. Toivola et al. [68] measured a CTE of 2.2 ppm/$^\circ C$ for low-stress LPCVD silicon nitride, which is lower than the value of 2.6 ppm/$^\circ C$ for single-crystal silicon. Although the deposition conditions used in [68] were not identical to those of this work, we assume that the CTE of our silicon nitride film is also lower than that of silicon.[6] A lower thermal expansion of the nitride film relative to the substrate results in tensile strain in the torsional resonator upon heating. Finite element calculation of the resonance frequency with and without application of pre-stress (c.f. Figure 3-6(b)) predicts a stress-sensitivity of -0.7 ppb/MPa (with compressive stress positive). A CTE mismatch of 0.4 ppm/$^\circ$C together with E=180 GPa for silicon nitride [35] then yields a temperature coefficient of +50 ppm/$^\circ C$ for the resonance frequency, which may be combined linearly with the TC caused by changes in material properties. The combination of the two effects yields a predicted TC of 37 ppm/$^\circ$C which is in good agreement with the experiment.[7]

---

[6]Toivola et al. obtained almost the same value over a wide range of conditions and even lower CTEs have been reported for stoichiometric silicon nitride [29].

[7]The exact equality of the values is likely a coincidence. We expect a tolerance of at least $\pm$20%

In conclusion, temperature sensitivity may introduce significant errors in non-differential measurements, as even changes on the order of 0.001 °C result in signals that are similar to the noise floor of ~0.1 ppm. While differential sensing can effectively suppress small disturbances caused by fluctuations in ambient temperature, the problem is more severe when the sensor and reference are exposed to different fluids whose temperature is not precisely matched.

6.4 Binding Experiments

The ability to detect biomolecular binding inside the suspended microchannel resonator has been demonstrated by first functionalizing the sensor with avidin and subsequently measuring the mass increase due to binding of different biotin labeled proteins. Binding between biotin and avidin is the strongest non-covalent interaction in biology and avidin can be reliably physisorbed to solid surfaces. While biotin by itself is a very small molecule whose mass would be difficult to detect directly, biotin conjugated proteins may be captured by the same interaction on avidin coated surfaces. This section describes results for the detection of two biotinylated proteins: biotin bovine serum albumin (bBSA) and biotin labeled anti green fluorescent protein (anti-GFP). Measuring the binding of these proteins proves that thin suspended microchannel resonators are a viable method for the mass sensitive detection of proteins in solution.

Avidin was first immobilized on the channel surface by non-specific adsorption from a 1 mg/mL solution in phosphate buffered saline (PBS) at pH 7.4 and a salt concentration of 10 mM NaCl. Lyophilized avidin and bBSA were purchased from Sigma-Aldrich Inc. (St. Louis, MO) and diluted in the same running buffer that was used during the experiment. bBSA was labeled with 8-16 mol biotin per mol BSA, as specified by the manufacturer. Monoclonal GFP antibodies labeled with 10-20 mol/mol biotin were purchased from Rockland Inc. (Gilbertsville, PA). The proteins came in a storage solution of phosphate buffered saline at pH 7.2 containing

---

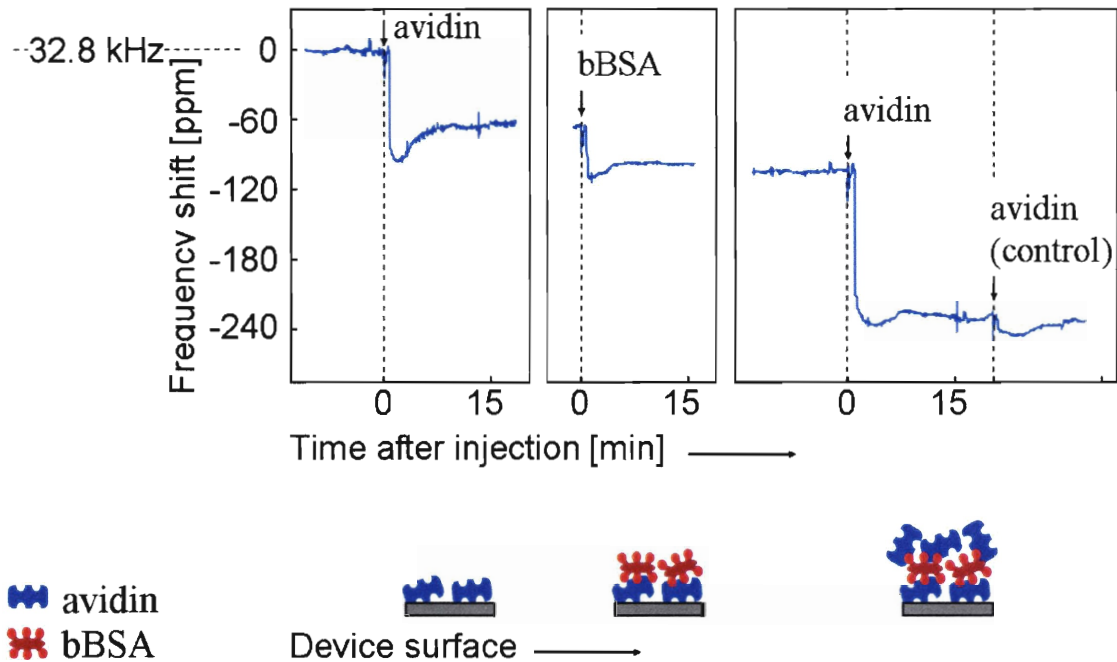for the TC predicted by finite element calculation.

Figure 6-10: Avidin and biotinylated BSA are detected by the resonance frequency shift upon binding. The transient dip during the injections is due to the greater density of the sample compared to the running buffer.

150 mM Sodium Chloride, 10 mg/mL BSA as stabilizer and 0.01% (w/v) Sodium Azide as a preservative; this solution was used undiluted. Constant flow at a rate of 5 μL/min through the microfluidic inlet bypass was maintained during the experiments. A 15 inch long tube with 75 um inner diameter connected between the outlet of the injection bypass and the waste reservoir induced a pressure of 6psi at the resonator inlet; this gave rise a small flow of $\sim$30 pL/s inside the suspended microchannel. Since the resonator comprises a volume of only 6 pL plus 14 pL of dead volume between the inlet and the base of the suspended channel, it takes less than one second to completely exchange the fluid inside the vibrating beam. The resonator outlet connects to a large bypass channel, which was continuously rinsed at a slow flow rate (1 μL/min) and at low pressure. The running buffer in the inlet was delivered by an Agilent 1100 HPLC system with inline degasser, and samples were injected with an autosampler as described in section 5.2. The frequency shift vs. time after injecting avidin into a new cantilever is plotted in Fig. 6-10 with arrows

labeling the times at which the sample loop was connected to the device. Less than one minute after the injection, which corresponds to the time it took for the sample to flow from the injection valve to the sensor, the frequency dropped by about 90 ppm and settled at an equilibrium value of -60 ppm after the sample was washed out. The rise of the signal during rinsing can be explained by the difference in bulk density between the protein solution and the running buffer, and by loosely bound molecules detaching from the surface. Assuming a bulk density of 1.3-1.4 g/cm^3 for avidin a solution concentration of 1 mg/mL would give rise to a signal of only ~10 ppm. The final frequency shift of -60 ppm corresponds to ~300–400 ng/cm^2 of dry protein mass, a value that is similar to levels of albumin adsorption on silicon dioxide surfaces reported by Zhang et al. [80] and by Nakanishi et al. [44].[8]

After rinsing the device with PBS for more than 20 min, we injected biotin conjugated Bovine Serum Albumin (bBSA) which bound to the avidin present on the surface. The initial signal of ~40 ppm exceeds the equilibrium value by 10 ppm, consistent with the density difference between the pure buffer and the bBSA solution. Again rinsing with PBS revealed the true mass change due to the BSA attached to the surface. Since each mol of BSA was labeled with 8-16 mol of biotin it was now possible to build up another layer of avidin molecules as illustrated in the last panel of Fig. 6-10.

Several control experiments were conducted to ensure that the observed signals were indeed caused by specific binding of bBSA to avidin rather than being the result of non-specific adsorption or measurement artifacts. First, injecting solutions without proteins never resulted in a permanent change of the baseline, indicating that the signal was robust to disturbances caused by the switching. Second, specificity was verified by repeating the experiment with regular BSA in place of bBSA, leading to no detectable mass signal. The same behavior resulted after two consecutive injections of avidin, as shown in the last panel in Fig. 6-10: Only the first of the two sample plugs

---

[8]Zhang et al. used ellipsometry to measure an adsorbed mass density of 250 ng/cm^2 for 1 mg/mL Human Serum Albumin on silicon dioxide. The review by Nakanishi et al. quotes a value of 170 ng/cm^2 for Bovine Serum Albumin on silica gel, and 140 ng/cm^2 Human Serum Albumin on glass.
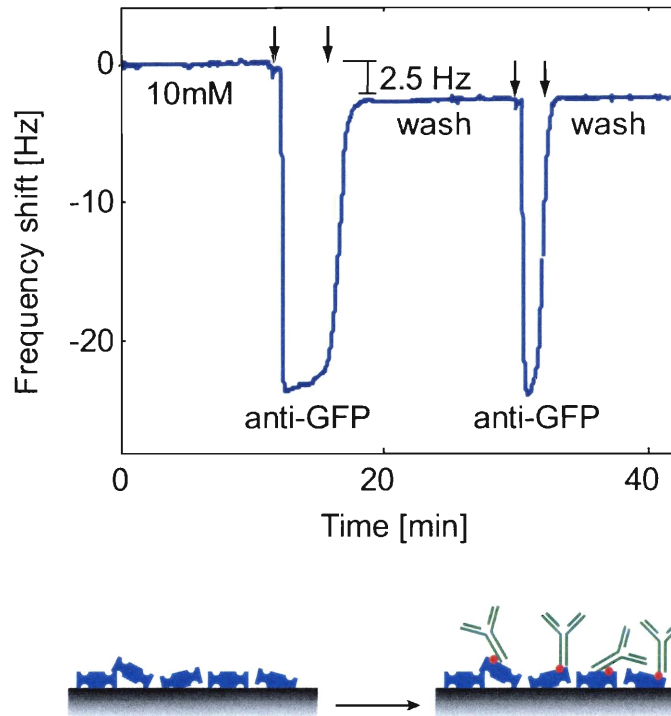
Figure 6-11: Binding of biotin conjugated anti-GFP to avidin. The large transient signals result from a difference in salt concentration between the sample and the running buffer. After the first injection, a residual frequency shift of 2.5 Hz indicates binding of anti-GFP. A frequency shift of zero corresponds to a resonance frequency of 33 kHz.

showed evidence of binding, while the second passed over the surface without leaving any deposits, presumably owing to a lack of available binding sites. Physisorption of avidin is a simple and versatile method for surface functionalization. Fig. 6-11 shows the immobilization of biotin conjugated anti-GFP to an avidin coated device. The sample was injected twice to ensure complete saturation of the surface. The periods during which the sample passed through the resonator can be recognized by the large transient frequency shift caused by the higher salt concentration of the anti-GFP solution (150 mM NaCl). In addition, the sample also contained a background of 10 mg/mL BSA. When rinsing out the anti-GFP solution the amount of bound protein could be identified by the difference in baseline before and after the experiment.

Chapter 7

Conclusions

This thesis has introduced a new device concept for the label-free detection of biological molecules by mass: Adsorption of molecules to the inside walls of a suspended microfluidic channel is detected by measuring the change in mechanical resonance frequency of the channel. In contrast to resonant mass sensors submersed in water, the sensitivity and frequency resolution of our device is not degraded by the presence of the fluid.

The primary feature that sets our work apart from research in the area of vibrating tube densitometers is that molecules that bind to the channel walls are detected, thereby providing a path to specificity via molecular recognition by immobilized receptors such as antibodies. We have therefore optimized the design for sensitivity to surface mass; this requires the fluid channel and the walls of the hollow resonator to be very thin.

Calculation of the intrinsic noise and the sensitivity of suspended microchannel resonators indicate that the physical limit for mass resolution in a 1 Hz bandwidth is approximately 0.01 ng/cm^2. A resolution of $\sim$0.1 ng/cm^2 has been experimentally demonstrated in this work. This resolution constitutes a tenfold improvement over commercial quartz crystal microbalance based instruments.

Sample depletion poses a potential challenge for the detection of low-abundance proteins in micrometer tall fluid channels. Although the time dependent mass transport in thin channels is not investigated in detail in this thesis, the important time-

and length-scales are pointed out. Specific examples illustrate that in one microme-ter tall channels, sample depletion is only significant for biochemical reactions that are typically considered fast, and depletion in three micrometer channels is generally negligible.

One limitation of the current design is the high flow resistance of the thin channels: At low flow rates, a dilute sample needs to flow through the resonator for a very long time before a detectable amount of target molecules can accumulate. Measurements at picomol per liter concentrations are severely limited by the convection rate. This limitation can be greatly alleviated by increasing the channel height to three micron. Mass transport is then dominated by diffusion, and a further increase in channel height would not significantly shorten the detection time.

Suspended microchannel resonators made of silicon nitride with a wall and fluid layer thickness of less than one micron have been fabricated and tested. The channels were fabricated using a polysilicon Damascene process, sacrificial layer etching in hot potassium hydroxide, and bulk micromachining. Two packaging processes integrating electrostatic actuation and microfluidic sample delivery have been developed. The first process is a die-level approach by which individual chips are bonded to a glass substrate via a thin gasket of micromolded PDMS. The second process was based on glass frit bonding of a pyrex capping wafer to the completed device wafer. By bonding under vacuum, the resonators were encapsulated in a low-pressure environment. The main drawback of the glass frit is the incompatibility of the material with solutions of low pH, which precludes the use of certain cleaning and surface regeneration protocols. Chemical compatibility will be addressed in the future by replacing the glass frit bond by other methods, e.g. by anodic or thermocompression bonding.

The measurement of the resonator vibration was based on the optical lever method. Our home-built system enabled a short-term frequency resolution of 0.1 ppm for res-onators with quality factors $\geq$700. A similar frequency resolution could be maintained over a period of at least one hour when drift was reduced by subtracting a reference signal. Likely causes of drift are temperature or pressure fluctuations. Characteriza-tion of the sensitivity of resonance frequency to operating conditions indicates that

temperature changes on the order of 0.1 °C will cause frequency variations of several parts per million, which also is a typical drift amplitude on a one hour timescale. The tested cantilever and torsional resonators had similar temperature coefficients, however torsional resonators with channels that were only ten instead of twenty micron wide were thirty times less sensitive to pressure fluctuations.

Long-term stability can be addressed through differential sensing, environmental control, and design for minimum sensitivity to operating conditions. Low short-term noise, on the other hand, depends on a high mechanical quality factor. Measurements with fluid filled cantilevers conducted under vacuum reveal that Q exceeds 10,000 at a pressure of $\sim$30 mTorr. To the best of our knowledge, no micromachined resonant transducers with a quality factor greater than 200 in liquid and sufficient sensitivity for biomolecular detection have been previously reported.

The theoretical limit for mass resolution predicted by the measured sensitivity and quality factor in a 30 mTorr vacuum is approximately 0.01 ng/cm^2 (1 Hz bandwidth), or the equivalent of one 100 kDa protein per square micron; at this level, the device would present a viable alternative to fluorescent detection. Improved vacuum packaging and environmental control are needed to exploit this potential. Furthermore, sensitive and selective biological assays require covalent coupling of capture antibodies and surface passivation to guard against non-specific binding. More work in the area of surface functionalization and chemical compatibility of the current device is required to address these issues.
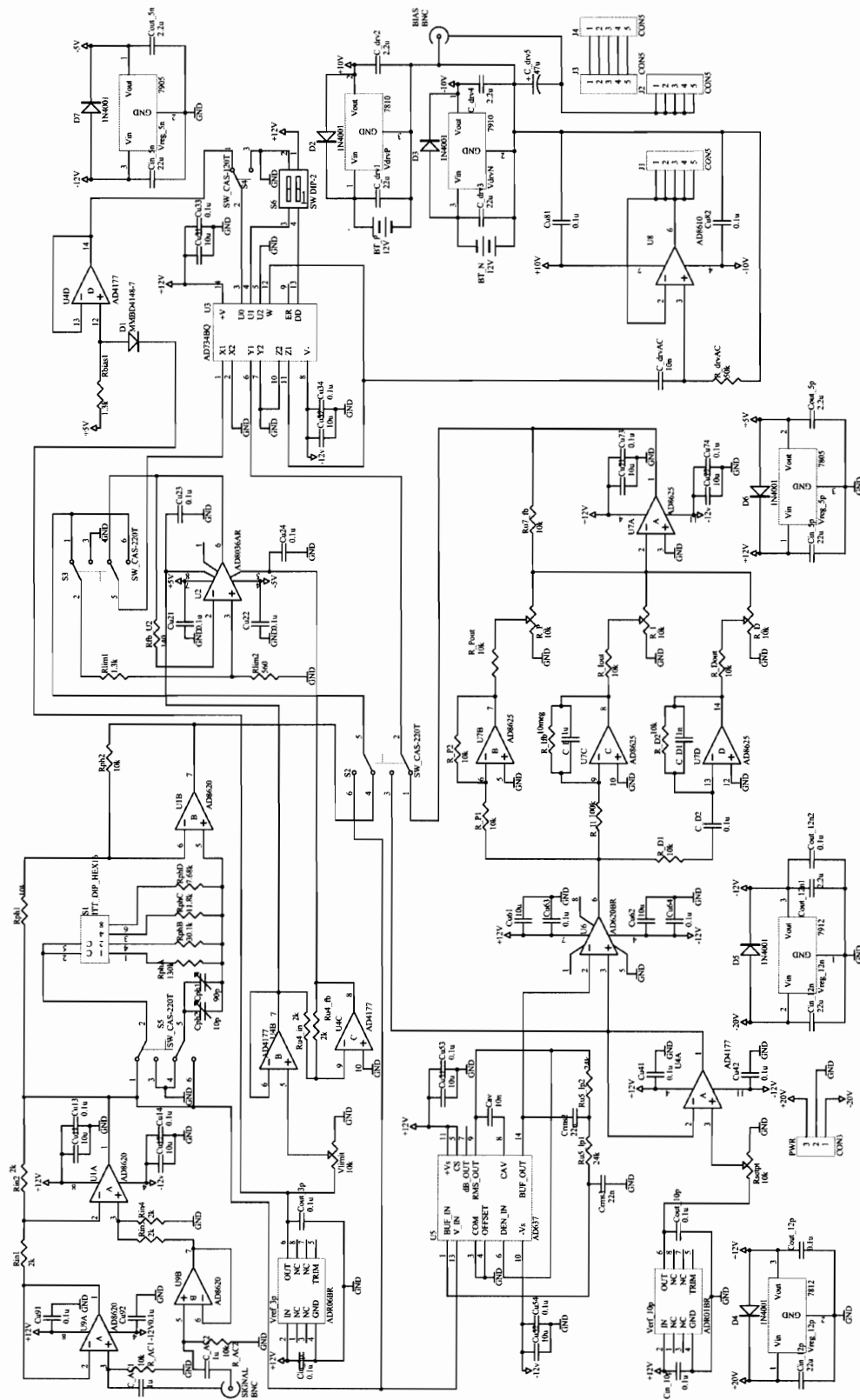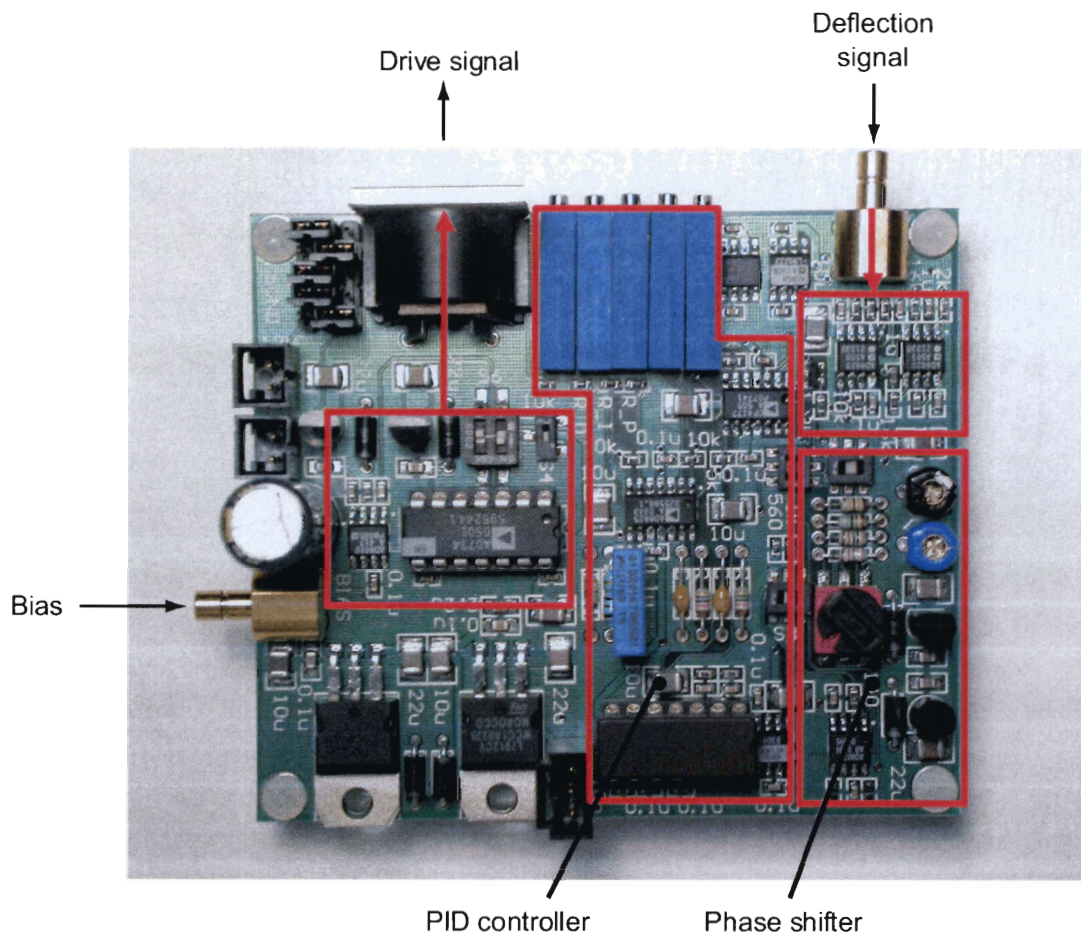
Appendix A

Circuit schematics

A.1 Photodetector
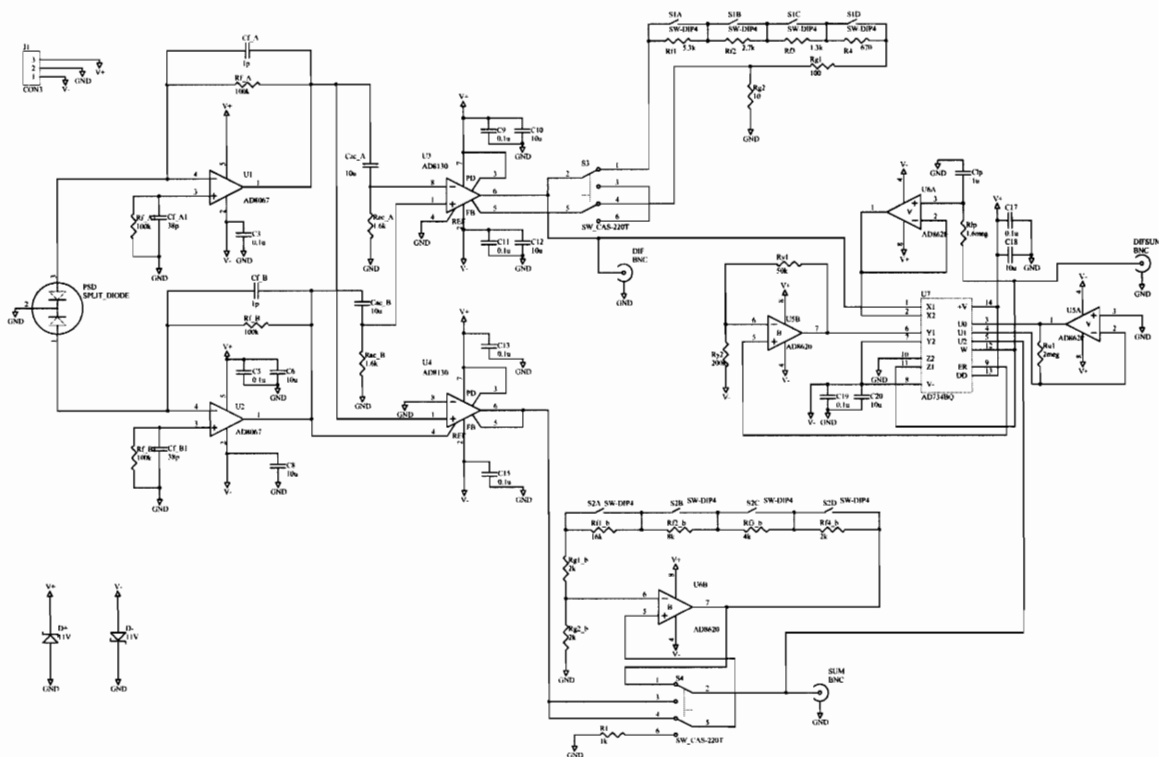
A.2 Gain controlled oscillator

Drive signal

Deflection signal

Bias

PID controller

Phase shifter

Bibliography

[1] W. Benenson, J.W. Harris, H. Stocker, and H. Lutz, editors. *Handbook of Physics*. Springer-Verlag, New York, 2002.

[2] J. W. Berenschot, N. R. Tas, T. S. J. Lammerink, M. Elwenspoek, and A. van den Berg. Advanced sacrificial poly-Si technology for fluidic systems. *Journal of Micromechanics and Microengineering*, 12(5):621–4, 2002.

[3] A. Brecht and G. Gauglitz. Recent developments in optical transducers for chemical or biochemical applications. *Sensors and Actuators, B: Chemical*, B38(1-3 pt 1):1–7, 1997.

[4] G.M. Brown. Heat or mass transfer in a fluid in laminar flow in a circular or flat conduit. *A.I.Ch.E. Journal*, 1960.

[5] T. P. Burg and S. R. Manalis. Suspended microchannel resonators for biomolecular detection. *Applied Physics Letters*, 83(13):2698–700, 29.

[6] T.P. Burg and S.R. Manalis. Microfluidic packaging of suspended microchannel resonators for biomolecular detection. In *Proceedings of the 3RD IEEE-EMBS Conference on Microtechnologies in Medicine and Biology, Kahuku, Oahu (HI)*, pages 264–267, 2005.

[7] T.P. Burg, A.R. Mirza, C.H. Tsau, N. Milovic, G.A. Popescu, J. Foster, and S.R. Manalis. Vacuum packaged suspended microchannel resonant mass sensors for biomolecular detection. *Journal of Microelectromechanical Systems*. (in preparation).

[8] H. R. Chen, C. Gau, B. T. Dai, and M. S. Tsai. A novel planarization process for polysilicon sacrificial layers in a micro-thermal system. *Sensors and Actuators, A: Physical*, 108(1-3):86–90, 2003.

[9] E. B. Cooper, J. Fritz, G. Wiegand, P. Wagner, and S. R. Manalis. Robust microfabricated field-effect sensor for monitoring molecular adsorption in liquids. *Applied Physics Letters*, 79(23):3875–7, 2001.

[10] T. Corman, P. Enoksson, and G. Stemme. Deep wet etching of borosilicate glass using an anodically bonded silicon substrate as mask. *Journal of Micromechanics and Microengineering*, 8(2):84–87, 1998.

[11] Y. Cui, Q. Q. Wei, H. K. Park, and C. M. Lieber. Nanowire nanosensors for highly sensitive and selective detection of biological and chemical species. *Science*, 293(5533):1289–1292, 2001.

[12] K. L. Ekinci, Y. T. Yang, and M. L. Roukes. Ultimate limits to inertial mass sensing based upon nanoelectromechanical systems. *Journal of Applied Physics*, 95(5):2682–2689, 2004.

[13] P. Enoksson, G. Stemme, and E. Stemme. Silicon tube structures for a fluid density sensor. In *Proceedings of the International Solid-State Sensors and Actuators Conference - TRANSDUCERS '95, 25-29 June 1995*, 1995.

[14] P. Enoksson, G. Stemme, and E. Stemme. A Coriolis mass flow sensor structure in silicon. In *Proceedings of Ninth International Workshop on Micro Electromechanical Systems, 11-15 Feb. 1996*, 1996.

[15] P. Enoksson, G. Stemme, and E. Stemme. Vibration modes of a resonant silicon tube density sensor. *Journal of Microelectromechanical Systems*, 5(1):39–44, 1996.

[16] P. Enoksson, G. Stemme, and E. Stemme. A silicon resonant sensor structure for Coriolis mass-flow measurements. *Journal of Microelectromechanical Systems*, 6(2):119–25, 1997.

[17] J. M. Friedt, L. Francis, G. Reekmans, R. De Palma, A. Campitelli, and U. B. Sleytr. Simultaneous surface acoustic wave and surface plasmon resonance measurements: Electrodeposition and biological interactions monitoring. *Journal of Applied Physics*, 95(4):1677–1680, 2004.

[18] J. Fritz, E. B. Cooper, S. Gaudet, P. K. Sorger, and S. R. Manalis. Electronic detection of DNA by its intrinsic molecular charge. *Proceedings of the National Academy of Sciences of the United States of America*, 99(22):14142–14146 ER, 2002.

[19] A. L. Ghindilis, P. Atanasov, M. Wilkins, and E. Wilkins. Immunosensors: Electrochemical sensing and other engineering approaches. *Biosensors & bioelectronics*, 13(1):113–131, 1998.

[20] C. Hagleitner, A. Hierlemann, D. Lange, A. Kummer, N. Kerness, O. Brand, and H. Baltes. Smart single-chip gas sensor microsystem. *Nature*, 414(6861):293–296, 2001.

[21] C. Hagleitner, D. Lange, O. Brand, A. Hierlemann, and H. Baltes. A single-chip CMOS resonant beam gas sensor. In *Digest of Technical Papers - IEEE International Solid-State Circuits Conference, Feb 5-6 2001*, 2001.

[22] J. Homola, S. S. Yee, and G. Gauglitz. Surface plasmon resonance sensors: review. *Sensors and Actuators B (Chemical)*, B54(1-2):3–15, 1999.

[23] F. Hook, B. Kasemo, T. Nylander, C. Fant, K. Sott, and H. Elwing. Variations in coupled water, viscoelastic properties, and film thickness of a Mefp-1 protein film during adsorption and cross-linking: A quartz crystal microbalance with dissipation monitoring, ellipsometry, and surface plasmon resonance study. *Analytical Chemistry*, 73(24):5796–5804, 2001.

[24] H. Hosaka, K. Itao, and S. Kuroda. Damping characteristics of beam-shaped micro-oscillators. *Sensors and Actuators, A: Physical*, 49(1-2):87–95, 1995.

[25] B. Ilic, H. G. Craighead, S. Krylov, W. Senaratne, C. Ober, and P. Neuzil. Attogram detection using nanoelectromechanical oscillators. *Journal of Applied Physics*, 95(7):3694–3703, 2004.

[26] B. Ilic, D. Czaplewski, M. Zalalutdinov, H. G. Craighead, P. Neuzil, C. Campagnolo, and C. Batt. Single cell detection with micromechanical oscillators. *Journal of Vacuum Science and Technology B: Microelectronics and Nanometer Structures*, 19(6):2825–2828, 2001.

[27] B. Ilic, Y. Yang, and H. G. Craighead. Virus detection using nanoelectromechanical devices. *Applied Physics Letters*, 85(13):2604–2606, 2004.

[28] D. James, S. M. Scott, Z. Ali, and W. T. O'Hare. Chemical sensors for electronic nose systems. *Microchimica Acta*, 149(1-2):1–17, 2005.

[29] T. F. Retajczyk Jr and A. K. Sinha. Elastic stiffness and thermal expansion coefficients of various refractory silicides and silicon nitride films. *Thin Solid Films*, 70(2):241–7, 1980.

[30] A. Kaushik, H. Kahn, and A. H. Heuer. Wafer-level mechanical characterization of silicon nitride MEMS. *Journal of Microelectromechanical Systems*, 14(2):359–367, 2005.

[31] A. Khan, J. Philip, and P. Hess. Young's modulus of silicon nitride used in scanning force microscope cantilevers. *Journal of Applied Physics*, 95(4):1667–1672, 2004.

[32] U. Kloter, H. Schmid, H. Wolf, B. Michel, and D. Juncker. High-resolution patterning and transfer of thin PDMS films: FABRICATION of hybrid self-sealing 3D microfluidic systems. In *17th IEEE International Conference on Micro Electro Mechanical Systems (MEMS): Maastricht MEMS 2004 Technical Digest, Jan 25-29 2004*, 2004.

[33] J. D. Koh, D. W. Suh, D. W. Han, J. W. Kim, N. H. Park, and S. B. Han. Investigations in polysilicon CMP to apply in sub-quarter micron DRAM device.

In *ICVC'99. 6th International Conference on VLSI and CAD, 26-27 Oct. 1999*, 1999.

[34] B. Konig and M. Gratzel. A Novel Immunosensor for Herpes Viruses. *Analytical Chemistry*, 66(3):341–344, 1994.

[35] J. Lai, T. Perazzo, Z. Shi, and A. Majumdar. Optimization and performance of high-resolution micro-optomechanical thermal sensors. *Sensors and Actuators, A: Physical*, 58(2):113–119, 1997.

[36] D. Lange, C. Hagleitner, A. Hierlemann, O. Brand, and H. Baltes. Complementary metal oxide semiconductor cantilever arrays on a single chip: Mass-sensitive detection of volatile organic compounds. *Analytical Chemistry*, 74(13):3084–3095, 2002.

[37] N. V. Lavrik, M. J. Sepaniak, and P. G. Datskos. Cantilever transducers as a platform for chemical and biological sensors. *Review of Scientific Instruments*, 75(7):2229–2253, 2004.

[38] G. Li and H. Hughes. Review of viscous damping in micro-machined structures. In *Micromachined Devices abd Components VI, Sep 18-Sep 19 2000*, volume 4176 of *Proceedings of SPIE - The International Society for Optical Engineering*, pages 30–46, 2000.

[39] P. C. H. Li and M. Thompson. Mass sensitivity of the thin-rod acoustic wave sensor operated in flexural and extensional modes. *Analytical Chemistry*, 68(15):2590–2597, 1996.

[40] D. R. Lide, editor. *CRC Handbook of Chemistry and Physics*. CRC Press, 85th edition, 2004.

[41] W. Lukosz. Integrated-optical biosensors. *Abstracts of Papers of the American Chemical Society*, 213:210–ANYL, 1997.

[42] M. Maute, S. Raible, F. E. Prins, D. P. Kern, H. Ulmer, U. Weimar, and W. Göpel. Detection of volatile organic compounds (VOCs) with polymer-coated cantilevers. *Sensors and Actuators B-Chemical*, 58(1-3):505–511, 1999.

[43] D. G. Myszka, Xiaoyi He, M. Dembo, T. A. Morton, and B. Goldstein. Extending the range of rate constants available from BIACORE: interpreting mass transport-influenced binding data. *Biophysical journal*, 75(2):583–94, 1998.

[44] K. Nakanishi, T. Sakiyama, and K. Imamura. On the adsorption of proteins on solid surfaces, a common but very complicated phenomenon. *Journal of Bioscience and Bioengineering*, 91(3):233–244, 2001.

[45] C. K. O'Sullivan and G. G. Guilbault. Commercial quartz crystal microbalances - theory and applications. *Biosensors & bioelectronics*, 14(8-9):663–670, 1999.

[46] O. Paul, O. Brand, R. Lenggenhager, and H. Baltes. Vacuum gauging with complementary metal-oxide-semiconductor microsensors. *Journal of Vacuum Science & Technology A: Vacuum, Surfaces, and Films*, 13(3 pt 1):503, 1995.

[47] Alexandra Radenovic, Eva Bystrenova, Laurent Libioulle, Francesco Valle, George T. Shubeita, Sandor Kasas, and Giovanni Dietler. Characterization of atomic force microscope probes at low temperatures. *Journal of Applied Physics*, 94(6):4210–4214, 2003.

[48] A. K. N. Reddy and J. M. Bockris. *Modern Electrochemistry*. Plenum Press, New York, 1998.

[49] J. Rickert, A. Brecht, and W. Göpel. Quartz crystal microbalances for quantitative biosensing and characterizing protein multilayers. *Biosensors & bioelectronics*, 12(7):567–575, 1997.

[50] K. S. Ryu and C. Liu. Precision Patterning of PDMS Thin Films: A New Fabrication Method and Its Applications. In *6th Intl. Symp. on Micro Total Analysis Systems, Nara, Japan*, 2002.

[51] K. S. Ryu, X. Wang, K. Shaikh, and C. Liu. A method for precision patterning of silicone elastomer and its applications. *Journal of Microelectromechanical Systems*, 13(4):568–575, 2004.

[52] J. E. Sader. Frequency response of cantilever beams immersed in viscous fluids with applications to the atomic force microscope. *Journal of Applied Physics*, 84(1):64–76, 1998.

[53] J. E. Sader, J. W. M. Chon, and P. Mulvaney. Calibration of rectangular atomic force microscope cantilevers. *Review of Scientific Instruments*, 70(10):3967–3969, 1999.

[54] C. A. Savran, T. P. Burg, J. Fritz, and S. R. Manalis. Microfabricated mechanical biosensor with inherently differential readout. *Applied Physics Letters*, 83(8):1659–1661, 2003.

[55] C. A. Savran, S. M. Knudsen, A. D. Ellington, and S. R. Manalis. Micromechanical detection of proteins using aptamer-based receptor molecules. *Analytical Chemistry*, 76(11):3194–3198, 2004.

[56] C. A. Savran, A. W. Sparks, J. Sihler, J. Li, W. C. Wu, D. E. Berlin, T. P. Burg, J. Fritz, M. A. Schmidt, and S. R. Manalis. Fabrication and characterization of a micromechanical sensor for differential detection of nanoscale motions. *Journal of Microelectromechanical Systems*, 11(6):703–708, 2002.

[57] D. Schultz, K. Moore, and W. Kautzmann. Protein densities from X-ray crystallographic coordinates. *Nature*, 248:447, 1974.

[58] P. Skladal. Piezoelectric quartz crystal sensors applied for bioanalytical assays and characterization of affinity interactions. *Journal of the Brazilian Chemical Society*, 14(4):491–502, 2003.

[59] D. Sparks, S. Massoud-Ansari, and N. Najafi. Reliable vacuum packaging using NanoGetters™ and glass frit bonding. *Proceedings of the SPIE - The International Society for Optical Engineering*, 5343(1):70–8, 2003.

[60] D. Sparks, S. Massoud-Ansari, and N. Najafi. Long-term evaluation of hermetically glass frit sealed silicon to pyrex wafers with feedthroughs. *Journal of Micromechanics and Microengineering*, 15(8):1560–4, 2005.

[61] D. Sparks, R. Smith, J. Cripe, R. Schneider, and N. Najafi. A Portable MEMS Coriolis Mass Flow Sensor. In *Second International Conference on Sensors: IEEE Sensors 2003, Oct 22-24 2003*, 2003.

[62] D. Sparks, R. Smith, R. Schneider, J. Cripe, S. Massoud-Ansari, A. Chimbayo, and N. Najafi. A variable temperature, resonant density sensor made using an improved chip-level vacuum package. *Sensors and Actuators, A: Physical*, 107(2):119–124, 2003.

[63] D. Sparks, R. Smith, M. Straayer, J. Cripe, R. Schneider, S. Massoud-Ansari, and N. Najafi. A microfluidic system for the measurement of chemical concentration and density. In *IEEE International Solid-State Sensors and Actuators Conference, 8-12 June 2003*, 2003.

[64] D. R. Sparks, S. Massoud-Ansari, and N. Najafi. Chip-level vacuum packaging of micromachines using NanoGetters. *IEEE Transactions on Advanced Packaging*, 26(3):277–82, 2003.

[65] I. Stemmler, A. Brecht, and G. Gauglitz. Compact surface plasmon resonance-transducers with spectral readout for biosensing applications. *Sensors and Actuators, B: Chemical*, 54(1):98–105, 1999.

[66] M. B. Stern, M. W. Geis, and J. E. Curtin. Nanochannel fabrication for chemical sensors. *Journal of Vacuum Science & Technology B (Microelectronics and Nanometer Structures)*, 15(6):2887–91, 1997.

[67] T. Thundat, E. A. Wachter, S. L. Sharp, and R. J. Warmack. Detection of mercury-vapor using resonating microcantilevers. *Applied Physics Letters*, 66(13):1695–1697, 1995.

[68] Y. Toivola, J. Thurn, R. F. Cook, G. Cibuzar, and K. Roberts. Influence of deposition conditions on mechanical properties of low-pressure chemical vapor deposited low-stress silicon nitride films. *Journal of Applied Physics*, 94(10):6915–6922, 2003.

[69] A. H. M. van Roermund, C. J. M. Verhoeven, and J. R. Westra. *Oscillators and Oscillator Systems: Classification, Analysis and Synthesis*. Kluwer Academic Publishers, Dordrecht, The Netherlands, 1999.

[70] J. Voros. The density and refractive index of adsorbing protein layers. *Biophysical journal*, 87(1):553–561, 2004.

[71] J. Voros, J. J. Ramsden, G. Csucs, I. Szendro, S. M. De Paul, M. Textor, and N. D. Spencer. Optical grating coupler biosensors. *Biomaterials*, 23(17):3699–3710, 2002.

[72] A. W. Wang, R. Kiwan, R. M. White, and R. L. Ceriani. A silicon-based ultrasonic immunoassay for detection of breast cancer antigens. *Sensors and Actuators B-Chemical*, 49(1-2):13–21, 1998.

[73] M. S. Weinberg, C. E. Dube, A. Petrovich, and A. M. Zapata. Fluid damping in resonant flexural plate wave device. *Journal of Microelectromechanical Systems*, 12(5):567–576, 2003.

[74] D. Westberg, O. Paul, G. I. Andersson, and H. Baltes. CMOS-compatible device for fluid density measurements fabricated by sacrificial aluminum etching. *Sensors and Actuators, A: Physical*, 73(3):243–251, 1999.

[75] R. M. White and S. W. Wenzel. Fluid loading of a lamb-wave sensor. *Applied Physics Letters*, 52(20):1653–1655, 1988.

[76] S.-C. Wong, P. S. Liu, J.-W. Ru, and S.-T. Lin. Interconnection capacitance models for VLSI circuits. *Solid-State Electronics:An International Journal*, 42(6):969–977, 1998.

[77] G. H. Wu, R. H. Datar, K. M. Hansen, T. Thundat, R. J. Cote, and A. Majumdar. Bioassay of prostate-specific antigen (PSA) using microcantilevers. *Nature biotechnology*, 19(9):856–860, 2001.

[78] Y. N. Xia and G. M. Whitesides. Soft lithography. *Annual Review of Materials Science*, 28:153–184, 1998.

[79] K. Y. Yasumura, T. D. Stowe, E. M. Chow, T. Pfafman, T. W. Kenny, B. C. Stipe, and D. Rugar. Quality factors in micron- and submicron-thick cantilevers. *Journal of Microelectromechanical Systems*, 9(1):117–25, 2000.

[80] M. Zhang and M. Ferrari. Reduction of albumin adsorption onto silicon surfaces by Tween 20. *Biotechnology and bioengineering*, 56(6):618–625, 1997.

[81] C. Ziegler. Cantilever-based biosensors. *Analytical and Bioanalytical Chemistry*, 379(7-8):946–959, 2004.